SOLUTION OF INVERSE PROBLEM OF ELECTROCARDIOGRAPHY USING STATE SPACE MODELS

A THESIS SUBMITTED TO
THE GRADUATE SCHOOL OF NATURAL AND APPLIED SCIENCES
OF
MIDDLE EAST TECHNICAL UNIVERSITY

BY

ÜMİT AYDIN

IN PARTIAL FULFILLMENT OF THE REQUIREMENTS
FOR
THE DEGREE OF MASTER OF SCIENCE
IN
ELECTRICAL AND ELECTRONICS ENGINEERING

SEPTEMBER 2009

Approval of the thesis:

SOLUTION OF INVERSE PROBLEM OF ELECTROCARDIOGRAPHY USING STATE SPACE MODELS

submitted by **ÜMİT AYDIN** in partial fulfillment of the requirements for the degree of **Master of Science in Electrical and Electronics Engineering Department, Middle East Technical University** by,

Prof. Dr. Canan Özgen
Dean, Graduate School of **Natural and Applied Sciences**

Prof. Dr. İsmet Erkmen
Head of Department, **Electrical and Electronics Engineering**

Assist. Prof. Dr. Yeşim Serinağaoğlu Doğrusöz
Supervisor, **Electrical and Electronics Engineering Dept, METU**

Examining Committee Members:

Prof. Dr. Murat Eyüboğlu
Electrical and Electronics Engineering, METU

Assist. Prof. Dr. Yeşim Serinağaoğlu Doğrusöz
Electrical and Electronics Engineering, METU

Prof. Dr. Nevzat Güneri Gençer
Electrical and Electronics Engineering, METU

Prof. Dr. Kemal Leblebicioğlu
Electrical and Electronics Engineering, METU

Dr. Özlem Birgül
TUBITAK

Date:

I hereby declare that all information in this document has been obtained and presented in accordance with academic rules and ethical conduct. I also declare that, as required by these rules and conduct, I have fully cited and referenced all material and results that are not original to this work.

Name, Last Name: ÜMİT AYDIN

Signature :

ABSTRACT

SOLUTION OF INVERSE PROBLEM OF ELECTROCARDIOGRAPHY USING
STATE SPACE MODELS

Aydın, Ümit
M.S., Department of Electrical and Electronics Engineering
Supervisor : Assist. Prof. Dr. Yeşim Serinağaoğlu Doğrusöz

September 2009, 108 pages

Heart is a vital organ that pumps blood to whole body. Synchronous contraction of the heart muscles assures that the required blood flow is supplied to organs. But sometimes the synchrony between those muscles is distorted, which results in reduced cardiac output that might lead to severe diseases, and even death. The most common of heart diseases are myocardial infarction and arrhythmias. The contraction of heart muscles is controlled by the electrical activity of the heart, therefore determination of that electrical activity could give us the information regarding the severeness and type of the disease. In order to diagnose heart diseases, classical 12 lead electrocardiogram (ECG) is the standard clinical tool. Although many cardiac diseases could be diagnosed with the 12 lead ECG, measurements from sparse electrode locations limit the interpretations. The main objective of this thesis is to determine the cardiac electrical activity from dense body surface measurements. This problem is called the inverse problem of electrocardiography. The high resolution maps of epicardial potentials could supply the physician the information that could not be obtained with any other method. But the calculation of those epicardial potentials are not easy; the problem is severely ill-posed due to the discretization and attenuation within the thorax. To overcome this ill-posedness, the solution should be constrained using prior information on the epicardial potential distributions. In this thesis, spatial and spatio-temporal Bayesian maximum *a posteriori* estimation (MAP), Tikhonov regularization and Kalman filter and Kalman smoother approaches are used to overcome the ill-posedness that is associated with the inverse problem of ECG. As part of the Kalman filter approach, the state transition matrix (STM) that determines the evolution of epicardial potentials over time is also estimated, both from the true epicardial potentials and previous estimates of the epicardial potentials. An activation time based approach was developed to overcome the computational complexity of the STM estimation problem. Another objective of this thesis is to study the effects of geometric errors to the solutions, and modify the inverse solution algorithms to minimize these effects. Geometric errors are simulated by changing the size and the location of the heart in the mathematical torso model. These errors are modeled as additive Gaussian noise in the inverse problem formulation. Residual-based and expectation maximization methods are implemented to estimate the measurement and process noise variances, as well as the geometric noise.

Keywords: Inverse electrocardiography, Spatio-temporal methods, Kalman filter, Noise estimation, Geometric errors

ÖZ

ELEKTROKARDİYOGRAFİDE GERİ PROBLEMİN DURUM UZAYI MODELLERİ KULLANILARAK ÇÖZÜMÜ

Aydın, Ümit
Yüksek Lisans, Elektrik ve Elektronik Mühendisliği Bölümü
Tez Yöneticisi : Yrd. Doç. Dr. Yeşim Serinağaoğlu Doğrusöz

Eylül 2009, 108 sayfa

Kalp bütün vücuda kan pompalayan hayati bir organdır. Kalp kaslarındaki senkron kasılma ve gevşemeler organlara gerekli kan akışının gerçekleşmesini sağlamaktadır. Fakat bazen bu kaslar arasındaki senkronizasyon bozulmakta ve düşen kalp debisi ölüme kadar gidebilen hastalıklara sebep olabilmektedir. Bu hastalıklardan en çok karşılaşılanlar enfarktüs ve aritmidir. Kalp kaslarındaki kasılmalar elektrik sinyalleri ile kontrol edilmektedir, bu sebeple kalbin elektriksel aktivitesi hakkında bilgi edinmek bize hastalıkların cinsi ve ciddiyeti hakkında da çok önemli bilgiler vermektedir. Günümüzde kalp hastalıklarının teçhisinde kullanılan standart klinik yöntem klasik 12 kanallı elektrokardiyografidir (EKG). Bu yöntem birçok hastalığın teşhisinde kullanılsa da vücut yüzeyinden alınan ölçümlerin seyrekliği çıkarımları sınırlamaktadır. Bu tezde başlıca amaç kalpteki elektriksel aktiviteyi vücut yüzeyinden sık bir çekilde alınan ölçümlerden bulmaktır ve bu ters elektrokardiyografi problemi olarak tanımlanmaktadır. Elde edilen yüksek çözünürlüklü epikart potansiyel haritaları ise doktora baçka hiçbir girişimsiz yöntemle elde edilemeyecek bilgiler verir. Fakat epikart potansiyellerini hesaplamak kolay değildir çünkü, ters EKG problemi göğüs kafesinde sinyallerin uğradığı ayrıklaşma ve zayıflama sebebiyle kötü konumlanmıştır. Bu problemin üstesinden gelebilmek amacıyla, epikart potansiyel dağılımları ile ilgili önsel bilgiler kullanılarak çözüme bazı kısıtlamalar getirilir. Bu tezde uzamsal ve zaman-uzamsal Bayes en büyük sonsal kestrim (MAP), Tikhonov düzenlileştirmesi ile Kalman filtre ve yumuşatıcı bu kötü konumlandırılmış problemi çözme amaçlı kullanılmıştır. Kalman filtre yaklaşımının bir uzantısı olarak epikart potansiyellerinin zamana bağlı değişimini modelleyen durum geçiş matrisi (DGM) hem gerçek epikart potansiyellerinden hem de başka yöntemlerle kestirilen epikart potansiyellerinden elde edilmiştir. Bu tezin başka bir hedefi ise geometrik hataların çözümlere etkilerini incelemek ve ters çözüm algoritmalarını bu etkileri minimize edecek şekilde modifiye etmektir. Bu kapsamda geometrik hatalar kalbin boyut ve pozisyonunun matematiksel modelde değiştirilmesi ile elde edilmiştir. Bu hatalar ters problem formülasyonunda eklenir Gaussian gürültü olarak modellenmişlerdir. Daha sonra ise durum ve ölçüm gürültü varyansları ile geometrik hatadan kaynaklanan gürültü varyansı, artıklardan yararlanan algoritma ve beklenti ençoklaması kullanılarak kestirilmeye çalışılmıştır.

Anahtar Kelimeler: Geri elektrokardiyografi, Uzamsal-zamansal yöntemler, Kalman filtre, Gürültü kestirimi, Geometrik hata

ACKNOWLEDGMENTS

I would like to thank my thesis supervisor Assist. Prof. Dr. Yeşim Serinağaoğlu Doğrusöz for providing me this research opportunity and guiding me through the study.

This study is part of the project 105E070 that is supported by Turkish Scientific and Technological Research Council (TÜBİTAK). I thank to Dr. Robert S. MacLeod from University of Utah, Nora Eccles Harrison CVRTI and the SCI Institute for the epicardial measurements used in the study and the map3d software.

I would like to thank all my colleagues Dr. Özlem Birgül, Murat Önal, Uğur Cunedioğlu, Ceren Bora and Alireza Mazloumi at ECG laboratory for their comments and technical supports.

I also would like to thank Prof. Dr. Murat Eyüboğlu and all my colleagues at MRI research laboratory Volkan Emre Arpınar, Evren Değirmenci, Gökhan Eker, Rasim Boyacıoğlu, Tankut Topal and Ali Ersöz for their supports.

I also would like to express my appreciation to all my friends especially Sedat Doğru, Güven Çetinkaya, Kerim Kara, Ozan Özyurt, Masood Jabarnejad and Ersin Karcı for their enthusiastic support throughout the development of this thesis.

Finally, I like to express very special thanks to my dear family for their endless support and love throughout my education.

TABLE OF CONTENTS

CHAPTERS

LIST OF TABLES

TABLES

LIST OF FIGURES

FIGURES

CHAPTER 1

INTRODUCTION

1.1 Motivation of the Thesis

Heart failure affects approximately 15 million people worldwide and since 1968, the role of heart failure as the primary cause of death has increased fourfold [1]. Only in European Union over 1.9 million deaths annually are due to cardiac diseases. Arrhythmias are among the major causes of heart failure. In order to diagnose arrhythmias, knowledge about the electrical activity within the heart is vital. Classical 12-lead electrocardiogram (ECG) is the standard diagnostic tool to measure the electrical activity of the heart. However, although physicians could diagnose certain pathologies with the 12-lead ECG, this technique's low resolution limits its benefits significantly; for example, precise localization of pathologies like myocardial infarcts and arrhythmogenic foci is not possible with the 12-lead ECG [2]. Furthermore, the 12-lead ECG could only diagnose %60 of acute inferior myocardial infarctions [3]. The 12-lead ECG also suffers from the effects of inhomogeneity within the thorax, and Brody and respiration effects, which cause wrong interpretations [4]. For clinical purposes, catheters are used to obtain details about the heart's electrical activity [5]. High resolution images are obtained with these catheters; however, the invasive nature of this technique restricts its usage. There are also other non-invasive techniques to monitor cardiac behavior such as cardiac CT, nuclear imaging, stress electrocardiography and echocardiography. Inverse problem of ECG, which is a method to provide high resolution images of the heart's electrical activity, could support the diagnosis made based on the 12-lead ECG. In the inverse ECG problem high resolution cardiac electrical activity is estimated noninvasively from dense body surface potential measurements (usually minimum 64 electrodes). Some advantages of using this type of electrocardiographic imaging are [6]:

- To screen people that have higher risks for arrhythmias.
- To find the source of patient specific arrhythmia mechanism to determine the best cure.
- To determine the optimal location and size of the diseased tissue for ablation and targeted drug delivery.
- To assess the success of the therapy over time.
- To further study the mechanism and properties of arrhythmias.

Due to above cited reasons and benefits, the studies on electrocardiographic imaging continues faster than ever before. The main motivation of this thesis is to make a contribution to those efforts.

1.2 Contributions of the Thesis

- The performances of spatio-temporal methods for the solution of inverse problem of electrocardiography are compared.
- New techniques to determine the state transition matrix (STM), which temporally maps the epicardial potentials with each other, are employed to solve the inverse problem of ECG using the Kalman filter and smoother. Those techniques include reduction of the problem size for faster computation using an activation time based approach and the calculation of the STM from previous estimates such as Bayesian maximum *a posteriori* estimation (MAP) and Tikhonov regularization instead of from real epicardial potentials.
- The effects of geometric errors to Bayesian MAP and Kalman filter solutions are studied.
- A statistical noise model that also includes the effects of geometric errors is modified to be used in the inverse problem of ECG.

- A residual based method and a method based on expectation- maximization (EM) algorithm are used to estimate the noise covariances needed in the Bayesian MAP estimation and the Kalman filter algorithms. The two proposed noise estimation methods are used to estimate the measurement and process noise covariances in the Kalman filter approach, with or without additional geometric noise.

1.3 Scope of the Thesis

In this thesis the second chapter is devoted to the background information. In this chapter, first anatomy and physiology of the heart is given. Then most common cardiac diseases are explained with a stress on arrhythmias. Next, the forward and inverse problems of ECG are defined along with a literature survey on these topics. Finally, the chapter is concluded with a short section on validation of the inverse ECG problem solutions and studies on human subjects.

The third chapter contains problem definition, theory and methods of the inverse problem of ECG in terms of epicardial potentials. In this chapter after the problem definition is given, the second part includes a detailed explanation of Tikhonov regularization, spatial and spatio-temporal Bayesian MAP estimation, Kalman filter and smoother and the estimation of STM. Then a statistical model used to overcome the effects of the geometric errors is explained. The final part of this chapter is devoted to the noise estimation algorithms.

In the fourth chapter, the application details of the algorithms given in theory section are provided, along with the results and the discussions of those results.

At the last chapter, conclusions of this study are given.

CHAPTER 2

BACKGROUND INFORMATION

2.1 Introduction

In this chapter first anatomy and physiology of the heart is explained shortly. Then a brief information is given about main cardiac diseases with the focus on arrhythmias. Then recent progresses on the forward and inverse problem of electrocardiography is given. The forward problem of ECG targets the determination of body surface potentials from cardiac electrical activity, and the inverse problem of electrocardiography, which is the main topic of this thesis, is defined as the determination of cardiac electrical activity from body surface potentials.

2.2 Anatomy of the Heart

The human heart is located in the middle mediastinum of the thorax and weights around 250-300 g. It is a muscular organ that is enclosed with the pericardium. There is a small region between the fibrous sac pericardium and the heart which is filled with a fluid and this fluid serves as a lubricant agent for heart that helps avoiding problems that could occur during movement due to contractions [7]. If we omit pericardium, heart is composed of three layers as seen in Figure 2.1. Those layers are:

- **Epicardium:** This is the outer layer of the heart and surrounded by pericardium. The potentials on epicardium (epicardial potentials) are widely used as cardiac sources in inverse and forward problems of electrocardiography.

- **Myocardium:** This layer is in between epicardium and endocardium. This is the thickest layer and it contains the myocytes (striated muscle cells) whose synchronous contraction and relaxation results in pumping of the blood. The main objective in electrocardiographic imaging is the determination of the activity within this region. The solutions in terms of epicardial or endocardial potentials are obtained due to their close location to myocardium.

- **Endocardium:** This is the inner layer of the heart and it has a smooth surface to allow blood flow with minimum resistance. The endocardial potentials which can be recorded with catheters are also used as cardiac sources for electrocardiographic imaging.

The heart has four chambers as seen in Figure 2.2. The upper ones are the right and left atrium which are responsible for collecting blood from vessels. The lower ones are called right and left ventricle. The right ventricle pumps the blood to lungs and the left ventricle pumps the blood to body. Because pumping the blood to body requires more pressure than pumping it to lungs the left ventricle has a thicker myocardial layer.

2.3 Physiology of the Heart

Heart is an organ that receives the low pressure blood from venous blood vessels and then ejects it to arterial blood vessels after increasing its pressure. By this way the nutrients and oxygen needed is supplied to every living cell in human body via blood.

2.3.1 Cardiac Conduction System

For a normal heart, the excitation starts at the sinoatrial (SA) node then spreads to the atrioventricular (AV) node thorough myocytes at atrium. The only conductive region between atria and ventricles is the AV node so the depolarization wavefront spreads through AV node to ventricles. AV node decreases the conduction velocity and the wavefront spreads through bundle of His to right and left bundle branches

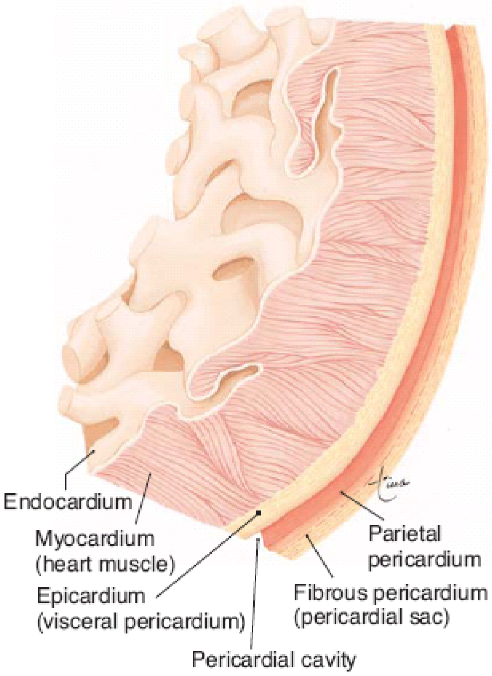

Figure 2.1: Layers of the heart [8]

where the velocity of conduction is increased again. Then the conduction velocity becomes even higher from the bundle branches, at purkinje fibers and the wavefront is transmitted to the ventricular myocytes to complete conduction path [9]. The conduction velocities of those regions are shown in Figure 2.5. The delay at AV node has two main advantages. Firstly, it provides sufficient time for atrial contraction and depolarization before ventricular contraction and depolarization occur. Secondly, it limits the frequency and prevent the ventricles from the affects of the atrial flutter and fibrillation [9]. This is very important because although atrial flutter and fibrillation are not very fatal, ventricular fibrillation cause death in just a few minutes [10].

Although cardiac excitation starts from the SA node for a normal heart AV node, bundle of His, bundle branches and purkinje fibers also have the self-excitation ability. This property of cardiac tissues prevent fatal consequences that might occur when a problem occur at the SA node. The self-excitation frequencies of those tissues are smaller than the SA node and when an excitation with a higher frequency received they follow it. The self-excitation frequencies for cardiac tissues are also shown at Figure 2.5.

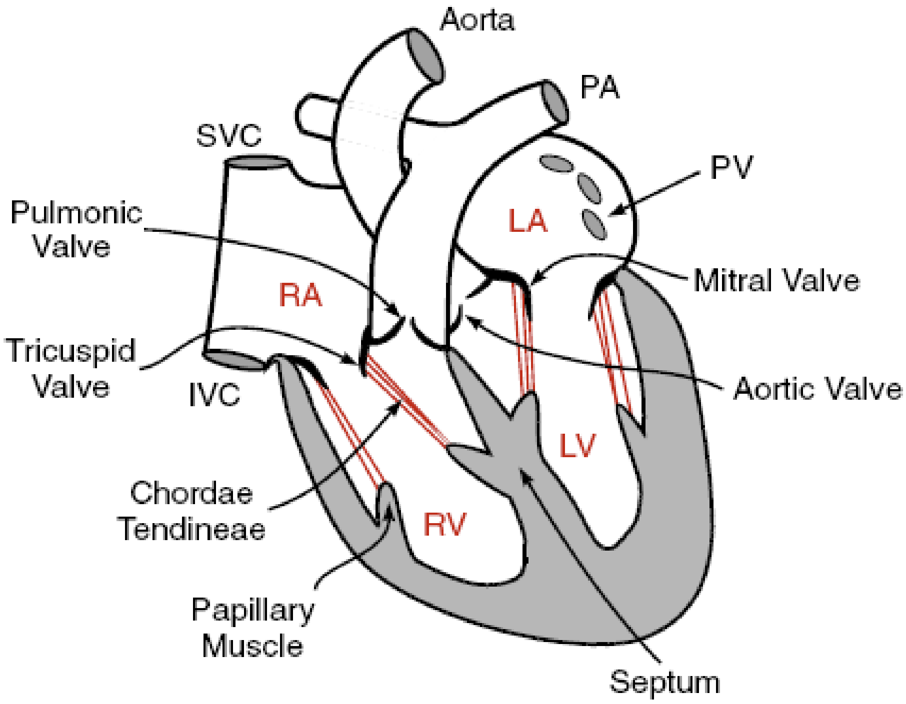

Figure 2.2: Anatomy of the heart. RA, right atrium; LA, left atrium; RV, right ventricle; LV, left ventricle; SVC, superior vena cava; IVC, inferior vena cava; PA, pulmonary artery; PV, pulmonary veins [9].

2.3.2 Cardiac Action Potential

Although the action potential wavefront changes for different tissues as seen in Figure 2.3, the generation of the typical cardiac action potential after the stimulus can be explained with steps below:

1. The quick Na^{+} channels are opened which causes sodium to flow inward thus increasing the membrane potential through positive. Then depolarization occur around +20 mV.
2. Slower K^{+} channels are opened and the outward flow of K^{+} stops the rising potential due to Na^{+}.
3. Na^{+} channels start closing while K^{+} channels are still open.
4. Slow Ca^{++} channels are opened and stay opened for approximately 20 millisecond which causes the plateau in membrane potential potential due to the inward Ca^{++} flow.
5. Ca^{++} channels are closed and repolarization occur with membrane voltage around -90 mV.

The shape of cardiac action potential differs from the action potential of other excitable tissues in the body. The difference is the plateau present after depolarization in cardiac action potential. The main reason for this plateau is the 4'th step explained above so Ca^{++} channels. This plateau does not occur in other excitable cells because they do not have Ca^{++} channels [7]. A typical action potential for a ventricular muscle cell and the ion permeabilities are shown in Figure 2.4.

2.3.3 Electrocardiography

In electrocardiography (ECG) the summation of cardiac action potentials are measured. In Figure 2.6 a classical ECG measurement is shown. In this figure [4];

- P represents the atrial depolarization

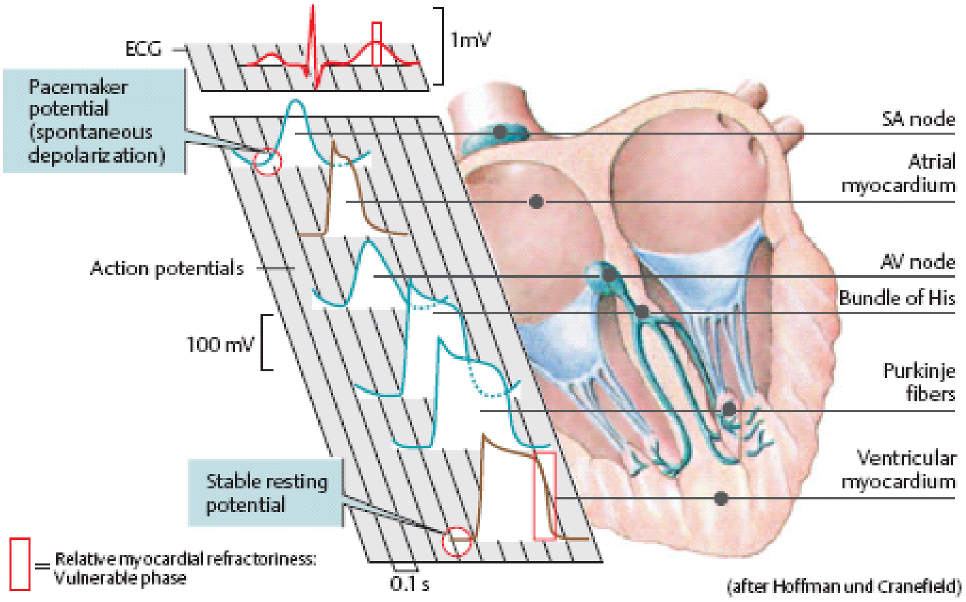

Figure 2.3: The action potential waveforms for different cardiac tissues [11].

- QRS interval represents the ventricular depolarization (also atrial repolarization occur at this interval but it is surpassed by ventricular depolarization)
- T represents the ventricular repolarization

2.4 Cardiac Diseases

At this section only some of the cardiac diseases will be explained. The focus will be on diseases that can be diagnosed with inverse electrocardiography.

2.4.1 Myocardial Infarction

Myocardial infarction is one of the major health problems and each year more than 1.5 million people suffer from it only in United States [7]. Heart muscles are in a continuous cycle and this process requires energy. The oxygen and nutrients required for energy production are supplied by coronary arteries. Those arteries might suffer from occlusions which results in reduced blood flow. This phenomenon is called ischemia.

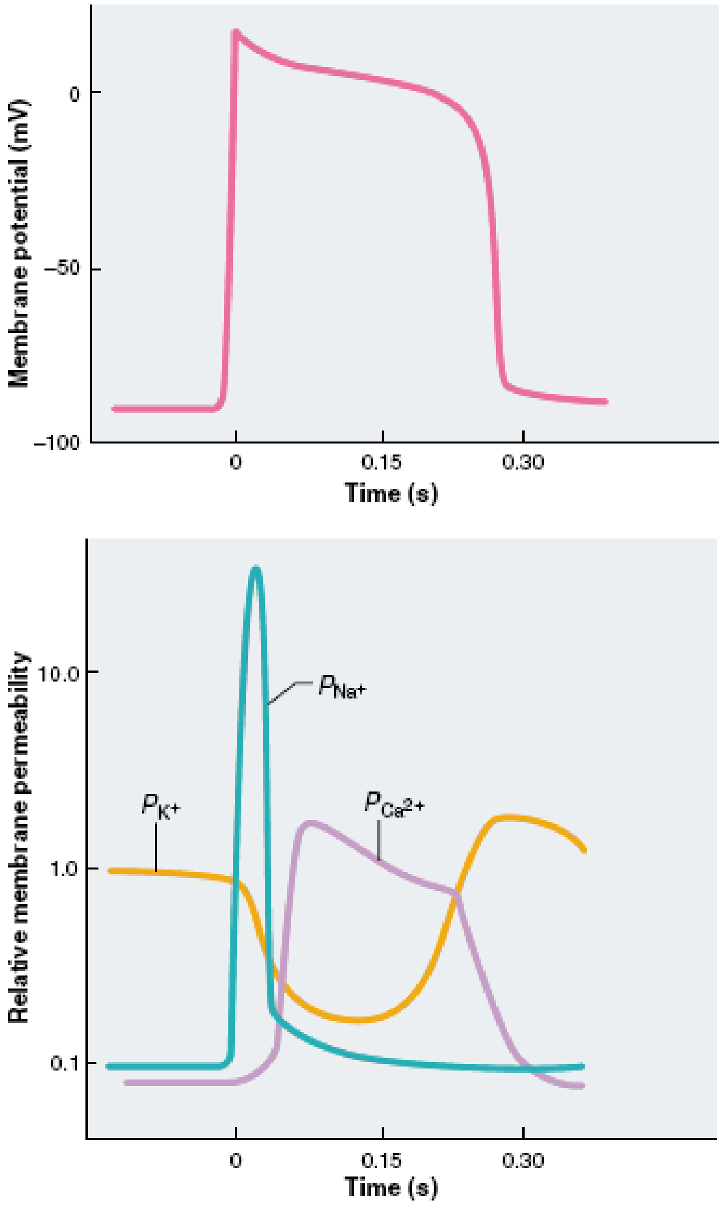

Figure 2.4: Action potential wavefront and ion permeabilities for a ventricular muscle cell. The upper figure shows the membrane potential and the lower figure shows the simultaneous ion permeabilities [7]

.

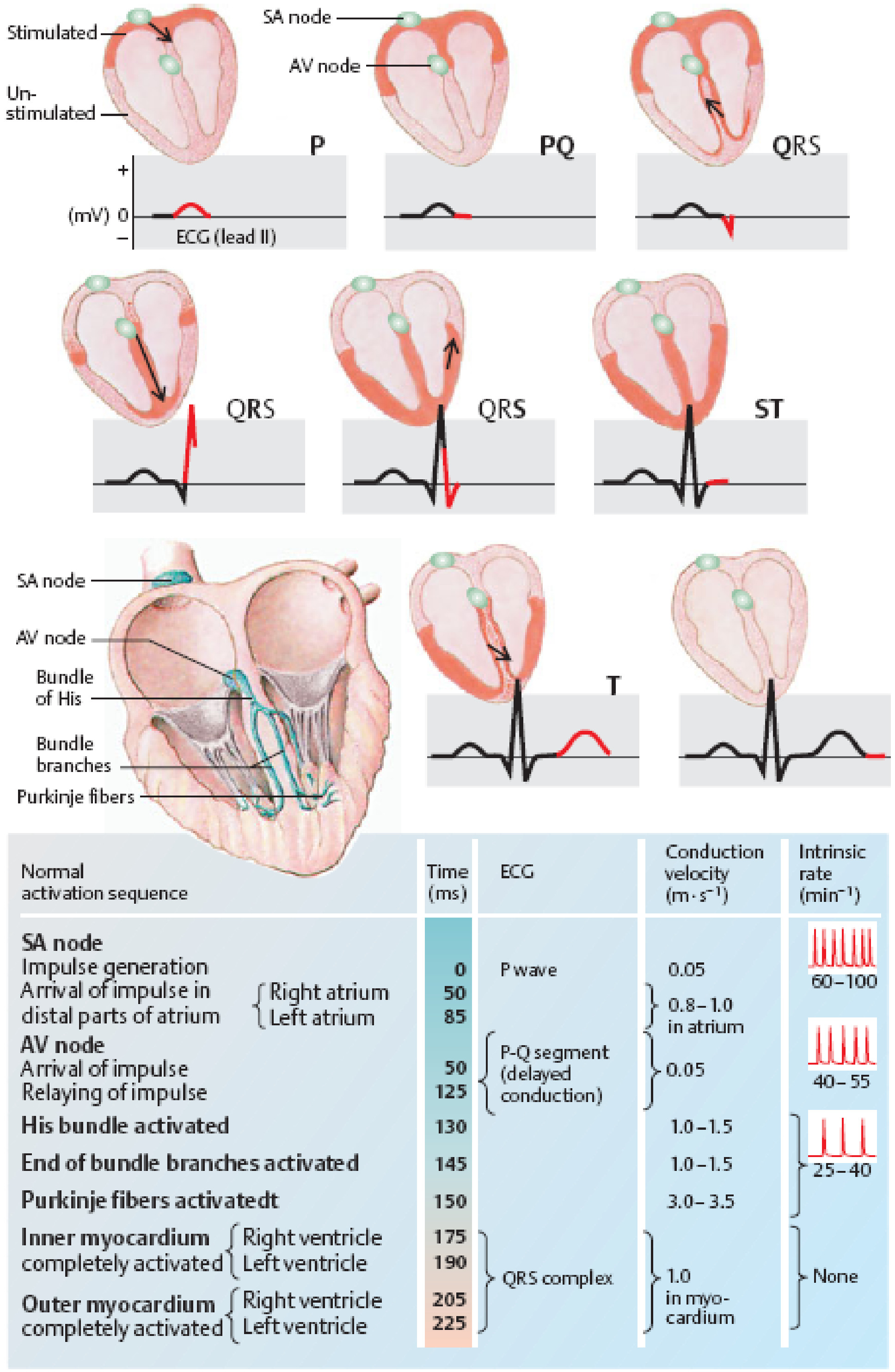

Normal activation sequence		Time (ms)	ECG	Conduction velocity $(m \cdot s^{-1})$	Intrinsic rate (min^{-1})
SA node					
Impulse generation		0	P wave	0.05	60–100
Arrival of impulse in distal parts of atrium	Right atrium	50		0.8–1.0 in atrium	
	Left atrium	85			
AV node					
Arrival of impulse		50	P-Q segment (delayed conduction)	0.05	40–55
Relaying of impulse		125			
His bundle activated		130		1.0–1.5	25–40
End of bundle branches activated		145		1.0–1.5	
Purkinje fibers activatedt		150		3.0–3.5	
Inner myocardium completely activated	Right ventricle	175	QRS complex	1.0 in myocardium	None
	Left ventricle	190			
Outer myocardium completely activated	Right ventricle	205			
	Left ventricle	225			

Figure 2.5: The path of cardiac impulse conduction and the corresponding regions at the electrocardiogram with the conduction velocities, conduction times and self-excitatory (intrinsic) frequencies [11].

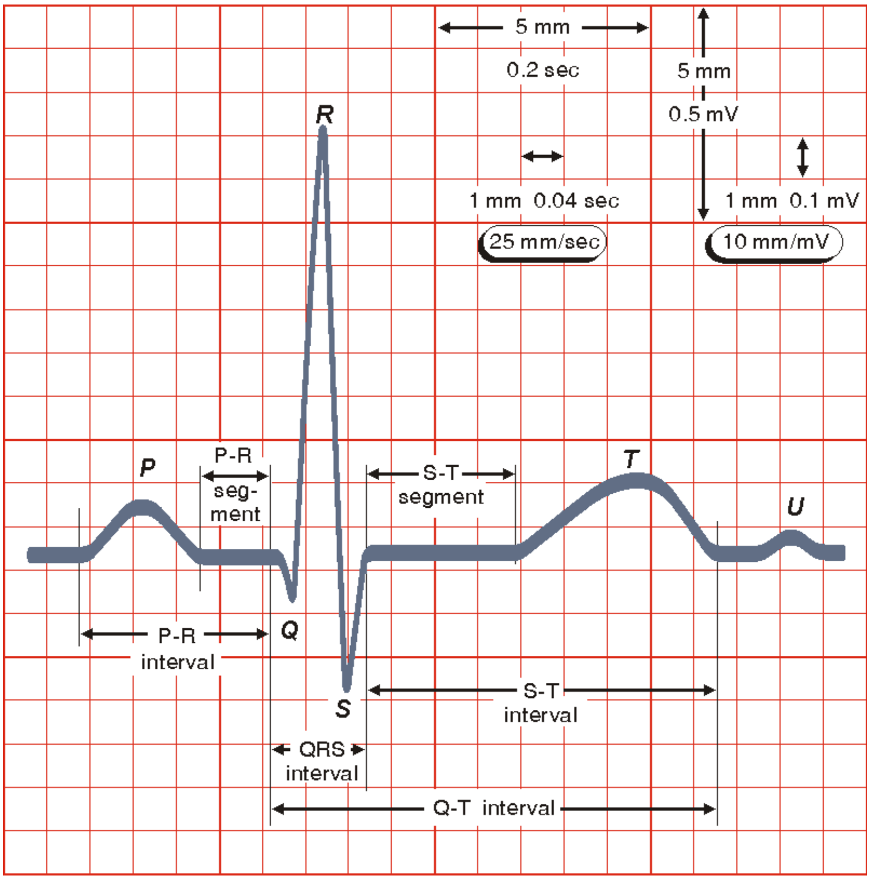

Figure 2.6: A typical ECG measurement [4].

If the damage due to ischemia is severe the tissues at that part of the heart might die and this is called myocardial infarction. Those ischemic regions or infarctions cause the extracellular conductivity changes which could be detected with investigation of epicardial potentials [12].

2.4.2 Cardiac Re-entry Phenomenon

In normal circumstances the excitation wavefront follows a predetermined path because all other paths are obstructed with tissues in refractory period. But sometimes due to certain problems the wavefront can find other ways to spread and after a period it comes back and simulates the same tissues again and again unless the conduction is resynchronized with electroshock.

The causes and mechanism of cardiac re-entry are usually described with cardiac muscle strips that are cut in a circular shape. Here this convention will be followed too [10].

In Figure 2.7 upper part shows the conduction for a normal tissue. Here the first stimuli is given from the 12 o'clock position and it spreads through the circle. The purple regions show the cells that are in refractory period. As can be seen from the lower part of Figure 2.7 when the excitation arrives at the initiation point again, it vanishes because neighboring cells are still in refractory period. However, sometimes when the excitation wavefront reaches the initiation point those points have been already out of the refractory period and the wavefront continues to travel forever in that loop. The reasons for this phenomenon and some typical pathologies lies under this conditions are summarized at Table 2.1.

Also this mechanism can be observed on whole heart instead of only circular muscle strips. Figure 2.8 is for a heart stimulated with a 60 hertz alternative current and very educational to show different waveforms caused by cardiac re-entry [10].

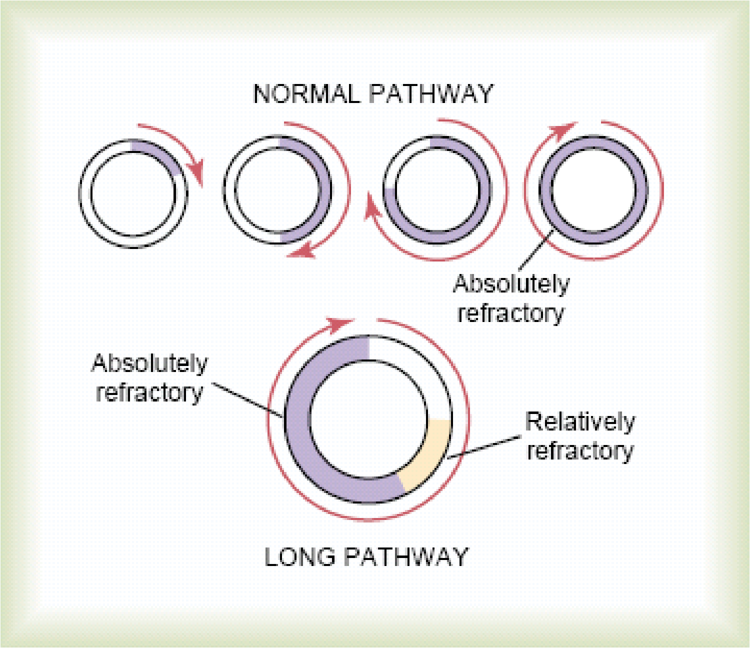

Figure 2.7: The mechanism of cardiac re-entry: At the upper part of the figure conduction in normal tissue is shown and at at the lower part the re-entry mechanism is shown. [10]

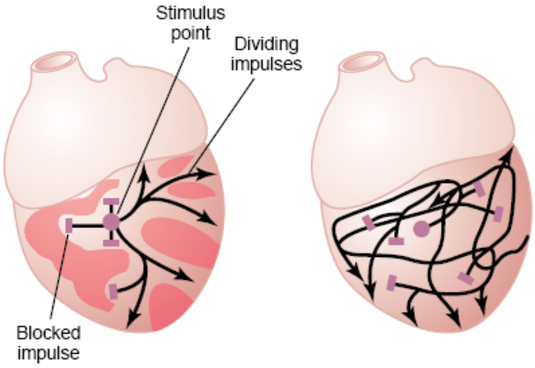

Figure 2.8: The cardiac re-entry model: At the left the initiation of the fibrillation can be seen with darker pink regions shows the regions in refractory period. The figure on the right hand side shows the propagation paths of those impulses. [10]

Table 2.1: The reasons for cardiac re-entry mechanism and possible diseases causing those.

Cause	Possible underlying diseases
The pathway around the circle is too long	Dilated Heart
The velocity of the conduction is too low	Blockage of the Purkinje Fibers Ischemia of the muscle High blood potassium
The refractory period of the muscle decreased significantly	Due to some drugs (epinephrine etc.) Repetitive electrical stimulation

2.4.3 Ventricular Fibrillation

Ventricular fibrillation is the most serious cardiac arrythmia and it can cause death if not treated within 1 to 3 minutes. As explained previously normally the excitation wavefront follows the same path in every cardiac cycle. But sometimes this path is distorted and the excitation wavefront follows other paths and returns to itself again which distorts the synchrony of the heart muscles. Due to this asynchrony sufficient blood can not be pumped to body which results in unconsciousness in a few seconds and death in a few minutes [10]. The main reason for ventricular fibrillation is known as re-entry phenomenon.

2.4.4 Atrial Fibrillation and Flutter

Atrial fibrillation and flutter are problems due to cardiac arrhythmias. The main cause of those problems is re-entry mechanism. In atrial flutter the depolarization wavefront spreads in one direction along atria with a much higher frequency than normal (200 to 350 beats per minute). On the other hand in atrial fibrillation there is not a single depolarization wavefront instead many different wavefronts spread through atria. The wavefront propagations for those two diseases can be seen at Figure 2.9. Both atrial flutter and fibrillation cause serious reduction in pumping mechanism of the atria but those diseases are not as serious as ventricular fibrillation [10].

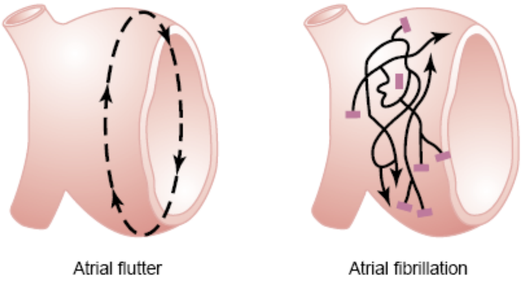

Figure 2.9: The movement of depolarization wavefront for atrial flutter and fibrillation [10].

2.5 Forward Problem of Electrocardiography

The goal in forward problem of ECG is to calculate the body surface potentials from the cardiac electrical activity. Although it may not seem so meaningful in clinical sense it has several implementations like [13]:

- Simulation of ECG with computer heart models
- Solution of reciprocal problem of determining currents on heart due to the current sources on body surface.

To solve the forward problem of ECG along with the anatomical information also a numerical solver is required.

2.5.1 Obtaining the Anatomical Information

In order to solve forward or inverse problem of electrocardiography, information about the geometries (or anatomies) of the organs is a crucial requirement. In the literature the geometry information is usually obtained by Magnetic Resonance Imaging (MRI) or Computed Tomography (CT) [2]. The most important criticization about using those imaging modalities for electrocardiographic imaging is that they are expensive. Another drawback about those are that they are too heavy and not mobilized so they can not be used for a system that could overcome the classical 12 lead ECG. In order to address these problems studies on obtaining necessary geometrical information for electrocardiographic imaging using other imaging techniques emerge. One group studies on using electrical impedance tomography (EIT) for this purpose and try to benefit from its relative cheap price and high mobility [14, 15, 16]. Another advantage of using EIT is its ability to measure conductivity values of the tissues. By using these data instead of using predetermined values for each tissue, conductivities that are specific for each patient could be used to obtain better results. There are also studies that use three dimensional ultrasound for this purpose [17, 18].

2.5.2 Numerical Solution Techniques

After the geometry information is obtained using imaging modalities described section 2.5.1, a numerical approach is needed to calculate the transfer matrix that maps the parameters of the cardiac sources to body surface potentials. Those numerical solvers can be categorized as [13]:

- Volume Element Methods:
    - Finite Element Method (FEM)
    - Finite Difference Method
    - Finite Volume Method
- Surface Element Methods:
    - Boundary Element Method (BEM)

Here FEM and BEM are compared because the most widely used methods in electrocardiographic imaging are those two. The main advantages and disadvantages of these methods compared to each other are [13, 19]:

- For FEM solution, whole tissue volume should be discretized, on the other hand for BEM, only the boundaries of the tissues with different conductivities should be discretized which reduces the complexity by a great amount.
- FEM could model tissues with anisotropic conductivities such as the the fiber orientation of the heart. BEM could model only isotropic tissues because only

the boundaries of those tissues are discretized. The anisotropies are included to the BEM model by determining an average of the conductivities that are longitudinal and transversal to the fiber direction.

- The matrices in FEM method are symmetric, positive definite and sparse but for BEM those matrices are dense which results in higher memory requirement.

The adaptive methods can be used to refine FEM in order to obtain finer solutions on the regions where fine solution is needed and coarse solution in regions where the solutions resolution is not that significant. By this way the extra work to construct fine meshes everywhere is avoided and this reduces the computation costs [20].

The accuracy of the BEM method is shown to be increased without upsurges in computational complexity using adaptive BEM [21]. For that purpose a coarse initial mesh is chosen and finer meshes are build using h-adaptive BEM in the literature [21]. The size of the meshes differ for different locations of the torso model based on the residual error. This means finer meshes are built for the parts of the torso where body surface potentials changes more. In that study it is shown that the accuracy can be increased as much as 10 percent with h-adaptive BEM.

Also there is a study to obtain numerical solution using method of fundamental solutions which eliminates the need to construct meshes [22]. At this technique first an auxiliary domain which encloses the real domain is constructed with auxiliary boundaries. The virtual source points (fundamental solutions) on those auxiliary boundaries achieves an approximate solution with linear superposition. Then the required epicardial surface potentials are calculated easily because the epicardial boundary is also in that auxiliary domain. Another advantage of the method of fundamental solutions over BEM is that the complex singular integrals are avoided [22].

2.6 Inverse Problem of Electrocardiography

The inverse problem of ECG is more meaningful in the clinical sense because from the measured body surface potentials the unknown cardiac electrical activity is tried to be calculated. In this section first different types of cardiac sources used to represent the electrical activity are explained. Then a literature survey on the inverse solution algorithms is given. In the next subsection validation studies and human experiments are explained. Finally the section is ended with a subsection on geometric errors.

2.6.1 Cardiac Source Models

There are many different cardiac source models that are used in inverse problem of electrocardiography. The first attempts focus on representing the electrical activity by one dipole [23]. Then more than one dipole and multipoles are used [24, 13]. The most frequently used source models today are epicardial or endocardial potential, transmembrame potential and activation time based models. Thus those techniques will be explained at this section. All of those techniques have advantages over others in terms of uniqueness, linearity and the severity of ill-posedness.

- **Uniqueness** One of the main difficulties about inverse electrocardiography problem is the non-uniqueness of the problem. Different cardiac source distributions may result in same body surface potentials which results in physologically meaningless solutions. In order to overcome this problem physiological constraints can be used.
- **Ill-Posedness** Ill-posedness is defined as the phenomenon that even small perturbations results in very severe errors in solutions. To overcome this problem regularization or statistical methods are widely used.

We have used the epicardial based method in our studies due to its advantages that will be explained shortly.

2.6.1.1 Epicardial and Endocardial Potential Distributions

One widely used model for cardiac sources is in terms of epicardial or endocardial potentials. Those solutions can be also called as surface potential based models. Although the cardiac sources are located at myocardium they could also be interpreted when potential distribution on surface is obtained. The detailed formulation and information regarding the epicardial potential based model is given at section 3.1. The advantages of formulating the problem in terms of surface potentials are: [2, 25, 13, 26]:

- In theory because the location of cardiac sources are restricted to the epicardial or endocardial surface the problem becomes unique.
- The solutions can be verified with either catheter measurements (for endocardial potential map) or sock electrodes (for epicardial potential map). Here we neglect the effects of surrounding impedances to those potentials which could change the measurements for example in open heart surgery.
- Another advantage of using epicardial potential based methods is that errors due to blood masses within the heart are avoided. Those blood masses cause significant errors due to the changes in flow and amount. The epicardial potentials are outside those masses. Thus while the epicardial potentials are calculated from body surface potentials those blood masses has no effects on solutions.
- The problem can be formulated linearly.

Some groups prefer studying on other formulations due to the disadvantages of surface potential based models such as:

- The problem is highly ill-posed due to the discretization and smoothing effects on potential signals passing through thorax. To overcome this problem regularization, statistical methods or filters are used which are explained in the subsection 2.6.2.1.
- Some studies show that it is affected more from geometric errors compared to activation time models [27, 28].

2.6.1.2 Transmembrane Potentials

The transmembrane potential (TMP) is the potential difference between inside and outside of the cell membrane. The calculation of transmembrane potentials at the myocardium becomes a widely studied model due to advantages such as [29, 30]:

- The problem can be formulated as a linear problem.
- Most of the diseases can be diagnosed with studying TMP's shape and distribution. Epicardial potentials and activation times could easily be obtained from the TMP distributions.

But it has a very serious limitation, the solution is non-unique so the obtained solution may not be physiologically meaningful unless additional constraints are used [29]. Also the increase in problem size a major disadvantage.

2.6.1.3 Activation Time Imaging

Although epicardial or endocardial potentials could give significant information regarding the myocardium, some groups prefer calculating the myocardial activation directly from BSP's. When uniform and isotropic conductivities are assumed along with zero phase amplitude, the formulation for activation time based model is:

$$\Phi(y,t) = \int_S \mathbf{A}(x,y)\mathbf{H}(t-\tau(x))dS_x \tag{2.1}$$

where **H** is the Heaviside step function, $\tau(x)$ is the activation time of myocardium at position x, $\mathbf{A}(x,y)$ is the uniform double layer transfer function and $\Phi(y,t)$ is the body surface potential at position y. The advantages of this formulation are [2, 25, 13, 26]:

- It deals directly with the phenomenon sought which is the activation times at myocardium.
- It is better-posed then surface potential methods.
- It deals with only a few parameters eg. the activation time of the tissue at a certain location whereas the surface potential methods tries to find the potentials for each time instant which requires a lot more parameters.
- Some studies show that it is affected less from geometric errors comparison with surface potential based methods [27, 28].

There are also disadvantages of this model:

- The solutions cannot be verified directly with measurements as in the case of surface potential methods.
- The problem is non-linear which results in more complex calculations.
- The model forces the solution of activation times for all tissues based on a template function that mimics the transmembrane potentials and because this template function is not valid at ischemic or infarcted regions, the solution fails [29].
- The isotropy assumption for myocardium limits its results (There are some recent studies that does not require isotropy assumption to overcome this limitation [31]).

2.6.2 Literature Survey on Inverse Solution Approaches

At this subsection first, a literature survey on the solution of inverse problem of ECG in terms of epicardial potentials and other source models is given then the literature survey is concluded with some recent works on human studies and validation methods.

2.6.2.1 Methods in Literature to Deal with Ill-posedness for Epicardial Potential Based Model

In inverse electrocardiography literature many different techniques were used to solve inverse problem of electrocardiography. Some of those are:

- **Tikhonov Regularization:** It is the most widely used method in the literature and it is explained in detail in section 3.2.1 [32, 33]. Shortly its solution is the minimization of the sum of the data misfit and a constraint to regularize the solution.
- **Twomey Regularization:** It is very similar to Tikhonov regularization but the constraint is the two-norm of the difference between the *a priori* and *a posteriori* estimate instead of the energy of the estimate [34].

- **Truncated Singular Value Decomposition (TSVD) :** The main motivation in TSVD is the elimination of the small singular values of the transfer matrix to overcome the ill-posedness [35]. This elimination regularize the solution but due to the elimination of the high frequency components associated with the small singular values the solution suffers from serious smoothing.

- **Bayes Maximum A Posteriori Estimation (Bayes-MAP):** The conditional *a posteriori* probability density function (pdf) for epicardial potentials given the BSP's is maximized with conditional *a priori* pdf of epicardial potentials given. Usually the solution is solved separately for each time instant which makes it a spatial algorithm [36]. The algorithm could also be modified as a spatio-temporal approach [37]. The detailed information about both spatial and spatio-temporal Bayes-MAP is given in chapter 3.

- **State-Space Models:** Kalman filter (or state space model) is also used to benefit from the spatio-temporal behavior of electrocardiographic imaging problem [38, 39, 40, 41, 42, 43]. Its optimality in the sense of mean square error with given *a priori* information is a major advantage of Kalman filter. The main difficulty about the usage of Kalman filter for electrocardiographic imaging is the determination of the state transition matrix (STM). This matrix is critical because it determines the spatio-temporal relationship of epicardial potentials for two consecutive time instants. Berrier *et al.* uses an identity matrix multiplied by a scalar as STM which means that the epicardial potential at the next time instant only depends on its present value [38]. Other studies calculate the STM from epicardial potentials [39, 40, 41].

- **Other Approaches:** There are a number of other studies that use different algorithms to solve inverse ECG problem like hybrid methods such that the one combines the least squares QR with truncated singular value decomposition, genetic algorithms and Laplacian weighted minimum norm [44, 45, 46].

At this point extra emphasis should be given to spatio-temporal methods. The reason for this is, they better represent the cardiac electrical activity comparison to spatial methods due to spatio-temporal nature of the phenomenon itself. Most widely used spatio-temporal approaches for electrocardiographic imaging are explained shortly below: Although most of the explained studies are for epicardial potentials also a study for trans-membrane potentials (TMP) is explained because of the close relationship between TMP and epicardial potentials.

Brooks *et al.*'s study is important in the sense that they employed a multiple constraint approach [32]. In classical Tikhonov regularization as previously described, the solution is found with the minimization of the data fit error and the constraint. In their study they added an extra constraint to the optimization problem of Tikhonov regularization. The regularization parameters are determined by plotting the residual norm against the norms of the constraints and using the corner of that surface. They call this method L-surface because it is a method based on L-curve. They have used two different approaches: 1) They used two spatial constraint. 2) They used one spatial and one temporal constraint which they call joint time/space (JTS) regularization. Their results show that using two spatial constraint instead of one supply the solution the robustness to the exact choice of regularization parameter and smaller regularization parameter values were enough to obtain satisfactory solutions. In the JTS case they stated that they obtained more realistic results in temporal sense in comparison to only spatial constraint. This study is very important in the sense of benefiting from spatio-temporal information to obtain more accurate solutions to inverse electrocardiography problem.

Greensite *et al.*'s study is very important in the sense that using spatio-temporal information for inverse problem of electrocardiography [47]. The isotropy assumption described in this work allow the problem's spatial and temporal covariance matrices written separately with a Kronecker product. This property has been used to include temporal information to Tikhonov regularization and Bayes-MAP approach [37, 43].

The unknown state at Kalman filter algorithm is the surface potentials in most of the studies for inverse ECG problem [38, 39, 40, 41, 42, 43]. As previously stated the major problem for Kalman filter based inverse ECG methods, is the determination of state transition matrix which determines the time evolution of the states. In their study Joly *et al.* use two different models as STM [41]. The first STM is identity matrix multiplied with a scalar ($\mathbf{F} = \alpha\mathbf{I}$) and the second one is calculated with a regularized least squares approach from measured epicardial potentials. El-Jakl *et al.* calculates the STM and noise covariances with expectation maximization algorithm from body surface potentials but they define only two parameters for STM such as $\mathbf{F} = \alpha\mathbf{I} + \beta\mathbf{S}$ where **I** is the identity matrix and **S** represents the spatio-temporal correlation of one node and its four closest neighbors at the previous time instant [40]. In that study El-Jakl *et al.* also calculates the STM from epicardial potentials too. Berrier *et al.*'s study also uses an identity matrix multiplied by a scalar as STM. The difference of their study from others is that instead of epicardial potentials they assume endocardial potentials as unknown state. Goussard *et al.* again use the epicardial potentials as the unknown state and calculates the STM with a linear prediction model from epicardial potentials [39]. Their model benefits from the locality character of the depolarization wavefront to reduce the problem dimension. They also used a training set to calculate STM. More information about the work of Goussard *et al.* is given in the section 3.2.5.

Ghodrati *et al.*'s study differs from other Kalman filter approaches because they use the activation wavefront as the unknown state [48]. In their study Ghodrati *et al.* use two approaches which they called wavefront-based curve reconstruction (WBCR) and wavefront-based potential reconstruction (WBPR). In WBCR the epicardial potentials are found from the activation curve with a basic assumption where the potentials are modeled as either active, inactive or transition. The wavefront curve is modeled as changing according to a curve evolution function whose shape and speed is determined by the parameters like angle between curve normal and fiber direction, fiber effect coefficients and spatial factor. Because this model is non-linear, Extended Kalman filter is used with wavefront curve as unknown state. The WBPR benefit from the relationship between wavefront curve and epicardial potentials. But the potential model is much simpler where the most important parameters are the distance of the node from the wavefront and whether the node is inside or outside of the curve. The results show that both WBCR and WBPR produce better results compared to zero'th order Tikhonov regularization.

Mesnarz *et al.* consider both spatial and temporal constraints and use these constraints to solve the problem [29]. They used TMP's as the cardiac source. They add temporal constraint as a side constraint with two assumptions. The first one is assuming TMP as monotonically nondecreasing function during depolarization and monotonically nonincreasing function during repolarization. The second temporal constraint is the determination of upper and lower bounds for the TMP value to restrict amplitude. They used the amplitude and Laplacian with usage of 0'th and 2'nd order Tikhonov regularization to benefit from spatial constraint. Then they changed the Tikhonov regularization scheme to a large-scale convex quadratic optimization problem with respect to the linear temporal constraint. The main advantages of their method is the avoidance of temporal regularization parameter (because a side temporal constraint is used) and the imposition of weak temporal constraints which allow acceptable solutions not only for healthy tissues but also for ischemic and infarcted regions.

The interested reader about spatio-temporal approaches should refer to the study of Zhang *et al.* which is important in the sense that they compared the three most widely used spatio-temporal inverse solution approaches for dynamic inverse problems [49]. Those methods are multiple constraints method [32], state-space models (Kalman filter) [40, 41] and Greensite's isotropy assumption [50, 47]. More information about Greensite's approach and Kalman filter solutions will be given in chapter 3 and multiple constraint approach is explained above in the work of Brooks *et al.* [32].

2.6.2.2 Other Approaches to Obtain Cardiac Electrical Activity

He *et al.* uses Laplacian weighted minimum norm (LWMN) algorithm to determine the current dipoles at myocardium [46]. They found the location of the arrhythmias in three dimensional myocardium which distinguishes this study from others which tries to find the location of arrhythmia with solutions of epicardial or endocardial potentials. Due to spatial smoothing effects of Laplacian operator they also applied a recursive weighting algorithm to detect even small arrhythmia sites.

Farina *et al.* suggested to use the information obtained from the simulations as a priori information for inverse ECG solution [30]. For that purpose they used cellular automaton to calculate transmembrane potentials for the patients anatomical data obtained by MRI. Then using FEM the epicardial potentials are calculated from those transmembrane potentials. They compared three regularization methods which are 0'th order Tikhonov, Twomey and a stochastic regularization method. The a priori information used for Twomey and stochastic regularization are obtained from those calculated epicardial potentials and only spatial regularization is used. The results show that the best solutions are obtained with stochastic regularization, but its computational cost is higher than others. Also Twomey regularization helps to avoid over-smoothing which is a typical problem for 0'th order Tikhonov regularization.

In another study the same group determines the slope of transmembrane potential and action potential propagation velocity using body surface potentials [51]. The importance of this study is that they optimize the excitation velocity for different tissues in the patient specific cellular automaton model such as bundle branches and Tawara nodes. By this way a model of the patients heart is constructed where the effects of therapy might be simulated as well as determination of the infarcted tissues.

Another study which tries to fit a model according to the measures BSP's is studied by He *et al.* for 3-D myocardium model [52]. In their study an anisotropic heart model is used to obtain more realistic results with different excitation velocities for longitudinal and transverse fiber direction and 82 different myocardial segments which results in 82 current dipoles are assumed. They also used cellular automaton model to simulate the BSP's. They first obtain the anatomical information with CT and used this data to build a thorax model. Then they optimize the parameters in their model with a comparison of measured and simulated BSP's. After that using those optimized parameters they determine the myocardial activation times. They have also published a similar study where they determine the transmembrane potentials [53].

2.6.3 Validation Studies and Human Experiments

The work by Nash *et al.* is important in the sense that it is an in vivo study that measures BSP's and epicardial potentials simultaneously [54]. Earlier studies uses in vitro experiments with a dog heart placed in a torso tank [55, 56] or does not have the needed resolution because of the technological limitations [57, 58]. In order to measure epicardial and body surface potentials simultaneously they implemented a sock electrode to the ventricles of a pig heart and the wire for epicardial measurements are exited near diaphragm. Also a suture snare is inserted to the left anterior descending (LAD) coronary artery to occlude it whenever necessary during experiment and they closed the chest. They have stated that with that experiment they were able to observe the slow conduction velocity at the ischemic region and measure the epicardial and BSP's simultaneously. As the authors stated this study could serve well to validate the inverse electrocardiography solutions.

Ramanathan *et al.* tested the technique they called electrocardiographic imaging which is same as inverse problem of electrocardiography for human subjects [6]. In their study they tested their imaging system for normal sinus rhythm, right bundle branch block, right and left ventricular pacing and atrial flutter. The first step at their system is the measurement of body surface potentials from 224 points with a vest electrode. Then they used CT with an axial resolution of 0.6 to 1 mm to obtain epicardial surface geometry and the positions of the vest electrodes. In the signal processing part, first the preprocessing module acquires ECG signals with noise filtration, baseline correction etc, at the second part the segmentation process is carried on and the CT images are got ready for calculating transfer matrix with BEM at the third step. Finally at the fourth step Tikhonov regularization and generalized minimum residual error algorithms are applied to the data to overcome ill-posedness of ECG signals. They obtained epicardial potential maps, epicardial electrograms, activation time isochrone maps and recovery times. Rudy *et. al.* also take the patent for that system in 2006.

2.6.4 Geometric Errors

As previously stated the geometric information regarding the thorax along with the conductivity values is a must for electrocardiographic imaging. This is because the transfer matrix that maps the cardiac activity to BSP's is used in both forward and inverse problems of elctrocardiography. But different kinds of errors are introduced to the system while the transfer matrix is calculated from the patient and those errors are called as geometric errors. The major sources of those errors are:

- Imaging modalities like CT and MRI are not perfect so errors in the locations and boundaries of the organs occur.
- Extra errors are introduced to the system in the segmentation step of the organ

boundaries.

- The numerical solvers also introduce errors due to discretization.
- Usually the movement of the heart is not considered during solution and the same transfer matrix is used for each phase of cardiac cycle.
- Non-invasive measurement of conductivities are not possible with current imaging modalities so approximate conductivity values are used for tissues.

There are many studies that deal with the effects of geometric errors for inverse problem of electrocardiography but those studies do not offer any method to reduce those affects [59, 28, 52, 60, 61, 62, 63]. Also those studies concluded that the errors in the locations and the size of the organs reduce the accuracy of the solutions more in comparison to errors occur due to conductivity values [28, 62]. Thus at this dissertation we will only study the affects of location and size errors at the organs and when we use the term geometric errors we will refer to those.

In their study Ramanathan *et al.* study the effects of torso inhomogeneities for body surface potential [60]. They used the frozen human torso cross-sections from the Library of Medicines Visible Human Project for realistic torso. They use actual measured epicardial potentials. They have studied normal sinus rhythm along with ventricular pacing to simulate ventricular arrhythmias with single and dual pacing. In their study they conclude that although differences in lung conductivities has some slight affects on amplitudes of body surface potentials no visible difference could be observed on potential patterns. The overall conclusion of this study was the torso inhomogeneities has small affects on amplitudes but does not affect the body surface potential patterns much. At this study also the need for a specific torso and heart geometry to obtain decent solutions are stressed along with the effects of smoothing for both homogeneous and inhomogeneous torso models.

Cheng *et al.*'s study is one of the most recent studies about geometric errors in inverse problem of electrocardiography [28]. At their study they examine the affects of signal (errors in signal amplitude and electrode locations for both correlated and uncorrelated cases), material (errors due to wrong conductivity assignments to the organs) and geometric (errors due to the wrong determination of size and location of the organs) errors. They obtain the solutions for both epicardial potential and activation based models and compare their performances for the existence of modeling errors. The inverse algorithms that are used to obtain epicardial potentials in this study are truncated singular value decomposition (TSVD), Tikhonov regularization and Greensite's algorithm. They use a method that benefits from critical point theorem to obtain activation time based solution [25]. Their results show activation based models are more immune to modeling errors than epicardial potential based methods. Also results show that geometric error is the most dominant modeling error (it leads to highest errors at the solution). The material errors have the least significant effect on solutions and the effects of signal errors are between those two. This study also shows the need for an inverse solution algorithm for cardiac imaging that could also address the geometric errors in the formulation.

Another interesting study is published by Jiang *et al.* [64]. In that study they tested the effects of heart motion by solving the problem for both static and dynamic models for epicardial potential based formulation. The motion of the heart is simulated only in the T period and this movement is simulated with mesh deformation. They use zero'th order Tikhonov regularization and generalized minimal residual error (GM-RES) to obtain solutions. Their results show improvements in correlation coefficient up to 0.1 with dynamic model for Tikhonov regularization but on the other hand no significant improvement observed for GM-RES. They stated that this shows that GM-RES is more immune to modeling errors.

CHAPTER 3

THEORY

3.1 Problem Definition

The relationship between body surface measurements and the electrical activity of the heart is usually represented with the equation below [13]:

$$\mathbf{Y} = \mathbf{H}(\mathbf{X}) + \mathbf{V} \tag{3.1}$$

where **X** is the matrix of parameters that defines the electrical activity of the heart, **Y** is the matrix of body surface measurements, **H** is the non-linear transfer matrix that is used to determine the torso measurements from the parameters that defines the electrical activity of the heart and **V** is the noise matrix which is usually assumed as Gaussian. The equation above represents the forward problem of electrocardiography which is the determination of torso measurements from the electrical activity of the heart.

The linearity of the relationship given in equation (3.1) changes for different parameters used to represent electrical activity at the heart. For example if activation times are used as **X** in equation (3.1) then **H** is a non-linear function. But if epicardial potentials are used as parameters **X** then the transfer matrix becomes linear. Also the values given in equation (3.1) can be discretized to be solved in computers. After those modifications the forward problem equation in terms of epicardial potentials and torso potentials takes the form given in equation (3.2). Also measurement noise (due to imperfections in the measurement devices, wrong modeling of transfer matrix etc.) is inserted to the system to obtain a more accurate formulation.

$$\mathbf{y}_k = \mathbf{H}\mathbf{x}_k + \mathbf{v}_k \tag{3.2}$$

where $\mathbf{x}_k$ is the $Nx1$ vector of epicardial potentials at time instant k, $\mathbf{y}_k$ is the $Mx1$ vector of body surface potentials at time instant k, $\mathbf{H}$ is the MxN linear transfer matrix and $\mathbf{v}_k$ is $Mx1$ measurement noise vector. The measurement noise is assumed as independent and identically distributed Gaussian noise vector with $\mathbf{v} \sim N(0, \mathbf{R})$. Also the measurement noise vector is assumed to be uncorrelated with epicardial potentials.

The transfer matrix $\mathbf{H}$ shown in equation (3.2) is calculated using the geometry and conductivities of the organs within the thorax using Boundary Element Method.

The solution strategies for the forward problem of ECG has been widely studied and its solution with Boundary element method (BEM) and Finite element method (FEM) can be found in the literature [13, 19]. In this thesis the BEM is used to obtain the forward transfer matrix. For that purpose the procedure described in the study of Barr *et al.* is used [65] using the forward solver that is developed by one of our group members.

The formulation given in equation (3.2) is also somewhat incomplete because the change of epicardial potentials with respect to time are not taken into consideration. To make up this deficiency an extra equation as shown below should be inserted to the formulation.

$$\mathbf{x}_k = \mathbf{F}\mathbf{x}_{k-1} + \mathbf{w}_k \tag{3.3}$$

In equation (3.3) the $\mathbf{F}$ is the NxN state transition matrix (STM) which determines the transition between the epicardial potentials of two consecutive time instants ($\mathbf{x}_{k-1}$ and $\mathbf{x}_k$) and $\mathbf{w}_k$ is the $Nx1$ process noise vector which is assumed as independent and identically distributed Gaussian noise vector with $\mathbf{w} \sim N(0, \mathbf{Q})$.

The main motivation of this thesis is to solve the inverse problem of ECG, which is defined as the estimation of electrical activity in the heart from torso measurements. The motivation behind this problem in terms of diagnostic purposes is more obvious than forward problem of ECG because normally the electrical activity within the heart cannot be measured but torso potentials can easily be measured. If the inverse problem of electrocardiography is formulized in terms of epicardial potentials and discretized, a linear formulation as shown below is obtained.

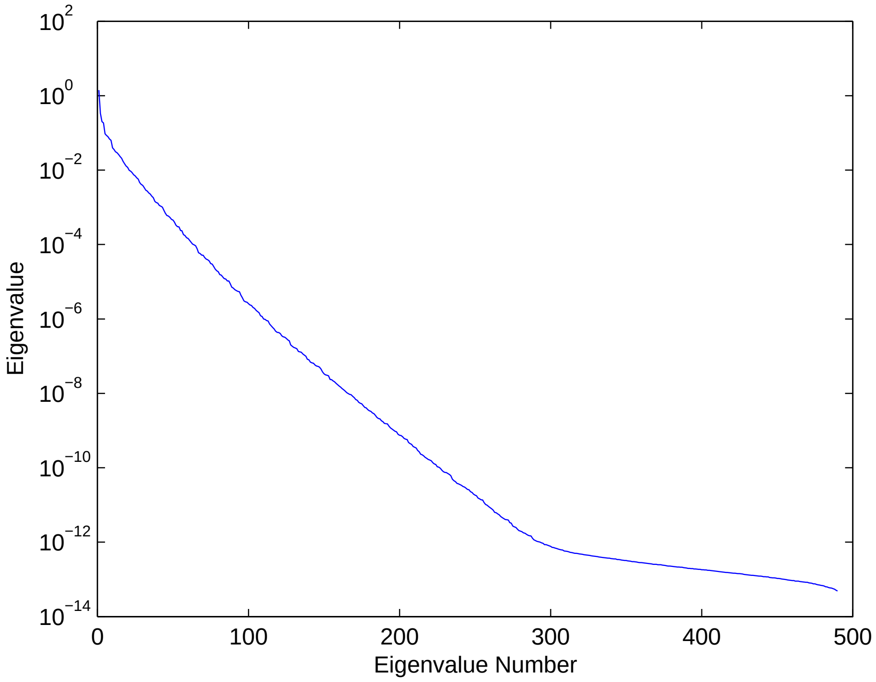

Figure 3.1: The plot of eigenvalues of a homogeneous transfer matrix obtained with BEM

$$\mathbf{x}_k = \mathbf{H}^{-1}\mathbf{y}_k; \tag{3.4}$$

Unfortunately the inverse problem of ECG can not be solved that easily because the condition number of the transfer matrix **H** is very high that, even a small noise resulted in very high errors in the solution. The condition number of a matrix is the ratio of the greatest eigenvalue to the smallest one. The plot of eigenvalues of one of the transfer matrices used in this study (for a homogeneous thorax model) is shown in Figure 3.1 and this matrix has a condition number $2.88e^{14}$.

In the previous paragraph it was mentioned that the solution of inverse ECG problem can not be obtained just by taking the inverse of the transfer matrix, because even small perturbations resulted in large errors in the solution. Those kind of problems are called as ill-posed problems (actually discrete ill-posed problem cause the formulation used here is discrete). In the literature those kind of inverse problems are usually solved with regularization methods like truncated singular value decomposition (TSVD), Tikhonov and Twomey regularization [32, 33, 34]. Also statistical estimation methods like Bayesian maximum *a posteriori* and Kalman filter were used [36, 38, 39, 40, 41].

In this thesis Tikhonov regularization, Bayesian-MAP and Kalman filter (smoother) algorithms are used to solve the inverse problem of ECG.

3.2 Inverse Problem Solution Algorithms

3.2.1 Tikhonov Regularization

Tikhonov regularization is the most widely used method to solve discrete ill-posed problems and the goal is to minimize the least squares solution given as [66]:

$$||\mathbf{Hx} - \mathbf{y}||_2^2 + \lambda \, ||\mathbf{Lx}||_2^2 \tag{3.5}$$

where $\mathbf{x}$ demonstrates the unknowns, $\mathbf{y}$ represents measurements, $\mathbf{H}$ is the forward transfer matrix, λ is the regularization parameter and $\mathbf{L}$ determines what to penalize. Here the first term determines the fit of the solution while the second term is used to constrain the solution. The regularization parameter determines the trade-off between data fit and the level of regularization. If the regularization parameter is large then the solution will be oversmoothed but if it is small than it cannot cope with the ill-posedness of the problem. Shortly, Tikhonov regularization works like a filter. It attenuates the effects of smaller singular values and thus reduce the effects of noise. The solution for the minimization problem given in equation (3.5) is:

$$\hat{\mathbf{x}} = (\mathbf{H}'\mathbf{H} + \lambda\mathbf{L})^{-1}\, \mathbf{H}'\mathbf{y} \tag{3.6}$$

The principles behind Tikhonov regularization can be understood much easier when the solution given in equation 3.6 is written with the help of singular value decompositon (SVD). In which the forward matrix $\mathbf{H}$ is written as

$$\mathbf{H} = \mathbf{USV}' \tag{3.7}$$

where $\mathbf{S} = s_1, ..., s_n$ is composed of singular values of $\mathbf{H}$. The $\mathbf{U}$ and $\mathbf{V}$ are matrices of right and left eigenvectors of $\mathbf{H}$ (or $\mathbf{H}^T\mathbf{H}$). The solution in terms of SVD becomes:

$$\hat{\mathbf{x}} = \sum_{i=1}^{n} \frac{s_i^2}{s_i^2 + \lambda^2} \frac{\mathbf{U}'_{:,i}\mathbf{y}}{s_i} \mathbf{U}_{:,i} \tag{3.8}$$

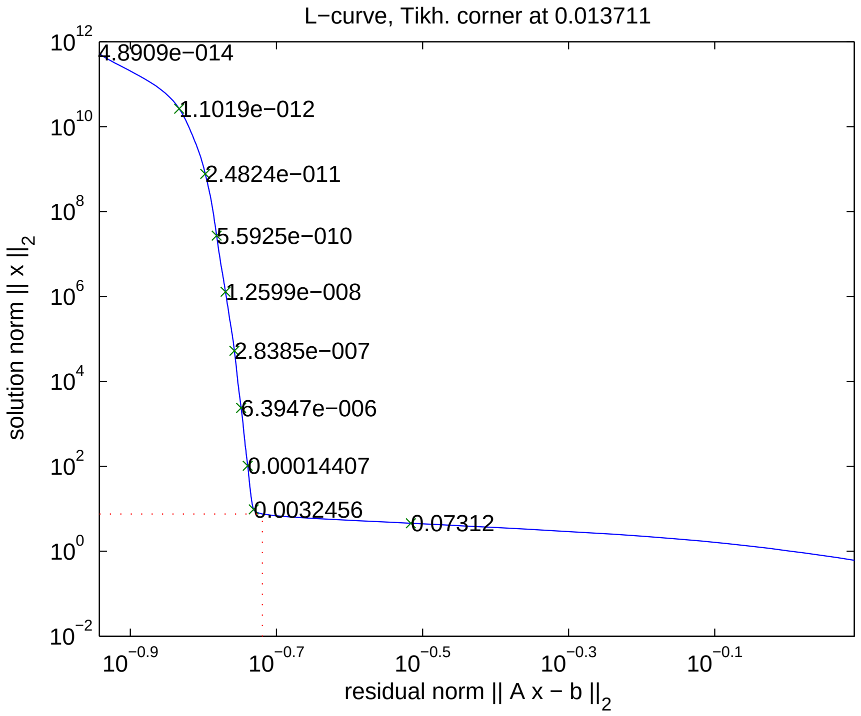

Figure 3.2: An example L-Curve plot for inverse ECG problem

It is clear from this formulation that the greater the singular values the higher its effect will be. Also the importance of the regularization parameter to obtain decent solutions is obvious in equation 3.8.

In this thesis regularization parameter is determined with L-Curve method [67]. In this method the residual $||\mathbf{Hx} - \mathbf{y}||_2^2$ and the constraint $||\mathbf{Lx}||_2^2$ are plotted for different regularization parameters and the one that corresponds to the optimal trade-off value between them is selected. The name of this method comes from the shape of the plot. As it can be seen in Figure 3.2 the logarithmic plot of residual and constraint norms has a shape like L. The parameter value at the corner of this curve is the optimal point and previous and later parameter values cause major increases in the norms.

3.2.2 Bayesian Maximum A Posteriori Estimation

In section 3.1 it is described that our goal is to find unknown $\mathbf{x}$ with given measurements $\mathbf{y}$. The $\mathbf{x}$ and $\mathbf{y}$ assumed as random variables. It is known from Bayesian philosophy that when the prior probability density function (pdf) of an unknown random variable $p(\mathbf{x})$ is given along with its conditional pdf $\mathbf{y}$ given $\mathbf{x}$ (likelihood function), the posterior conditional pdf $\mathbf{x}$ given $\mathbf{y}$ can be found from the equation below [68],

$$\mathbf{p}(\mathbf{x}\backslash\mathbf{y}) = \frac{\mathbf{p}(\mathbf{y}\backslash\mathbf{x})\mathbf{p}(\mathbf{x})}{\int_{\mathbf{X}} \mathbf{p}(\mathbf{y}\backslash\mathbf{x})\mathbf{p}(\mathbf{x})dx} \tag{3.9}$$

where $\mathbf{X}$ is the parameter space.

In Bayesian-MAP the solution $\hat{\mathbf{x}}$ that maximizes the posterior pdf is tried to be calculated:

$$\hat{\mathbf{x}} = argmax_x p(\mathbf{x}\backslash\mathbf{y}) \tag{3.10}$$

When the unknown $\mathbf{x}$ is assumed as epicardial potentials, the pdf of $\mathbf{x}$ can be assumed as normally distributed with mean $\overline{\mathbf{x}}$ and Covariance matrix with $\mathbf{C}_x$. Also the measurement noise $\mathbf{v}$ shown in equation (3.3) is assumed as independent and identically distributed Gaussian noise, so its pdf is $\mathbf{v} \sim N(\mathbf{0}, \mathbf{R})$ where $\mathbf{R} = \sigma_v^2\mathbf{I}$. Therefore the joint pdf is represented as [69]:

$$E\left\{\begin{pmatrix} \mathbf{x} \\ \mathbf{y} \end{pmatrix}\right\} = \begin{pmatrix} \overline{\mathbf{x}} \\ \mathbf{H}\overline{\mathbf{x}} \end{pmatrix} \tag{3.11}$$

$$\mathbf{C}_{\mathbf{x},\mathbf{y}} = \begin{pmatrix} \mathbf{C}_{\mathbf{x}} & \mathbf{C}_{\mathbf{x}}\mathbf{H}' \\ \mathbf{H}\mathbf{C}_{\mathbf{x}} & \mathbf{H}\mathbf{C}_{\mathbf{x}}\mathbf{H}' + \mathbf{R} \end{pmatrix} \tag{3.12}$$

Under these conditions the solution to the maximization problem shown in equation (3.10) can be obtained as:

$$\hat{\mathbf{x}} = \left(\mathbf{H}'\mathbf{R}^{-1}\mathbf{H} + \mathbf{C}_{\mathbf{x}}^{-1}\right)^{-1}\left(\mathbf{H}'\mathbf{R}^{-1}\mathbf{y} + \mathbf{C}_{\mathbf{x}}^{-1}\overline{\mathbf{x}}\right) \tag{3.13}$$

More detail about the Bayesian-MAP can be found in [68, 69].

3.2.3 Temporal Bayesian-MAP

The Bayesian-MAP approach described in 3.2.2 assumes no temporal correlation between epicardial potentials and thus solve each time instant separately. But electrical activity in the heart has temporal dependence too [13]. In order to include temporal information to Bayesian-MAP solution the isotropy assumption is used which is suggested by Greensite *et al.* [50, 47]. The isotropy is very similar to the separability condition for random variables. According to separability condition a spatio-temporal random variable's cross-covariance matrix $\mathbf{C_x}$ depends on temporal covariance matrix $\mathbf{C}_t$ and spatial covariance matrix $\mathbf{C}_s$ as shown below [47]:

$$\mathbf{C_x} = \mathbf{C}_t \otimes \mathbf{C}_s \tag{3.14}$$

where $\otimes$ is the kronecker product and:

$$E[\widetilde{\mathbf{X}}\widetilde{\mathbf{X}}'] = \mathbf{C}_s \sum_{j=1}^{N} t\mathbf{C}_t(j, j) \tag{3.15}$$

$$E[\widetilde{\mathbf{X}}'\widetilde{\mathbf{X}}] = \mathbf{C}_t \sum_{i=1}^{N} s\mathbf{C}_s(i, i) \tag{3.16}$$

With $\widetilde{\mathbf{X}}$ represents mean removed random variable.

From equations (3.15) and (3.16) $\mathbf{C_x}$ is written as:

$$\mathbf{C_x} = \frac{E[\widetilde{\mathbf{X}}'\widetilde{\mathbf{X}}] \otimes E[\widetilde{\mathbf{X}}\widetilde{\mathbf{X}}']}{\sum_{i=1}^{N} s\mathbf{C}_s(i, i) \sum_{j=1}^{N} t\mathbf{C}_t(j, j)} \tag{3.17}$$

Due to high memory requirement of the direct solution the solution should be modified to a column by column solvable formulation as in the spatial Bayesian-MAP. For that purpose the time correlation should be broken somehow. To break the the time correlation temporal whitening can be used. This method is simply using a transformation matrix $\mathbf{Z}$ such that the new coordinate system supplies the time independency that is required to solve the problem with spatial Bayesian-MAP. Then instead of solving the whole system at once, it could be solved column by column. By that way the memory consumption of the solution algorithm is reduced without ignoring the time dependency.

Choosing an appropriate transformation matrix which supplies the time decorrelation is very important to have minimum error using this assumption. For that purpose the transformation matrix should be chosen as orthogonal and also it should diagonalize $E[\mathbf{Y}'\mathbf{Y}]$. In previous studies that matrix ($\mathbf{Z}$) is chosen as eigenvectors of $E[\mathbf{Y}'\mathbf{Y}]$ and at that study it is chosen the same [37].

This process is called temporal whitening and the modified model for this system becomes [49]:

$$\mathbf{YZ} = \mathbf{HXZ} + \mathbf{VZ} \tag{3.18}$$

where $\mathbf{V}$ is the noise matrix with independent and identically distributed Gaussian assumption. Also equation (3.17) for $\mathbf{C_{xz}}$ becomes:

$$\mathbf{C_{xz}} = \frac{E[(\widetilde{\mathbf{X}}\mathbf{Z})'(\widetilde{\mathbf{X}}\mathbf{Z})] \otimes E[(\widetilde{\mathbf{X}}\mathbf{Z})(\widetilde{\mathbf{X}}\mathbf{Z})']}{E[\left\|\widetilde{\mathbf{X}}\right\|_F^2]} \tag{3.19}$$

where $||.||_F^2$ is the Frobenius norm.

When the system given in equation (3.18) is solved column by column with Bayesian-MAP formulation 3.13, the new unknown $\mathbf{XZ}$ is calculated. Finally using orthogonality of the transformation matrix $\mathbf{Z}$ the estimate for $\mathbf{X}$ is determined from:

$$\mathbf{X} = \mathbf{XZZ}' \tag{3.20}$$

More information about these derivations could be found in papers [50, 47, 49].

3.2.4 Kalman Filter and Smoother

The first implementation of the Kalman filter was a part of the space program directed by NASA (National Aeronautics and Space Administration) [70]. Since then the Kalman filter is used for a variety of problems from economy to biology [71, 72]. The main reason is its optimality in the mean square error sense with given a priori information and its ability to include uncertainties easily.

Using Kalman filter, processes that are represented with state space models can be solved and the inverse ECG problem can be represented with a state space model as shown in equations (3.2) and (3.3). Those equations are repeated below:

$$\mathbf{x}_k = \mathbf{F}\mathbf{x}_{k-1} + \mathbf{w}_k \tag{3.21}$$

$$\mathbf{y}_k = \mathbf{H}\mathbf{x}_k + \mathbf{v}_k \tag{3.22}$$

The derivations given in this section are modified from the books [73, 74, 75].

The Kalman filter is an estimator used to determine the most probable unknown states $\mathbf{x}_k^k$ and error covariance $\mathbf{P}_k^k$ with given measurements $\mathbf{Y}_k = \mathbf{y}_1, ..., \mathbf{y}_k$. Mathematically

$$\mathbf{x}_k^k = E(\mathbf{x}_k|\mathbf{Y}_k) \tag{3.23}$$

$$\mathbf{P}_k^k = E\{(\mathbf{x}_k - \mathbf{x}_k^k)(\mathbf{x}_k - \mathbf{x}_k^k)'\} \tag{3.24}$$

The Kalman filter is a two stage estimator. At the first stage *a priori* state estimation $\mathbf{x}_k^{k-1}$ and error covariance $\mathbf{P}_k^{k-1}$ are estimated with measurement $\mathbf{Y}_{t-1} = \mathbf{y}_1, ..., \mathbf{y}_{t-1}$

$$\mathbf{x}_k^{k-1} = E(\mathbf{x}_k|\mathbf{Y}_{k-1}) = E(\mathbf{F}\mathbf{x}_{k-1} + \mathbf{w}_k|\mathbf{Y}_{k-1}) = \mathbf{F}\mathbf{x}_{k-1}^{k-1} \tag{3.25}$$

$$\mathbf{P}_k^{k-1} = E\{(\mathbf{x}_k - \mathbf{x}_k^{k-1})(\mathbf{x}_k - \mathbf{x}_k^{k-1})'\} = \mathbf{F}\mathbf{P}_{k-1}^{k-1}\mathbf{F}' + \mathbf{Q} \tag{3.26}$$

At the second stage *a priori* state and error covariance that are shown in equations (3.25) and (3.26) are updated with the measurement at the last time instant $\mathbf{y}_k$. For that purpose first the innovations or residuals should be determined which are defined as

$$\epsilon_k = \mathbf{y}_k - E(\mathbf{y}_k|\mathbf{Y}_{k-1}) \tag{3.27}$$

The expectation of residuals is zero and its variance is

$$var(\epsilon_k) = \mathbf{H}_k\mathbf{P}_k^{k-1}\mathbf{H}_k' + \mathbf{R} \tag{3.28}$$

So,

$$\mathbf{x}_k^k = E(\mathbf{x}_k|\mathbf{Y}_k) = E(\mathbf{x}_k|\mathbf{Y}_{k-1}, \epsilon_k) = \mathbf{x}_k^{k-1} + \mathbf{K}_k\epsilon_k \tag{3.29}$$

$$\mathbf{P}_k^k = [\mathbf{I} - \mathbf{K}_k\mathbf{H}_k]\mathbf{P}_k^{k-1} \tag{3.30}$$

A posteriori error covariance could also be calculated with a different formulation. That formulation satisfies the need for $\mathbf{P}_k^k$ to be positive definite and symmetric which helps to avoid problems due to ill-conditioning.

$$\mathbf{P}_k^k = [\mathbf{I} - \mathbf{K}_k\mathbf{H}_k]\mathbf{P}_k^{k-1}[\mathbf{I} - \mathbf{K}_k\mathbf{H}_k]' + \mathbf{K}_k\mathbf{R}_k\mathbf{K}_k' \tag{3.31}$$

It is clear that the formulation above satisfies both symmetry and positive definiteness requirements. The symmetry is satisfied because the formulation compose of summation of two symmetric matrices so the result is symmetric too. Also the first term is a positive definite matrix and the second term is a nonnegative definite matrix whose sum is obviously a positive definite matrix [73]. In equation (3.31) $\mathbf{K}_k$ is the Kalman gain that decides the amount of correction to *a priori* estimates using the last measurement and formulated as:

$$\mathbf{K}_k = \mathbf{P}_k^{k-1}\mathbf{H}_k'(\mathbf{H}_k\mathbf{P}_k^{k-1}\mathbf{H}_k' + \mathbf{R})^{-1} \tag{3.32}$$

Equations (3.25), (3.26), (3.29), (3.31) and (3.32) are called the Kalman filter equations. This formulation is called Kalman filter because it uses all measurements up to the time instant that the state is going to be calculated. For example $\mathbf{x}_k$ is calculated with $\mathbf{Y}_k$. If $\mathbf{x}_k$ was calculated from $\mathbf{Y}_{k-1}$, it would be called an estimator. Actually equations (3.25) and (3.26) are estimation. Also if $\mathbf{x}_k$ is calculated from all measurements such that $\mathbf{Y}_n$ (where n is bigger than k) then it is called Kalman smoother. It is called smoother because the results are usually smoother than the filter results. In this study also Kalman smoother is used to further decrease errors.

The Kalman smoother does the backward recursion and requires the results of Kalman filter for the last time instant ($\mathbf{x}_n^n$, $\mathbf{P}_n^n$). Those equations to obtain Kalman smoother are given as:

$$\mathbf{J}_{k-1} = \mathbf{P}_{k-1}^{k-1}\mathbf{F}'[\mathbf{P}_k^{k-1}]^{-1} \tag{3.33}$$

$$\mathbf{x}_{k-1}^n = \mathbf{x}_{k-1}^{k-1} + \mathbf{J}_{k-1}(\mathbf{x}_k^n - \mathbf{x}_k^{k-1}) \tag{3.34}$$

$$\mathbf{P}_{k-1}^n = \mathbf{P}_{k-1}^{k-1} + \mathbf{J}_{k-1}(\mathbf{P}_k^n - \mathbf{P}_k^{k-1})\mathbf{J}_{k-1}' \tag{3.35}$$

where $k = n, ..., 1$

3.2.5 Determination of STM for Kalman Filter from Epicardial Potentials

For standard Bayesian-MAP and Tikhonov regularization algorithms only equation (3.2) is used but for Kalman filter approach also the equation (3.3) is used and the matrix **F** which is called state transition matrix (STM) should be determined. As can be seen from equation (3.3) STM maps the unknown states (epicardial potentials) at the previous time instant to the states at the next time instant thus contains the temporal information regarding the problem. For that reason unlike standard Bayesian-MAP and Tikhonov regularization techniques Kalman filter is a spatio-temporal method. To obtain a decent solution with Kalman filter the correctness of the STM is very important. But the determination of it for inverse ECG problem is not an easy task. In this subsection the technique that is suggested by Goussard *et al.* [39] is explained. In this technique the epicardial potentials are used to determine the STM. For that purpose they changed the formulation and assumed the epicardial potentials are known and it is STM which should be determined. Then they solved this formulation with a modified version of Kalman filter.

The new formulation where the unknown states are the elements of the STM is as:

$$\mathbf{x}_k = \mathbf{X}_{k-1}\mathbf{f} + \mathbf{w}_k \tag{3.36}$$

Where,

$$\mathbf{f} = \begin{pmatrix} \mathbf{f}_1 \\ \mathbf{f}_2 \\ \vdots \\ \mathbf{f}_N \end{pmatrix}, \ \mathbf{X}(k) = \begin{pmatrix} \mathbf{x}'^{(k)} & 0 & \cdots & 0 \\ 0 & \mathbf{x}'^{(k)} & \cdots & 0 \\ \vdots & \vdots & \ddots & \vdots \\ 0 & 0 & \cdots & \mathbf{x}'^{(k)} \end{pmatrix} \tag{3.37}$$

In equation 3.37 $\mathbf{f}_N$ is the transpose of the N'th row of STM matrix and $\mathbf{x}^T_{(k)}$ is the transpose of the epicardial potentials at time instant k.

As stated previously a modified version of Kalman Filter is used to solve this problem which is given as [39]:

$$\mathbf{K}_k = \mathbf{P}_k\mathbf{X}'_k \tag{3.38}$$

$$\mathbf{f}_{k+1} = \mathbf{f}_k + \mathbf{K}_k\mathbf{Q}{-}1\left(\mathbf{x}_{k+1} - \mathbf{X}_k\mathbf{f}_k\right) \tag{3.39}$$

$$\mathbf{Q}_k = \mathbf{I} + \mathbf{X}_k \mathbf{P}_k \mathbf{X}_k' \tag{3.40}$$

$$\mathbf{P}_{k+1} = \mathbf{P}_k - \mathbf{K}_k \mathbf{Q}_k^{-1} \mathbf{K}_k' \tag{3.41}$$

After rearranging the **f** as STM matrix, it could be used in Kalman Filter. For more detail on these one may refer to [39].

In this equation 3.41 **K** is the Kalman gain, **Q** is the covariance matrix of noise and **P** is the error covariance matrix.

This technique's high memory requirement is a major drawback. For an array of sensors that have measurements from 490 sensors the size of the error covariance matrix **P** becomes a matrix with size $490^2 x 490^2$ that requires approximately 429 GB of memory. In their work Goussard *et. al.* use the locality property to reduce the dimension of the problem by assuming a node is associated to only its neighbors. To avoid high memory problem we use the activation times of the nodes along with locality properties.

For that purpose first the activation time of each node is calculated using the second order differentials. Then the epicardial potential value at node (i) in time instant (k) is assumed as dependent to only the nodes at time instant (k-1) whose activation times are closed to the i'th. Only the elements of STM and so **f** that corresponds to those nodes are calculated and others are forced to zero. The rows of **X** in equation 3.37 corresponding to the elements that will be forced to zero at **f** has no effects on the calculated STM. For that reason those rows are deleted from the matrix which also reduces size of error covariance matrix at modified Kalman filter form $N^2 x N^2$ to $NDxND$ where N is the number of nodes on epicardium and D is the number of nodes that are assumed as associated to each other for each node. By benefiting from this property the memory consumption could be significantly reduced.

Usage of activation times also allow us to include physiological information to our problem solution. For example the nodes with close activation times probably corresponds to the fiber directions on the heart and so if the fiber directions are known the nodes that will be associated to each other could have chosen according to this information. This might save us from the obligation to calculate activation times for each node while introducing physiological constraints.

3.3 Enhanced Noise Model for Geometric Error Compensation

Modeling errors are very often in inverse problems. For inverse ECG problem those modeling errors may be due to discretization, wrong interpretation of electrode locations, wrong determination of heart's size and location and wrong conductivity assignments in the mathematical torso model. In the literature it can be seen that geometric errors have very significant effects in solutions [28]. As a part of this thesis geometric errors occur due to wrong size and location assignments to the heart are investigated. The effects of those geometric errors are also tried to be minimized with the modification of a method suggested by Kaipio *et. al.* for inverse problem solutions [76]. This model was implemented to optical tomography before [77] but to the best of our knowledge this is the first study that modifies this method to the inverse problem of electrocardiography.

In order to consider geometric errors the formulation of the system is changed as:

$$\mathbf{y} = \mathbf{H}(\mathbf{x}, \mathbf{z}) + \mathbf{v} \tag{3.42}$$

The difference in this formulation from others is that the transfer matrix is assumed as dependent on parameter vector $\mathbf{z}$. For inverse electrocardiography problem those parameters are the size and locations of each tissue that are present in the mathematical torso model.

If the true parameter vector is assumed as $\mathbf{z^*}$ and the parameter vector that are used in the inverse model are represented by $\mathbf{z}$, then it is clear that extra errors enter the system. For that case the formulation becomes [77]:

$$\mathbf{y} = \mathbf{H}(\mathbf{x}, \mathbf{z^*}) + (\mathbf{H}(\mathbf{x}, \mathbf{z}) - \mathbf{H}(\mathbf{x}, \mathbf{z^*})) + \mathbf{v} \tag{3.43}$$

In the formulation above $(\mathbf{H}(\mathbf{x}, \mathbf{z}) - \mathbf{H}(\mathbf{x}, \mathbf{z^*}))$ term represents the error due to uncertainties in the parameters of the transfer matrix. Those uncertainties may be due to wrong interpretations of the heart's size and location and thus this error represents the geometric errors in the problem. If that noise is assumed as $\epsilon(\mathbf{x}, \mathbf{z})$ then equation (3.43) becomes [77]:

$$\mathbf{y} = \mathbf{H}(\mathbf{x}, \mathbf{z*}) + \epsilon(\mathbf{x}, \mathbf{z}) + \mathbf{v} \tag{3.44}$$

For simplicity **H** is assumed as linearly dependent to parameters **z** and using Gaussian approximation geometric error is written as [77]:

$$\epsilon(\mathbf{x}, \mathbf{z}) = \mathbf{D_z H}(\mathbf{x}, \mathbf{z*})\delta_{\mathbf{z}} \tag{3.45}$$

With,

$$\delta_{\mathbf{z}} = \mathbf{z} - \mathbf{z}^* \tag{3.46}$$

In the formulation above $\mathbf{D_z}$ is the Jacobian matrix with respect to **z**. If the expectation of the geometric error is assumed as zero then the covariance of the geometric error is [77]:

$$E\left(\epsilon(\mathbf{x}, \mathbf{z})\epsilon(\mathbf{x}, \mathbf{z})'\right) = \Gamma_\epsilon = \mathbf{D_z H}(\mathbf{x}, \mathbf{z*})\Gamma_{\mathbf{z}}\mathbf{D_z H}(\mathbf{x}, \mathbf{z*})' \tag{3.47}$$

where,

$$\Gamma_{\mathbf{z}} = E\left(\delta_{\mathbf{z}}\delta'_{\mathbf{z}}\right) \tag{3.48}$$

Finally, benefiting from the independence assumption between geometric errors and measurement noise equation (3.43) is written as:

$$\mathbf{y} = \mathbf{H}(\mathbf{x}, \mathbf{z}^*) + \mathbf{e} \tag{3.49}$$

With the covariance matrix of **e** is $\Gamma_{\mathbf{e}} = \Gamma_\epsilon + \Gamma_{\mathbf{v}}$.

More detail on the proofs given in this part can be found in Kaipio *et. al.*'s book and journal so interested reader is encouraged to read those [77, 76].

To summarize, ENM allows the usage of $\Gamma_{\mathbf{e}}$ instead of measurement noise covariance **R** to reduce the effects of geometric errors in the inverse ECG problem.

3.4 System Identification Problem

The usage correct values of measurement and process noise covariances is critical to obtain decent solutions with inverse solution algorithms. In this section two different methods are described to determine the noise covariances for inverse ECG problem. The first method benefits from residuals and the other one uses expectation maximization. Those methods do not only used to calculate noise covariance matrices under normal conditions but also in the case of geometric errors. In that sense those methods are used to determine the noise covariances employed in enhanced noise model.

3.4.1 Determination of Measurement and Process Noise Covariance Matrices Using Residuals

As stated in 3.2.4 the values of measurement (**R**) and process (**Q**) covariance matrices should be known to use Kalman filter. As a part of this thesis those covariances are calculated from the residuals for inverse ECG problem such as Bailie and Jazwinski propose for orbit determination problem [78].

To calculate the noise covariances, first the residual should be calculated as:

$$r_k = \mathbf{y}(i)_k - \mathbf{H}(i)\mathbf{x}_k^{k-1} \tag{3.50}$$

$$\mathbf{R}(i)_k = r_k^2 - \mathbf{H}(i)\mathbf{P}_k^k\mathbf{H}(i)' \tag{3.51}$$

where i represents the row number and k is used to show time instant. So $\mathbf{H}(i)$ represents the i'th row of the forward transfer matrix. On the equations above if the value of $\mathbf{R}(i)_k$ is not positive then its value should be assigned as 0 [78]. Then $\mathbf{x}_k^k$, $\mathbf{P}_k^k$ and $\mathbf{x}_k^{k+1}$ are calculated with Kalman filter equations as [78]:

$$\mathbf{x}_k^k = \mathbf{x}_k^{k-1} + \mathbf{P}_k^{k-1}\mathbf{H}(i)'(\mathbf{H}(i)\mathbf{P}_k^{k-1}\mathbf{H}(i)' + \mathbf{R}(i)_k)^{-1}(\mathbf{y}(i)_k - \mathbf{H}(i)\mathbf{x}_k^{k-1}) \tag{3.52}$$

$$\mathbf{P}_k^k = \mathbf{P}_k^{k-1} - \mathbf{P}_k^{k-1}\mathbf{H}(i)'(\mathbf{H}(i)\mathbf{P}_k^{k-1}\mathbf{H}(i)' + \mathbf{R}(i)_k)^{-1}\mathbf{H}(i)\mathbf{P}_k^{k-1} \tag{3.53}$$

$$\mathbf{x}_{k+1}^k = \mathbf{F}\mathbf{x}_k^k \tag{3.54}$$

After the residual for k+1'th time instant is calculated from the formula given in equation (3.50), the process noise covariance elements are calculated as [78]:

$$\mathbf{Q}(i)_k = \frac{r_{k+1} - \mathbf{H}(i)\mathbf{F}\mathbf{P}_k^k\mathbf{H}(i)' + \mathbf{R}(i)_k}{\mathbf{H}(i)\mathbf{H}(i)'} \tag{3.55}$$

Again non-positive elements of covariance matrix are forced to zero. Finally error covariance matrix $\mathbf{P}_{k+1}^k$ is calculated with formulation below and the process continues.

$$\mathbf{P}_{k+1}^k = \mathbf{F}\mathbf{P}_k^k\mathbf{F}' + \mathbf{Q}(i)_k \tag{3.56}$$

More detail regarding the general formulations in this section can be found in [78].

3.4.2 Determination of Measurement and Process Noise Covariances Using Expectation Maximization

In this technique the likelihood is tried to be maximized for parameters $\Theta = [\mathbf{Q}, \mathbf{R}]$ [75, 79]. In expectation maximization (EM) algorithm the complete data likelihood with Gaussian assumption is written as [75, 79]:

$$\begin{aligned} -2ln\mathbf{L}_{\mathbf{X},\mathbf{Y}}(\Theta) &= ln\,|\Sigma_0| + (\mathbf{x}_0 - \mu)'\Sigma_0^{-1}(\mathbf{x}_0 - \mu) \\ &+ ln\,|\mathbf{Q}| + \sum_{k=1}^{n}(\mathbf{x}_k - \mathbf{F}\mathbf{x}_{k-1})'\mathbf{Q}^{-1}(\mathbf{x}_k - \mathbf{F}\mathbf{x}_{k-1}) \\ &+ ln\,|\mathbf{R}| + \sum_{k=1}^{n}(\mathbf{y}_k - \mathbf{H}\mathbf{x}_k)'\mathbf{R}^{-1}(\mathbf{y}_k - \mathbf{H}\mathbf{x}_k) \end{aligned} \tag{3.57}$$

where Σ and μ are the covariance and mean of the initial state vector $\mathbf{x}_0$. In EM algorithm maximizing the conditional expectation of the complete data likelihood with iterations is same as maximizing complete data likelihood. So at the j-th iteration [75, 79]:

$$\mathbf{Q}(\Theta|\Theta^{(j-1)}) = E\left\{-2ln\mathbf{L}_{\mathbf{X},\mathbf{Y}}(\Theta)|\mathbf{Y}_n, \Theta^{(j-1)}\right\} \tag{3.58}$$

The procedure have 4 steps and the iterations are $j = 1, 2, ...$

1. Initial parameter values $\Theta_{(0)} = [\mathbf{Q}, \mathbf{R}]$ are selected along with μ and Σ
2. The expectation step is performed. In this step the Kalman smoother estimations are used to calculate $\mathbf{S}_{11}$, $\mathbf{S}_{10}$ and $\mathbf{S}_{00}$ which forms the conditional expec-

tation of the complete data likelihood as below:

$$\begin{aligned}\mathbf{Q}(\Theta|\Theta^{(j-1)}) &= ln\,|\Sigma_0| + tr\left\{\Sigma_0^{-1}[\mathbf{P}_0^n(\mathbf{x}_0^n - \mu_0)(\mathbf{x}_0^n - \mu_0)']\right\} \\ &+ ln\,|\mathbf{Q}| + tr\left\{\mathbf{Q}^{-1}[\mathbf{S}_{11} - \mathbf{S}_{10}\mathbf{F}' - \mathbf{F}\mathbf{S}_{10}' + \mathbf{F}\mathbf{S}_{00}\mathbf{F}']\right\} \\ &+ ln\,|\mathbf{R}| + tr\left\{\mathbf{R}^{-1}\sum_{k=1}^{n}(\mathbf{y}_k - \mathbf{H}\mathbf{x}_k^n)' + \mathbf{H}\mathbf{P}_k^n\mathbf{H}'\right\} \qquad (3.59)\end{aligned}$$

With $\mathbf{S}_{11}$, $\mathbf{S}_{10}$ and $\mathbf{S}_{00}$ are as

$$\mathbf{S}_{11} = \sum_{k=1}^{n}(\mathbf{x}_k^n\mathbf{x}_k^{n\prime} + \mathbf{P}_k^n) \qquad (3.60)$$

$$\mathbf{S}_{10} = \sum_{k=1}^{n}(\mathbf{x}_k^n\mathbf{x}_{k-1}^{n}{}' + \mathbf{P}_{k,k-1}^n) \qquad (3.61)$$

$$\mathbf{S}_{00} = \sum_{k=1}^{n}(\mathbf{x}_{k-1}^n\mathbf{x}_{k-1}^{n}{}' + \mathbf{P}_{k-1}^n) \qquad (3.62)$$

The $\mathbf{P}_{k,k-1}^n$ is found using the lag-one covariance smoother whose formulation is as for $k = n, n-1, ..., 2$ [75, 79]:

$$\mathbf{P}_{k-1,k-2}^n = \mathbf{P}_{k-1}^{k-1}\mathbf{J}_{k-2}' + \mathbf{J}_{k-1}(\mathbf{P}_{k,k-1}^n - \mathbf{F}\mathbf{P}_{k-1}^{k-1})\mathbf{J}_{k-2}' \qquad (3.63)$$

With initial value as

$$\mathbf{P}_{n,n-1}^n = (\mathbf{I} - \mathbf{K}_n\mathbf{H})\mathbf{F}\mathbf{P}_{k-1}^{k-1} \qquad (3.64)$$

3. In this step as the name expectation maximization implies the expectation is tried to be maximized for parameters. So $\Theta^{(j)}$ is calculated with equations given below [75, 79]:

$$\mathbf{Q}^{(j)} = n^{-1}(\mathbf{S}_{11} - \mathbf{S}_{10}\mathbf{S}_{00}^{-1}\mathbf{S}_{10}') \qquad (3.65)$$

$$\mathbf{R}^{(j)} = n^{-1}\sum_{k=1}^{n}[(\mathbf{y}_k - \mathbf{H}\mathbf{x}_k^n)' + \mathbf{H}\mathbf{P}_k^n\mathbf{H}'] \qquad (3.66)$$

4. Next iteration starts from the second step with new parameter values.

More information about derivations can be found in [75, 79].

CHAPTER 4

RESULTS AND DISCUSSION

In this chapter first the data used for simulations are explained and then the reconstruction results for inverse problem of electrocardiography are given.

4.1 Simulated Data

The body surface potential measurements used in this study are simulated using the QRS intervals of measured epicardial potentials and an appropriate noise and forward model which is explained in detail later.

The epicardial potentials used for this study are measured at University of Utah Nora Eccles Harrison Cardiovascular Research and Training Institute (CVRTI) [56]. The measurements are taken from a dog heart which is perfused from another dog's circulatory system and suspended in an electrolytic filled (500Ωcm) adolescence human thorax shaped fiberglass tank. To measure the epicardial potentials a nylon sock electrode with silver wires is slipped over the ventricles. During measurements the heart is stimulated from the ventricles to simulate ventricular arrhythmias. The epicardial measurements are taken from 64 or 490 points with sampling rate 1000 sample per second.

The forward transfer matrix that maps epicardial potentials to body surface potentials is calculated with boundary element method from MRI images [1]. The thorax model consists of heart, torso and lungs. The conductivity values for thorax volume and lungs are taken from literature as 0.0002 S/mm and 0.00005 S/mm respectively [60].

---

[1] The forward solver is developed by Dr. Özlem Birgül

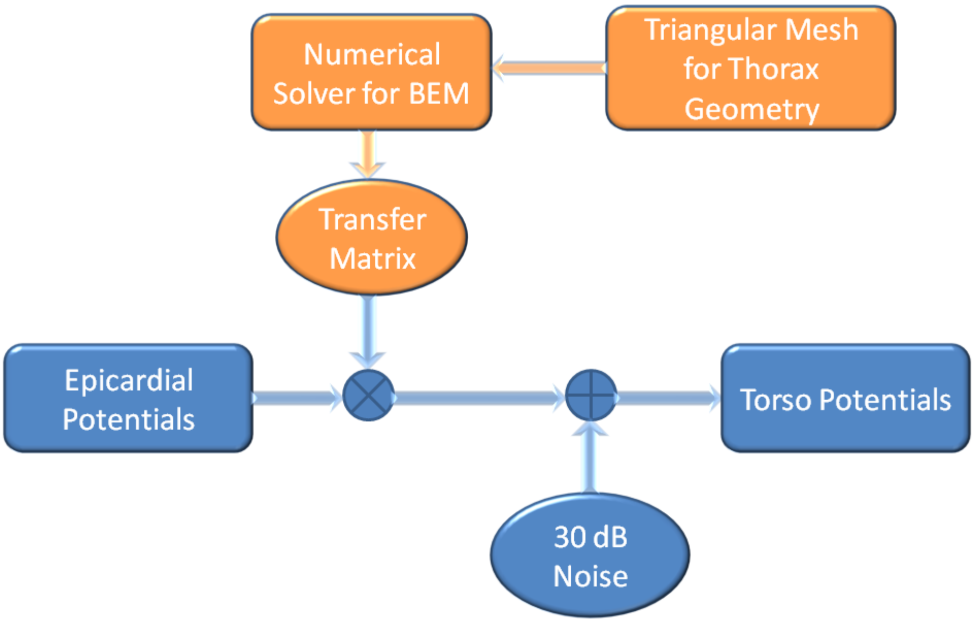

Figure 4.1: Schematic representation of the forward problem.

The forward transfer matrix is used to obtain 658 or 771 body surface potentials form epicardial potential measurements from 64 or 490 points respectively.

The body surface potentials are obtained from the epicardial potential measurements by a multiplication with the transfer matrix and addition of 30 dB SNR independent and identically distributed Gaussian noise. By doing so the forward problem of electrocardiography is solved. This process is shown in Figure 4.1.

4.2 Validation Methods

The quantitative comparisons of the solutions are made using correlation coefficients (CC) and relative difference measurement star (RDMS):

$$CC = \frac{N\left(\sum_{i=1}^{T}\mathbf{X}_i\widehat{\mathbf{X}}_i\right) - \left(\sum_{i=1}^{T}\mathbf{X}_i\right)\left(\sum_{i=1}^{T}\widehat{\mathbf{X}}_i\right)}{\sqrt{N\left(\sum_{i=1}^{T}\mathbf{X}_i^2\right)\left(\sum_{i=1}^{T}\mathbf{X}_i\right)^2}\sqrt{N\left(\sum_{i=1}^{T}\widehat{\mathbf{X}}_i^2\right)\left(\sum_{i=1}^{T}\widehat{\mathbf{X}}_i\right)^2}} \tag{4.1}$$

$$RDMS = \sqrt{\sum \left(\frac{\widehat{\mathbf{X}}_i}{\sum_{i=1}^{T} \widehat{\mathbf{X}}_i^2} - \frac{\mathbf{X}_i}{\sum_{i=1}^{T} \mathbf{X}_i^2} \right)^2} \tag{4.2}$$

As it is clear from their formulations that higher CC and lower RDMS correspond to better solutions. Although RDMS and CC give us information about the performances of the methods used for inverse electrocardiography problem, it is also important to compare original and reconstructed epicardial distributions visually. One of the reasons for this visual comparison is that the error measures used in this study cannot put necessary emphasis on true reconstruction of activation wavefront which is one of the most important features for inverse electrocardiography problem. For that purpose map3d software has been used which is a scientific visualization application written in Utah Nora Eccles Harrison Cardiovascular Research and Training Institute for the purpose of displaying and editing three-dimensional geometric models and time-based data associated with those models [80].

In Figure 4.2 the epicardial potential distribution and body surface potential map for a certain time instant which are plotted by map3d software are shown. In this figure red represents the regions that have not activated yet and the blue regions show the cells that have already been activated, the transition region between those two is the activation wavefront. While the results are compared with map3d two important characteristics are considered:

1. The solution's ability to follow the wavefront without dispersing it much. The dispersion in the wavefront is due to the regularization.

2. The solution's ability to correctly reconstruct the activated or inactivated regions.

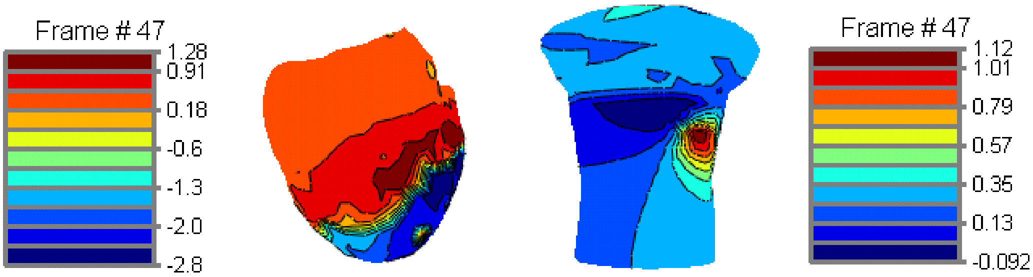

Figure 4.2: Sample epicardial and body surface potential potential maps plotted with map3d [80] for a certain time instant.

4.3 Reduction of the Problem Size for Inverse ECG Solution Using Kalman Filter

4.3.1 Comparison of the Reduced Formulation for STM Calculation with the Original One for 64 Node Data

In this subsection the algorithm suggested by Goussard *et al.* is implemented with some modifications to improve its performance. As explained in 3.2.5 they calculated the state transition matrix (STM) from epicardial potential (EP) measurements. The drawback of this approach is the high dimension of the problem when all nodes are assumed as related to each other. For example for N EP nodes the size of the error covariance matrix for full STM calculation algorithm is N^2xN^2. Although it could be calculated for 64 nodes (the memory requirement for error covariance matrix is 128 MB) for a model with higher resolution such as 490 epicardial nodes the memory requirement is approximately 430 GB. For that purpose Goussard *et al.* tries to benefit from the locality property of the problem and construct the STM as the EP at one time instant is related to only its 4 closest neighbors at the previous time instant. This assumption reduce the problem dimension significantly but introduce extra errors. In this part of the thesis we benefit from other characteristics of the propagating activation wavefront to achieve the reduction in the problem dimension without introducing extra errors. For that purpose strategies explained below are tested and a sample illustration of the nodes that corresponds to the scenarios explained are shown at Figure 4.3.

1. All nodes are assumed as related to each other which is called here as the full STM approach.
2. Only the first order neighbors are assumed as related to each other (approximately 7 node for each node).
3. Only the second order neighbors are assumed as related to each other (approximately 18 node for each node).
4. Only the nodes with close activation times are related to each other (within 11 ms threshold approximately 18 node).
5. The union set of the nodes that are found from both 1'st and 3'rd approaches are related to each other (within 4 ms threshold).

At this point extra information for the 3'rd and 4'th strategies might be needed. The motivation behind using those two strategies is to benefit from the relation between the signals that are along the same wavefront. In order to use those strategies at first the activation times for each node are determined by using the second derivative's of the EP's. The goal here is to relate those leads that are located on the same wavefront; i.e., those that are depolarized at the same time. For that purpose the activation time difference for each node is calculated and the nodes whose activation time difference are within a predetermined threshold are related to each other. The STM is calculated only for the entries that corresponds to those predetermined related nodes and other entries are forced to zero.

In this part of the study the STM is calculated from the test data itself. After the STM's are calculated according to the 5 scenarios, the inverse solutions are obtained by processing the data first with Kalman filter and then with Kalman smoother. The schematic representation of the simulation procedure is shown at Figure 4.4.

At the first step the simulations are conducted with EP measurements from 64 nodes to test the performances of the strategies 2 to 5 compared to the calculation in which full STM is used (strategy 1).

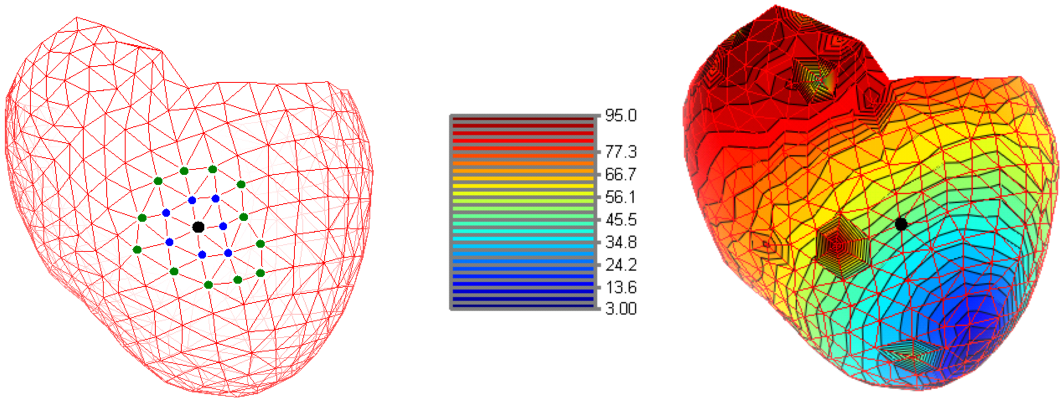

(a) 1’st and 2’nd order neighbors for node 230

(b) The isochrone map

Figure 4.3: The nodes that are related to 230’th node for STM calculation for different scenarios for the case of 490 epicardial nodes. In (a) The blue dots are the 1’st order neighbors and the union of blue and green dots are the 2’nd order neighbors while the black dot is the node 230. In (b) the isochrone map for the activation times is shown and the nodes at the same isochrone are related to each other.

Table 4.1: Means and standard deviations of CC and RDMS values, average related node numbers and the time consumptions of different scenarios to reduce the problem dimension of STM calculation for 64 node case. The threshold values for activation time based solutions are given in parenthesis near scenario name.

Scenario name	Mean CC ± std	Mean RDMS ± std	Node Number	Time consumption (sec)
Full STM	0,94 ± 0,17	0,22 ± 0,28	64	66
1’st Order Neighbors	0,89 ± 0,23	0,34 ± 0,33	7	3
2’nd Order Neighbors	0,93 ± 0,17	0,25 ± 0,27	18	6
Activation Based (11 ms)	0,92 ± 0,20	0,26 ± 0,30	18	6
Activation (4 ms) and 1’st Neighbor Union	0,93 ± 0,19	0,24 ± 0,30	12	4

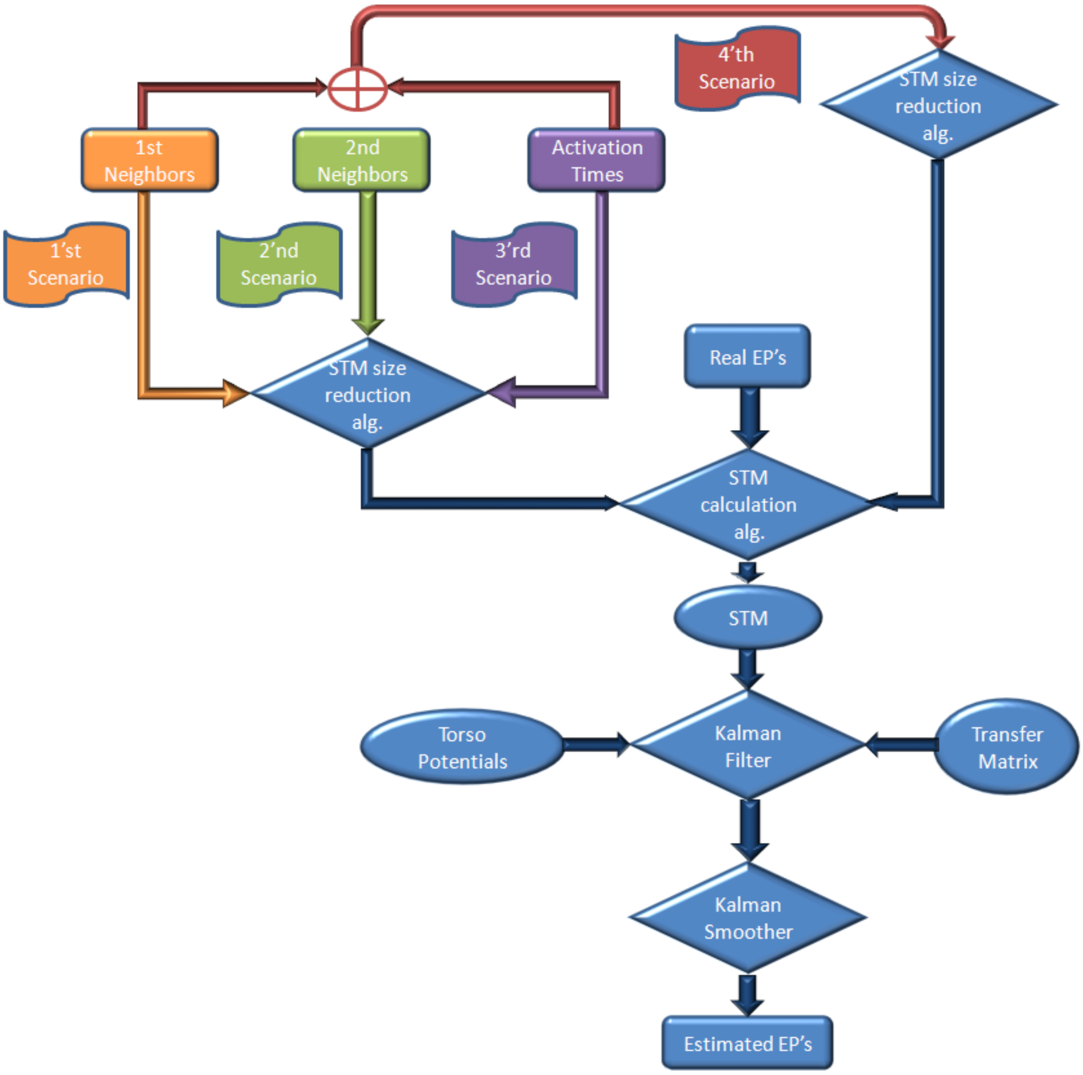

Figure 4.4: Schematic representation of the simulation procedure. Scenario 1 is the one that relates only 1'st order neighbors, scenario 2 relates only 2'nd order neighbors, scenario 3 relates only the nodes with close activation times and scenario 4 relates the union of the ones with very close activation time and 1'st order neighbors for STM calculation.

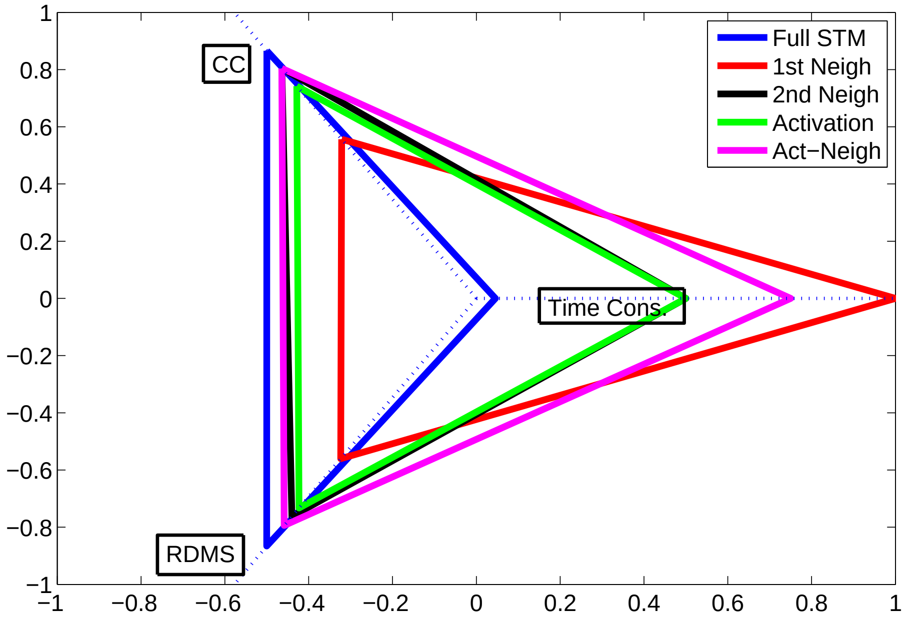

Figure 4.5: Starchart representation of time consumption, CC and RDMS.

In Table 4.1 the averages of CC and RDMS for the previously described strategies are given. The node number shows the average number of nodes that are related to one node. This number also corresponds to the average number of non-zero entries of the STM for one row. It can be seen that full STM approach has the best error performance. But other approaches except the one that uses 1'st order neighbors, have very similar performances to full STM approach, although the problem dimension and computation time are significantly decreased. The reason for this result can be understood when the entries of the full STM is studied. In full STM most of the entries are so close to zero which means that they have no significant relation for the corresponding nodes. Also if the entries with the highest values are checked it can be seen that the nodes that correspond to those entries are not only the neighbors. Sometimes the entry corresponding to two nodes with far locations is very high which contradicts to the assumption of using only the locality property of the activation wavefront propagation. When those related nodes are studied further, a pattern appears and it can be seen that those nodes are the ones that are along the same activation wavefront. This result also demonstrates the logic behind using not only local neighbors but also the ones with close activation times. The same results could be observed from Figure 4.5 too. At that chart CC, RDMS and time consumption of the algorithms are plotted on three dashed lines with 120 degree between them. In this plot the algorithm which crosses the dashed line at the outer most point has the best performance in the criteria that dashed line represents.

The interpretations made for Table 4.1 are also verified by Figure 4.6. This figure shows the epicardial distributions calculated at 37 ms after the stimulation with the scenarios described previously. Those results also indicate that there is no obvious difference between using the full STM, 2’nd order neighbor, activation based and activation union 1’st neighbor scenarios. Close correspondence of those solutions to the real epicardial potential distribution is also observed.

The results presented here show that the inverse problem of ECG could be solved without using the full STM because most of the entries of that STM is very close to zero. Also the nodes that should be related to each other can be determined benefiting from not only the locality property but also the shape of the wavefront. One possible question is how to determine those nodes along the same wavefront for real case. There are two possible answers to this question. The first one is, the approximate activation times could be determined from the pre-solutions obtained with other methods like Bayes-MAP or Tikhonov regularization and and the second one is, if the fiber directions are known the nodes along those fiber directions could be used as those along the same activation wavefront.

4.3.2 Comparison of the Proposed Problem Dimension Reduction Techniques for STM Calculation with 490 Node Data

The reason for using the data with 64 epicardial nodes previously was to assess the performance when problem dimension is reduced and the results show no significant reduction in the performance. Here those scenarios except the full STM scenario (due to its very high computational cost) ,for a problem with higher resolution which tries to find the EP’s from 490 nodes using BSP’s from 771 nodes, are tested.

The simulation procedure is same as in subsection 4.3.1 and only the threshold values

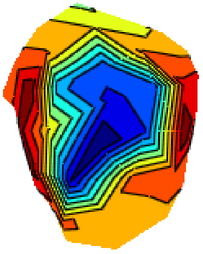

(a) Real Distribution

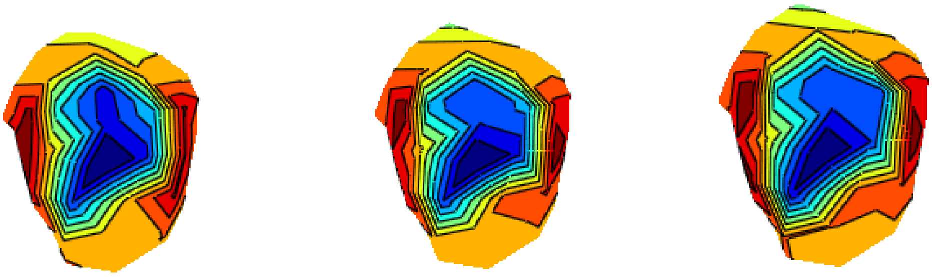

(b) 1’st Neighbor (c) 2’nd Neighbor (d) Activation Based

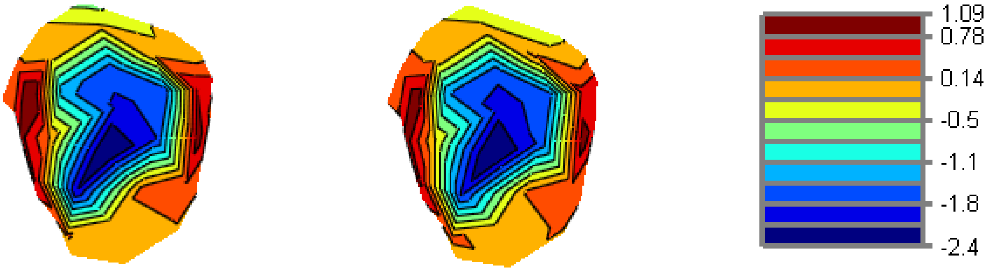

(e) Activation 1’st Neighbor Union (f) Full STM (g) Colormap

Figure 4.6: Epicardial potential map for 64 node solution with 37 ms after the first stimulus.

Table 4.2: Means and standard deviations of CC and RDMS values, average related node numbers and the time consumptions of different scenarios to reduce the problem dimension of STM calculation for 490 node case. The threshold values for activation time based solutions are given in parenthesis near scenario name.

Scenario name	Mean CC ± std	Mean RDMS ± std	Node Number	Time consumption (sec)
1’st Order Neighbors	0,89 ± 0,11	0,42 ± 0,13	7	3
2’nd Order Neighbors	0,92 ± 0,10	0,35 ± 0,16	18	6
Activation Based (3 ms)	0,91 ± 0,11	0,37 ± 0,14	19	6
Activation (1 ms) and 1’st Neighbor Union	0,93 ± 0,10	0,32 ± 0,15	14	4

for activation based scenario are reduced due to the increase in epicardial nodes.

In Table 4.2 the average CC and RDMS values for the corresponding scenarios are given. The node number shows the average number of nodes that are related to one node which is the same as the average non-zero entries at the STM for one row. Also in Figure 4.7 CC, RDMS and computation times are given with a graphic representation. Possible interpretations from those results are:

- The first order neighbors based solution has the worst error performance.
- The best error performance is achieved by union of activation time and 1’st order neighbors eventhough this solution relates only 14 epicardial nodes at the calculated STM. Which means less computational cost comparison to activation based and 2’nd order neighbor solution.
- Second order neighbor solution performs slightly better than the activation based solution.

As stated previously the quantitative error measures are not sufficient alone to compare results for inverse electrocardiography so along with those the epicardial potential distributions should be studied which are given in Figure 4.8. The results shown at Figure 4.8 prove the accuracy of that. These maps show that:

- The first order neighbor solution suffer from severe dispersion at the activation wavefront compared to the actual potential map.

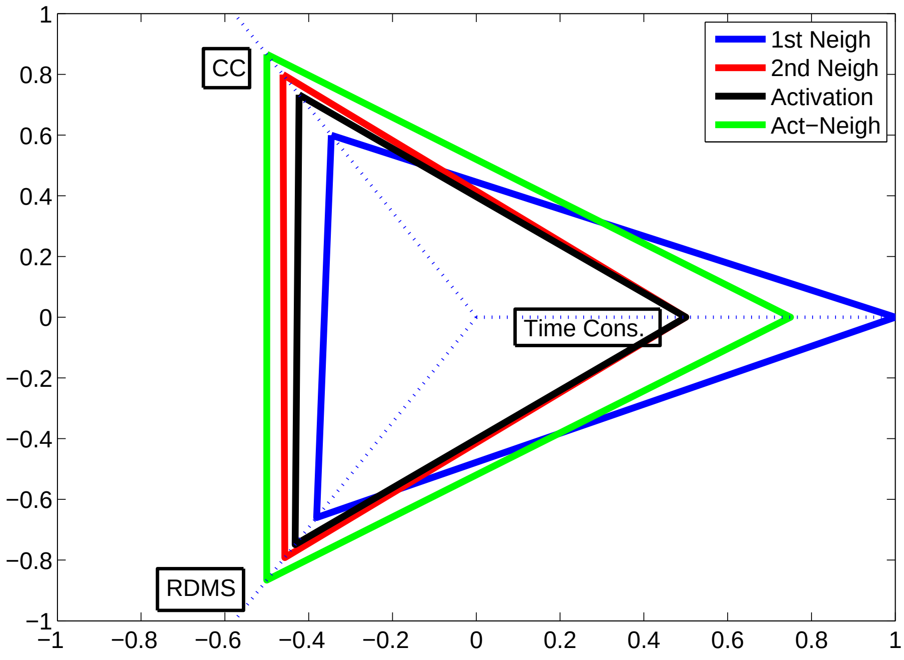

Figure 4.7: Starchart representation of time consumption, CC and RDMS.

- The second order neighbor solution reduce the dispersion at the activation wavefront but still the smoothing affect is obvious.

- The activation based solution does not have the activation wavefront dispersion problem from which both first and second order neighbor solutions suffer. But this approach suffers from another problem which is the false activated regions that do not exist neither in the actual map nor in the neighborhood based models.

- The union of activation and first neighbor solution seems to benefit from the advantages of both neighborhood and activation based methods. It follows the wavefront much better than neighborhood based methods and does not have the false activated areas reconstructed in the activation based method.

From Table 4.2 the second order neighbor method seems to perform better in error metrics compared to the activation based method but from Figure 4.8 it is seen that the activation time based method constructs the wavefront better. The reason for this is quite simple. The neighborhood based methods result in spatial smoothing due to the locality they benefit from so the activation wavefront is also smoothed along with the inactivated and activated regions. The activation time based method is not affected from this smoothing because it relates only those nodes that are on the same activation wavefront. But due to the lack of the spatial smoothing the false regions are not corrected in the activated and inactivated regions. On the other hand the union of activation and first order neighbor avoids the smoothing at the wavefront due to the related activation nodes and it avoids the false regions at activated or inactivated regions with benefiting from the spatial smoothing of first order neighbors.

The conclusion of this part of the study is neither neighborhood nor activation based methods are the best choices alone to determine nodes that should be related to each other for STM determination. The best choice is using both of them which results in better solutions with very significant reduction at the computational cost.

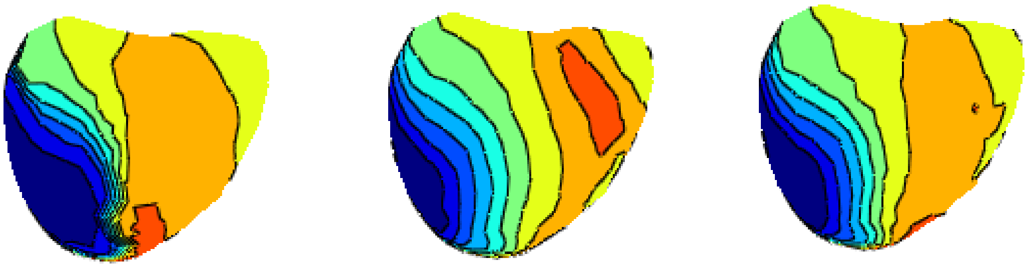

(a) Real Distribution (b) 1’st Neighbor (c) 2’nd Neighbor

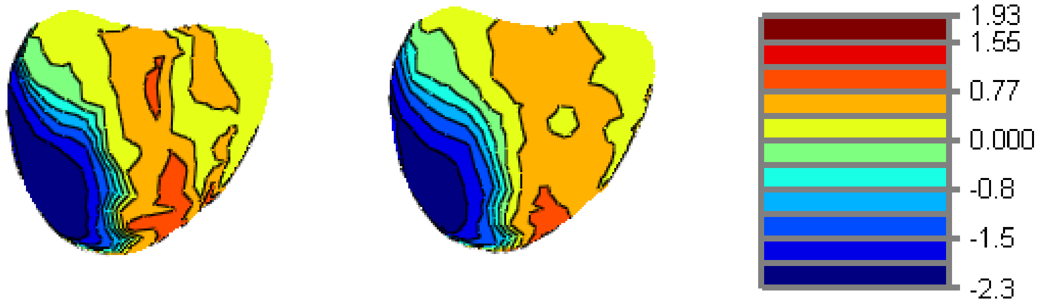

(d) Activation Based (e) Activation 1’st Neighbor Union (f) Colormap

Figure 4.8: Epicardial potential map for 490 node solution at 57 ms after the first stimulus.

4.4 Studies on the Calculation of State Transition Matrix without Using Real Epicardial Potentials

In the previous section the emphasis was on the reduction of the problem dimension to calculate the STM. The STM's calculated in the previous section requires the epicardial potential distributions of the test data itself which is obviously not possible in a realistic application. Those studies are helpful to show us that if appropriate *a priori* information can be acquired the STM calculation described at the previous section could be used to solve inverse electrocardiography problem with very high correlations.

In this section our objective is to present ways to obtain the *a priori* information needed to calculate the STM and compare those results with other spatial and spatio-temporal techniques. For that purpose we have used the following techniques:

1. **Bayes-Train:** The spatial Bayes-MAP solution obtained using the mean and covariance from the training set
2. **Tikhonov:** The zero'th order Tikhonov regularization solution
3. **Temp-Bayes:** The spatio-temporal Bayes-MAP solution with *a priori* information from the training set
4. **Kalman-Bayes:** The training set is used to obtain the solution using the spatial Bayes-MAP (Bayes-Train) and then this solution is used to calculate STM.
5. **Kalman-Tikh:** The solution of zero'th order Tikhonov regularization is used to calculate STM.
6. **Kalman-Direct:** A training set is used to calculate the STM directly which is suggested by Goussard *et al.* [39]

The BSP's that are used for inverse solutions are produced same as previous section. So epicardial potentials from 490 nodes are multiplied with the transfer matrix calculated with BEM and finally 30 dB white Gaussian noise is added to obtain noisy BSP's.

The training set used at this study is constructed from 8 different epicardial potential distributions which contains only the QRS intervals, with duration of 97 ms. The epicardial potential maps used in training set are all stimulated from the ventricles of the same dog heart but the location of the first stimulus site is different for each of them so the epicardial potential distributions are different. The test data is not included to the training set. The construction of training set for Bayes-Train and Kalman Direct differs from the temporal training set used for Temp-Bayes.

The 490x776 training set $\mathbf{X}_s$ for Bayes-Train is constructed by adding the epicardial potential distribution for each data column by column as shown below.

$$\mathbf{X}_s = [\mathbf{X}_1 \quad \mathbf{X}_2 \quad \cdots \quad \mathbf{X}_8] \tag{4.3}$$

Where 490x97 matrix X_i is the matrix that contains epicardial potential maps at 97 different time instants of the QRS interval for the i'th beat in the training set. The number of columns at X_i represents the number of time instants at which the epicardial potentials are measured and the number of rows are equal to the number of nodes on the epicardium. The priori mean for each node is found by averaging the rows of the training set over time and covariance matrix is found from equation given below.

$$\mathbf{C}_s = \frac{\mathbf{X}_s \mathbf{X}_s^T}{N_T} \tag{4.4}$$

Where N_T is the total number of time instants, which is 8x97 = 776. In this study it is clear that the resulting 490x490 covariance matrix $\mathbf{C}_s$ contains only spatial information.

For the Temp-Bayes algorithm the temporal covariance matrix $\mathbf{C}_t$ is also needed along with the spatial covariance matrix $\mathbf{C}_s$. In order to construct the 3920x97 training set $\mathbf{X}_t$ for temporal information, the 490x97 X_i epicardial potential map matrices are added row by row so:

$$\mathbf{X}_t = \begin{bmatrix} \mathbf{X}_1 \\ \mathbf{X}_2 \\ \vdots \\ \mathbf{X}_8 \end{bmatrix} \tag{4.5}$$

Then the temporal training set $\mathbf{C}_t$ is calculated with the formulation below:

$$\mathbf{C}_t = \frac{\mathbf{X}_t \mathbf{X}_t^T}{N_S} \tag{4.6}$$

where N_S is the row number of $\mathbf{X}_t$ and corresponds to the number of epicardial nodes.

The regularization parameter for zero'th order Tikhonov regularization is calculated using the L-Curve method [67] and a different regularization parameter is used for each time instant.

For Kalman-Bayes solution first the Bayes-Train solution is obtained. Then the epicardial potential map obtained from those are assumed as the real epicardial potential map and the activation time for each node is calculated from those. Finally the STM is calculated with using the problem dimension reduction technique described in 4.3. The procedure for Kalman-Tikh is the same as Kalman-Bayes only this time the solution of Tikhonov is used to find the STM instead of Bayes-Train.

The Bayes-Train and Tikhonov algorithms benefit from only spatial information to constrain the solution so these are called as spatial methods. On the other hand Kalman-Direct, Kalman-Bayes, Kalman-Tikh and Temp-Bayes benefit from both temporal and spatial constraints so those are spatio-temporal constraints. In this section also spatial and spatio-temporal methods are compared for the solution of inverse electrocardiography problem.

The schematic representation of the simulation procedure for methods Bayes-Train, Tikhonov, Kalman-Bayes, Kalman Tikh and Kalman-Direct is given at Figure 4.9

In Table 4.3 the average CC and RDMS values obtained for the algorithms explained above are given. In Figure 4.10 the performances of the algorithms in terms of CC, RDMS and computation time are shown. At this plot the algorithm which crosses the dashed line at the outer most point has the best performance in the criteria that dashed line represents. The interpretations from this table and plot are:

- Tikhonov solution has the worst performance in terms of error metrics.

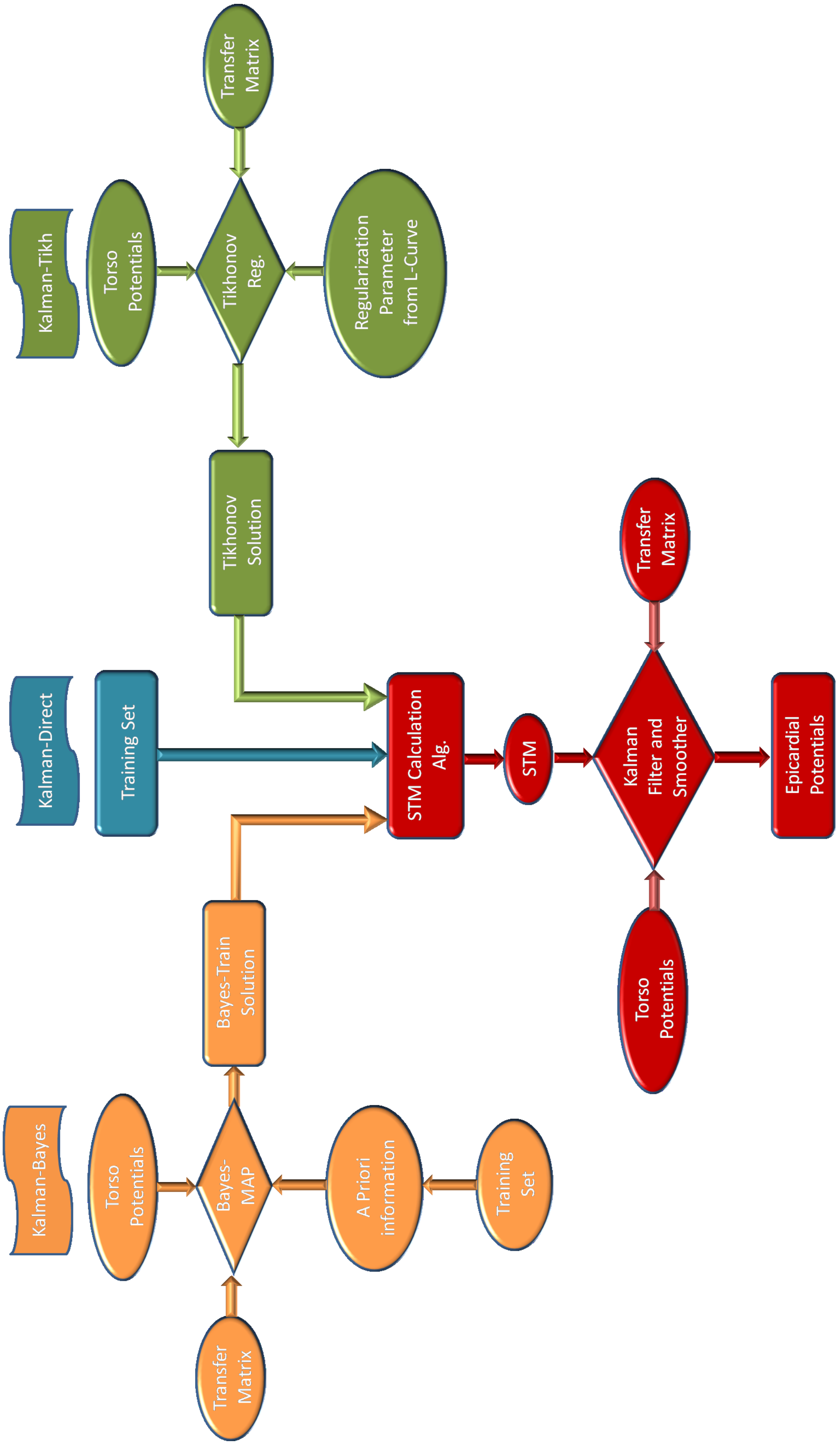

Figure 4.9: Schematic representation of the simulation procedure for Bayes-Train, Tikhonov, Kalman-Bayes, Kalman-Tikh and Kalman-Direct approaches

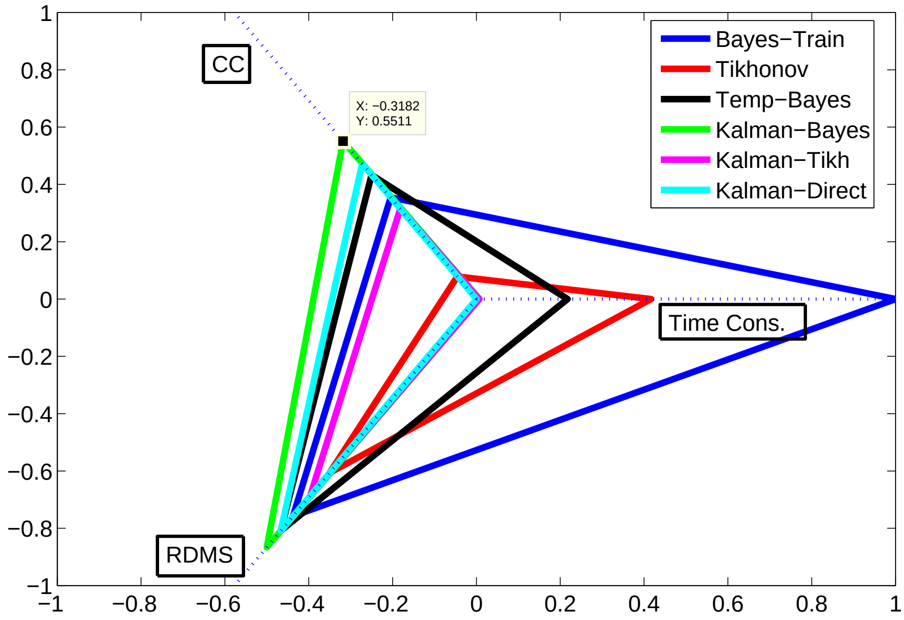

Figure 4.10: Starchart representation of time consumption, CC and RDMS.

- The Kalman-Tikh algorithm improves the results of Tikhonov solution significantly.

- The worst error performance after Tikhonov and Kalman-Tikh belongs to Bayes-Train solution.

- Eventhough Kalman-Tikh does not benefit from a priori information from any training set, its result is almost the same as Bayes-Train when CC's are considered but in terms of RDMS Bayes-Train is much better than Kalman-Tikh. Better RDMS means the relative potential map is constructed better and CC considers not only relative maps but also the amplitudes of the result.

- Usage of temporal information with Temp-Bayes improves the performance compared to the Bayes-Train but the improvement is limited. The advantage of this approach is its lower computational time compared to other spatio-temporal methods that are used in this study..

- Kalman-Real has the best error performance as expected because it uses the test data itself to calculate STM.

Table 4.3: Means and standard deviations of CC and RDMS values for spatial and spatio-temporal methods.

Scenario name	Mean CC ± std	Mean RDMS ± std	Time consumption
Bayes-Train	0,84 ± 0,19	0,48 ± 0,26	5 sec
Tikhonov	0,77 ± 0,20	0,60 ± 0,20	12 sec
Temp-Bayes	0,86 ± 0,17	0,45 ± 0,24	23 sec
Kalman-Bayes	0,89 ± 0,13	0,42 ± 0,21	695 sec
Kalman-Tikh	0,83 ± 0,11	0,53 ± 0,16	702 sec
Kalman-Direct	0,87 ± 0,12	0,45 ± 0,21	158 min
Kalman-Real	0,97 ± 0,08	0,20 ± 0,10	690 sec

- Kalman-Bayes has the best error performance if Kalman-Real is omitted. Kalman Direct is only slightly better than Temp-Bayes but its computational cost is very high. Also the computational cost increases as the number of beats included in the training set are increased because the number of recursions increase. On the other hand for Kalman-Bayes the computational time does not increase as in Kalman-Direct when the number of beats included to the training set increases, because in any case the number of recursions needed will be the same as the time instants of the test data itself.
- The usage of Kalman filter with *a priori* information from Bayes-Train improves the results of Bayes-Train.
- Overall it could be stated that spatio-temporal algorithms have better performance than spatial methods and the best performance among the spatio-temporal methods in terms of error metrics is belong to the Kalman-Bayes.

The epicardial potential map for 45 ms after the first stimulus are shown in Figure 4.11 respectively. The interpretations from those models are:

- The Kalman-Tikh improves the Tikhonov solutions significantly.
- Temp-Bayes and Kalman-Bayes solutions show some improvements comparison to Bayes-Train in terms of wavefront dispersion and false activated regions.
- Kalman-Direct and Kalman-Real solutions have the best performances in constructing the wavefront truly.

- Although in terms of error metrics Kalman-Bayes is better than Kalman-Direct, when epicardial maps are studied visually it is seen that Kalman-Direct performs better to avoid dispersion at the wavefront. Kalman-Direct is also better than the Temp-Bayes and its solution is close to the Kalman-Real case. But it is also observed during our studies that the performance of the Direct-Kalman approach depends on the sequence of the maps used in the training set due to the recursive algorithm used to obtain STM. For example the result presented here obtained when the last element of the training set is the propagation map initiated from the first order neighborhood of the test data. When the sequence of propagation maps is reversed the solutions of Kalman-Direct become even worst than Bayes-Train.

Figure 4.12 shows the CC and RDMS plots for different time instants. From those plots:

- The error metrics are worst at the initial and final time intervals. The possible explanation of this poor performance is the lower values of the RMS signal at those time instants due to the the small size of the activation wavefront at the initial and final time instants.
- Tikhonov and Kalman-Tikh solutions can compete with other methods at the initial time interval but especially after 60 ms these two solutions are significantly worse than other solutions.

The interpretations in terms of temporal information can better be made when the estimated epicardial potential signals for one node are plotted versus time as seen in Figure 4.13. From that figure it can be seen that the the solutions of spatio-temporal methods are more similar to the real one compared to spatial methods. Also due to temporal constraints used the spatio-temporal methods are much smoother than spatial methods with respect to time.

To summary of the conclusions for this section are:

- The solutions of other inverse ECG algorithms could be used to solve inverse

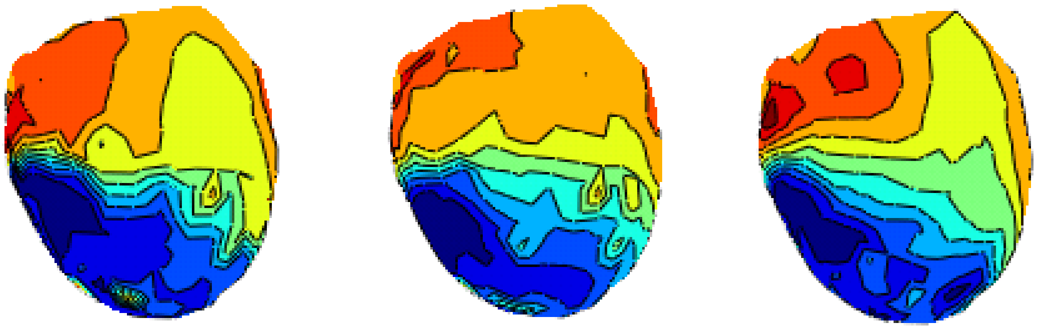

(a) Real Distribution (b) Bayes-Train (c) Tikhonov

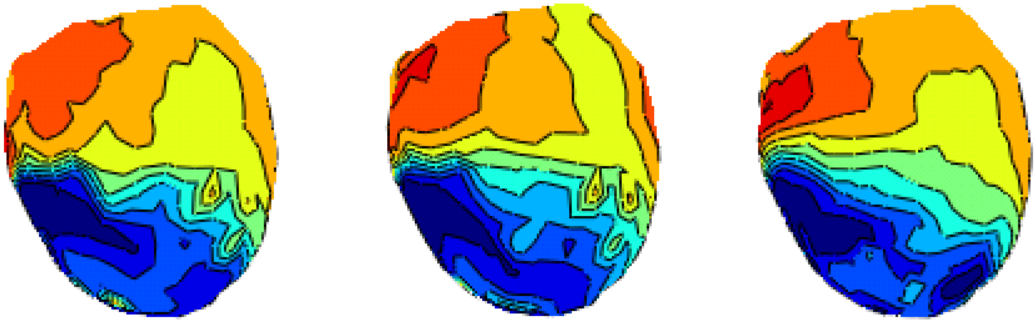

(d) Kalman-Direct (e) Kalman-Bayes (f) Kalman-Tikh

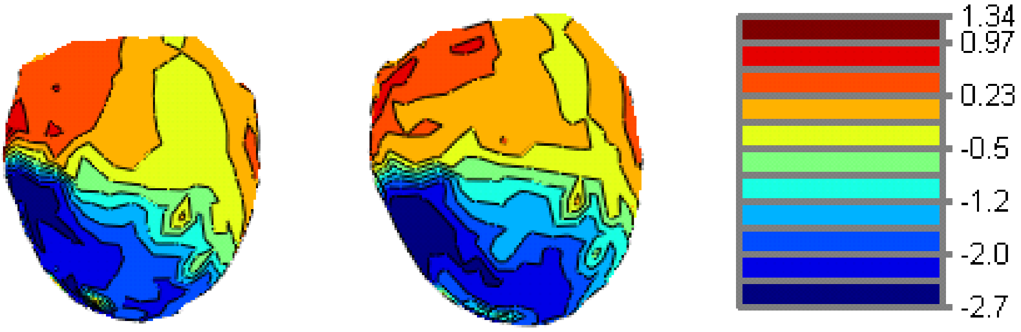

(g) Kalman-Real (h) Temp-Bayes (i) Colormap

Figure 4.11: Epicardial potential map for different STM solutions at 45 ms after the first stimulus.

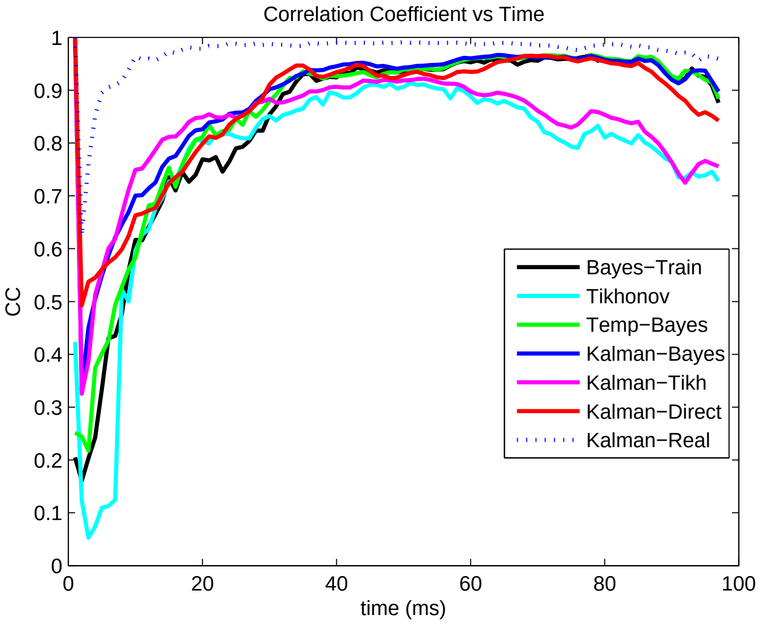

(a) The CC plot

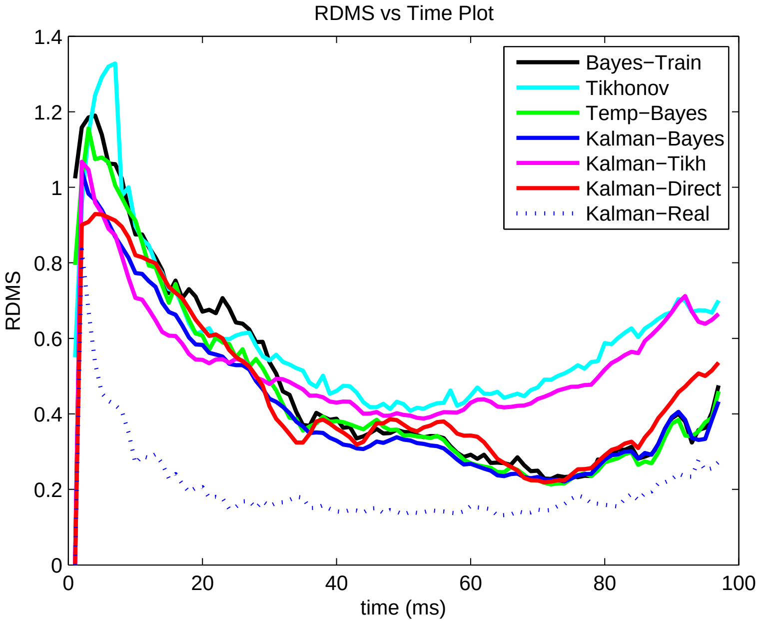

(b) The RDMS plot

Figure 4.12: The CC and RDMS values of different STM solutions with respect to time.

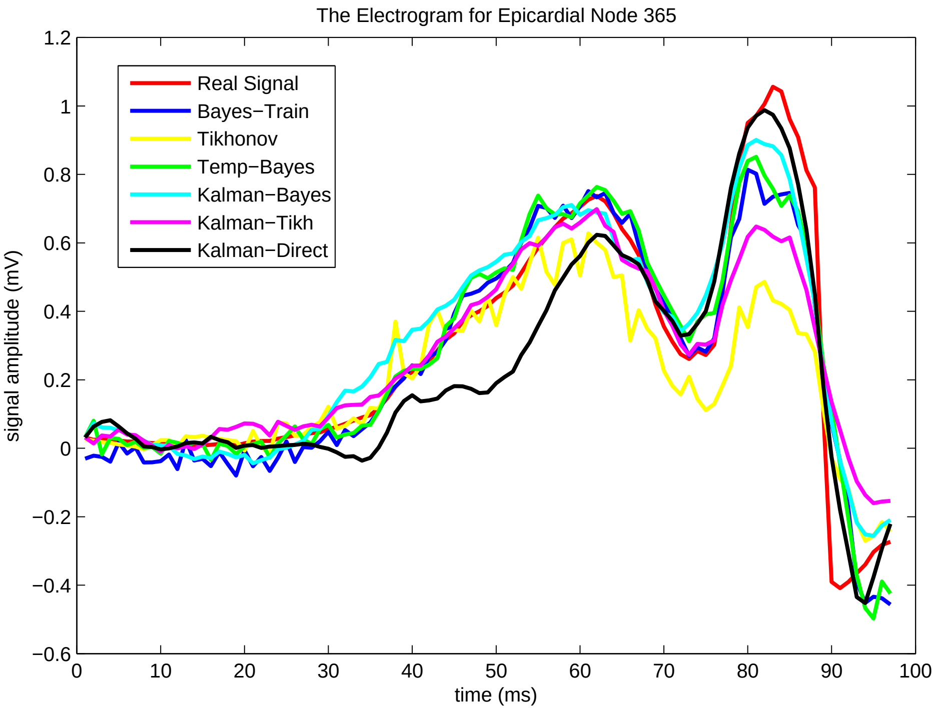

Figure 4.13: The real and estimated potential signal plot for the 365'th node on epicardium

problem of ECG with Kalman filter algorithm.

- This study is important in the sense that it shows the possible improvements with the usage of spatio-temporal algorithms instead of spatial ones. Especially the improvements obtained using Kalman-Bayes and Kalman-Tikh is important because all a priori information used in those two techniques are obtained from the spatial algorithm solutions.
- Kalman-Direct and Kalman-Bayes solutions performances are close to Kalman-Real solution.
- Although Kalman-Direct seems to follow the wavefront very good its much higher computational cost should also be considered. Also its dependence on the sequence of elements in the training set considerably limits its usage. Also the Kalman Direct performs worse than Kalman-Bayes, Kalman-Tikh and Kalman-Real.
- Kalman-Bayes performs slightly better than Temp-Bayes but its computational cost is higher. So if one can tolerate the extra computational time Kalman-Bayes could be preferred instead of Temp-Bayes or Bayes-Train.
- The results of Kalman-Tikh are worse than Bayes-Train and its computational time is higher but the advantage of Kalman-Tikh is that the necessity of using training set could be avoided with that approach.

4.5 The Effects of Geometric Error in Cardiac Electrical Imaging and A Statistical Model to Overcome Those Errors: Enhanced Noise Model

In this section first the affects of geometric errors in cardiac electrical imaging for the solutions obtained by Kalman Filter and Bayes-MAP will be studied. Then the improvements obtained by modeling those geometric errors in a statistical sense will be shown. According to this model geometric errors could be added to the inverse solutions algorithms as independent and identically distributed Gaussian noise. The new noise model is called the Enhanced noise model. The enhanced noise model is firstly proposed by Kaipio *et. al.* and then used in optical tomography [76, 77]. To the best of our knowledge this is the first application of this model to inverse ECG problem.

4.5.1 Effects of Geometric Errors

The effects of the geometric errors were investigated by several studies [28, 62]. In those studies the effects of geometric errors are shown to be more important (cause more error in the constructed inverse solution) than errors in the conductivity values within the thorax. For that reason the errors due to wrong conductivity assignments are not covered in this thesis.

The forward calculations are same as in 4.4. But the inverse calculations differ in order to simulate geometric errors. During the inverse calculations, position or the size of heart mesh is changed in the model and a new transfer matrix is calculated with this faulty mesh (F-mesh). Using this F-mesh in the inverse solution the geometric errors that could occur in noninvasive ECG imaging applications are simulated. Two kinds of geometric errors are investigated in this study. These are the wrong determination of heart's position and size. These two problems could often occur due to the movement of the heart. First, the consequences of the faulty determination of heart's location are examined. The error is created by shifting the heart from its original position by 2 to 25 mm in the positive–x direction and using the transfer matrix calculated from these F-meshes in the inverse solution. Next, wrong estimation of heart's size is examined. The error is created by multiplying the heart's surface by a scalar varying from 0.90 to 1.10 to adjust its size. For example if the heart's surface is multiplied by 0.95, 5 percent reduction in the heart's size is achieved. These error margins are enough because the modern techniques used today for geometry determination usually have smaller errors than those. The training set used here is same as in 4.4. The simulation procedure for geometric errors is shown at Figure 4.14.

The inverse problem solution algorithms used here are:

1. **Tikhonov:** It is same as the one used at the previous section.
2. **Kalman-Real:** It uses the epicardial potential maps of the test data itself to calculate STM.

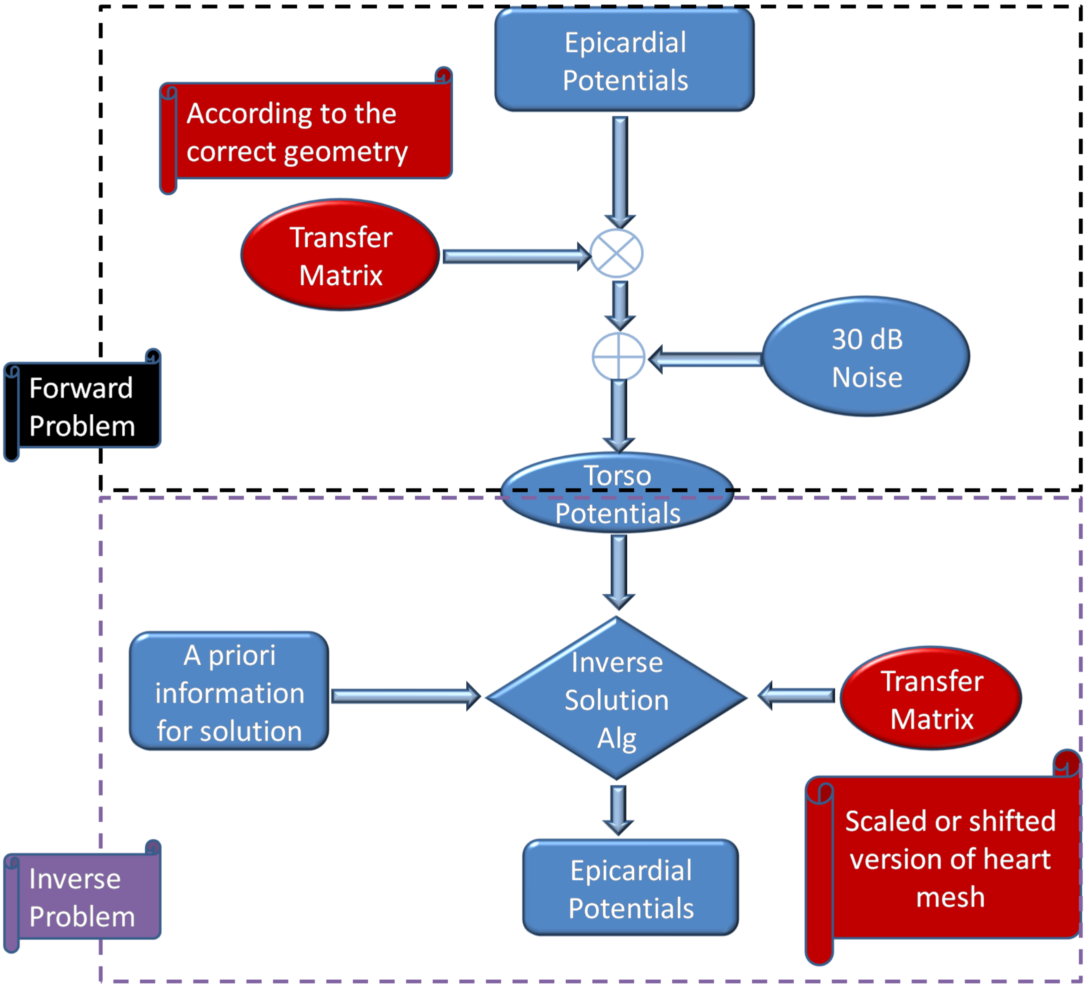

Figure 4.14: The schematic representation of the simulation procedure to study geometric errors.

3. **Bayes-Real:** It uses the epicardial potential maps of the test data itself to calculate the mean and the covariance matrix.
4. **Bayes-Train:** It uses the epicardial potential maps from a training set to calculate the mean and the covariance matrix (same as in 4.4).
5. **Kalman-Bayes:** It uses the solution of Bayes-Train to calculate STM (same as in 4.4).

In Table 4.4 the effects of wrong determination of heart's size on the inverse solutions can be seen. From that table it is seen that geometric errors based on size of the heart results in very significant degradations on the performances of the algorithms. This

Table 4.4: The CC and RDMS values for wrong determination of heart’s size.

	Tikhonov Regularization		Kalman-Real		Bayes-Real		Kalman-Bayes		Bayes-Train	
Scale	**CC**	**RDMS**	**CC**	**RDMS**	**CC**	**RDMS**	**CC**	**RDMS**	**CC**	**RDMS**
1.00	0.78	0.60	0.97	0.20	0.96	0.24	0.88	0.42	0.84	0.48
0.95	0.58	0.85	0.71	0.73	0.75	0.66	0.67	0.77	0.69	0.72
0.90	0.29	1.13	0.30	1.14	0.51	0.93	0.30	1.13	0.44	1.00
1.05	0.69	0.73	0.78	0.64	0.80	0.59	0.67	0.75	0.75	0.65
1.10	0.47	0.99	0.50	0.97	0.59	0.87	0.43	1.04	0.56	0.91

Table 4.5: The CC and RDMS values for the wrong determination of the heart’s location.

	Tikhonov Regularization		Kalman-Real		Bayes-Real		Kalman-Bayes		Bayes-Train	
Shift	**CC**	**RDMS**	**CC**	**RDMS**	**CC**	**RDMS**	**CC**	**RDMS**	**CC**	**RDMS**
0 mm	0.78	0.60	0.97	0.20	0.96	0.24	0.88	0.42	0.84	0.48
2 mm	0.77	0.62	0.96	0.26	0.95	0.28	0.88	0.43	0.84	0.49
6 mm	0.73	0.68	0.89	0.44	0.89	0.44	0.83	0.54	0.80	0.56
10 mm	0.66	0.78	0.77	0.64	0.80	0.60	0.74	0.69	0.74	0.68
15 mm	0.53	0.92	0.62	0.83	0.69	0.74	0.60	0.86	0.63	0.82
20 mm	0.38	1.07	0.49	0.96	0.60	0.84	0.47	1.00	0.53	0.93
25 mm	0.26	1.17	0.40	1.05	0.54	0.91	0.36	1.10	0.45	1.01

table also shows that Bayes-MAP algorithms are more immune to geometric errors than the Kalman Filter algorithms.

In Table 4.5, the performances of solutions when the heart’s location is wrongly determined are given. But when this type of geometric error is very small (eg. 2 mm shift), it does not change the performances much but after 6 mm shift the effects of geometric errors on the solutions become more obvious. Again the Bayes-MAP can be said to be affected less from geometric errors in comparison to Kalman-Filter.

From the results presented in this section it is clear that geometric errors has very significant effects on inverse solutions. Even 5 percent error in heart’s size decreases the CC by approximately 25 percent. For the heart location errors significant increases in errors is seen after the error exceeds 2 mm. The results presented here coincide with earlier studies and show the need for a possible technique to reduce the effects of geometric errors. This is a major obstacle on the way to practical usage of inverse ECG problem.

4.5.2 Enhanced Noise Model to Compensate Geometric Errors

In 4.5.1 it was shown that geometric errors reduce the quality of the inverse solutions significantly. In this section the simulation results of a possible approach to compensate the effects of geometric errors is given. This approach is called enhanced noise model and this is described in detail in 3.3. In Figures 4.15 and 4.16 the change in RDMS with different assumptions on the variance values of enhanced noise model are given. From those plots it could be seen that using enhanced noise model improves the performances of all algorithms used (Bayes-Train, Bayes-Real, Kalman-Bayes and Kalman-Real). From that figure:

- The improvements in Kalman filter approaches are higher than Bayes-MAP approaches
- The improvements for the algorithms that use very accurate *a priori* information (Bayes-Real, Kalman-Real) are higher.
- After a point the increase in the assumed measurement noise due to enhanced noise model increases error. So neither too low nor too high measurement noise covariance is good. This requires the determination of the global minimum of RDMS or maximum of the CC.
- The amount of assumed noise increases as the geometric error in the system is increased which proves the idea behind enhanced noise model.

In Table 4.6 the improvements in terms of CC and RDMS using enhanced noise model are given. The assumed measurement noise covariances are selected as the ones that give the best CC values. From those results the significant improvements can be seen clearly with the usage of enhanced noise model instead of normal noise model when geometric errors are present.

In Figures 4.17 and 4.18 the epicardial potential maps calculated for size and scale errors are given. Also the solutions that do and do not use enhanced noise model are given at those figures too. From those figures it could be seen that the enhanced noise model improves the solutions by a great amount. Also the solutions using enhanced noise model of Kalman filter methods (Kalman-Real, Kalman-Bayes) are better than

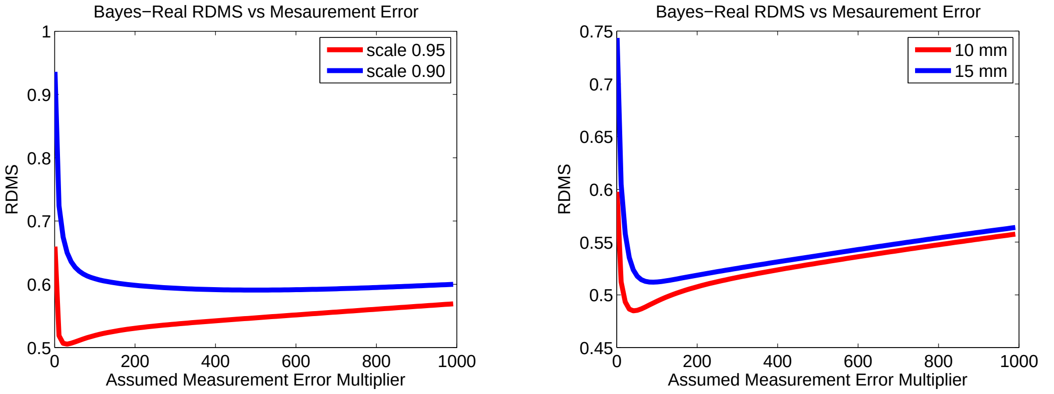

(a) Bayes-Real 0.95 and 0.90 scale (b) Bayes-Real 10 and 15 mm position

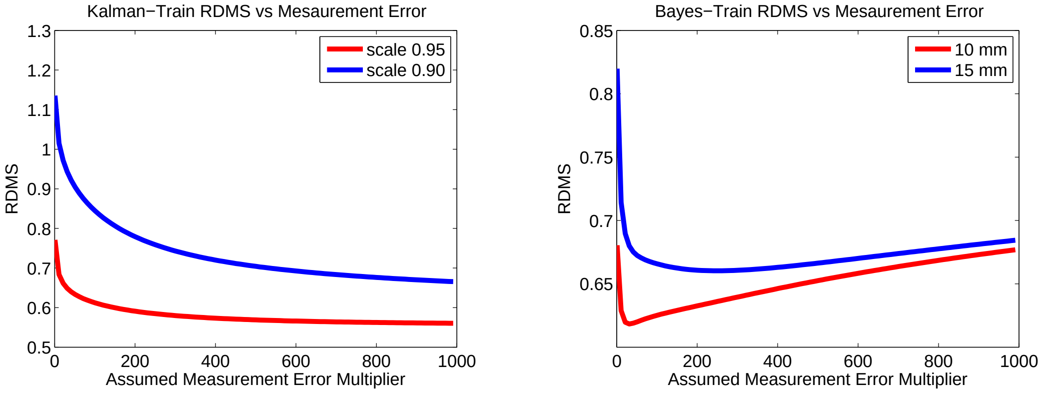

(c) Bayes-Train 0.95 and 0.90 scale (d) Bayes-Train 10 and 15 mm position

Figure 4.15: The change in RDMS values for different values of Enhanced noise model with geometric errors present for Bayesian-MAP.

Table 4.6: The CC and RDMS values when enhanced noise model is used. Imp. columns show the increase of CC in percentage compared to the solutions that do not use enhanced noise model.

	Kalman-Real			Bayes-Real			Kalman-Bayes			Bayes-Train		
Error Type	**CC**	**RDMS**	**Imp.**	**CC**	**RDMS**	**Imp.**	**CC**	**RDMS**	**Imp.**	**CC**	**RDMS**	**Imp.**
shift 10	0.92	0.37	19	0.86	0.49	16	0.81	0.58	9	0.77	0.62	4
shift 15	0.90	0.43	45	0.83	0.54	2	0.77	0.63	28	0.74	0.66	17
scale 0.95	0.94	0.34	25	0.85	0.50	16	0.81	0.57	21	0.76	0.63	10
scale 0.90	0.87	0.48	190	0.79	0.59	55	0.74	0.67	147	0.73	0,68	66

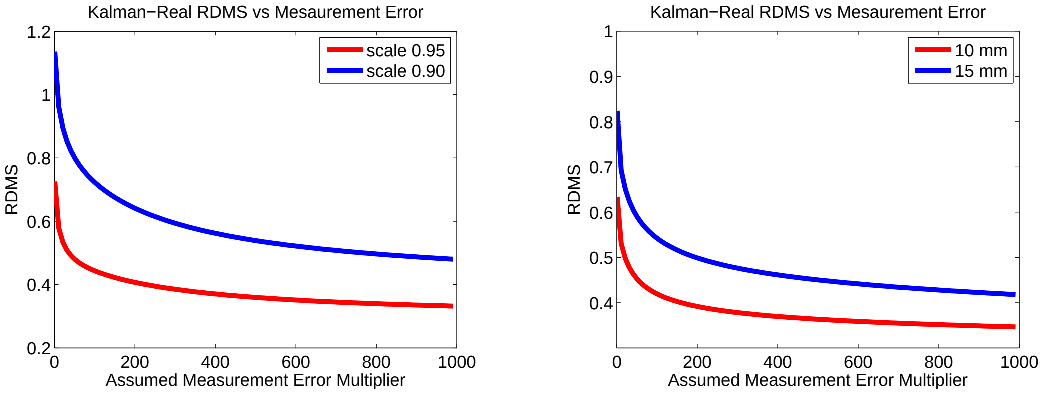

(a) Kalman-Real 0.95 and 0.90

(b) Kalman-Real 10 and 15 mm

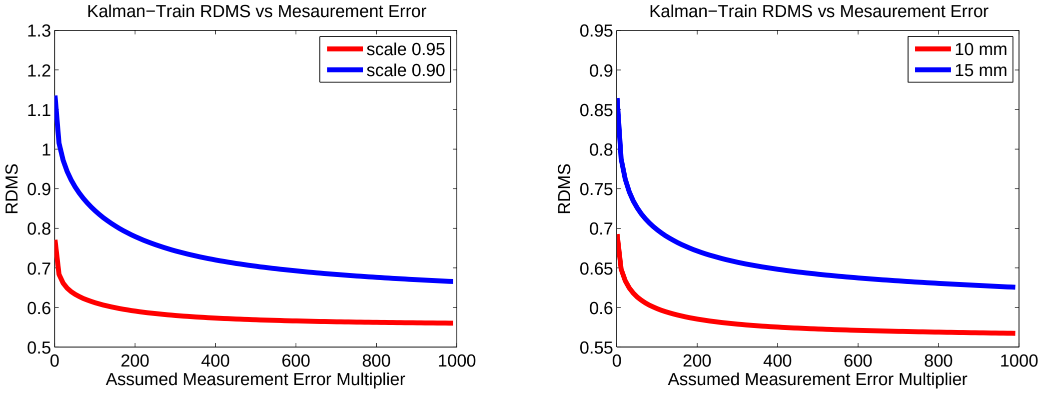

(c) Kalman-Bayes 0.95 and 0.90 scale

(d) Kalman-Bayes 10 and 15 mm position

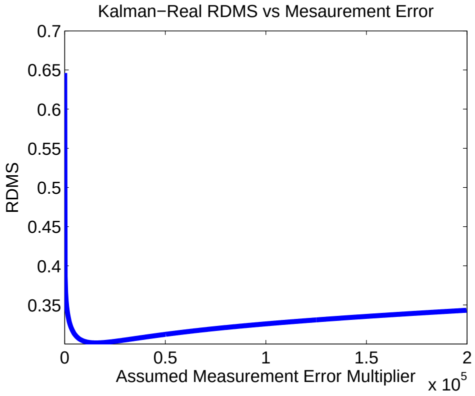

(e) Kalman-Real 10 mm

Figure 4.16: The change in RDMS values for different values of Enhanced noise model with geometric errors present for Kalman filter.

(a) Real Distribution (b) Colormap

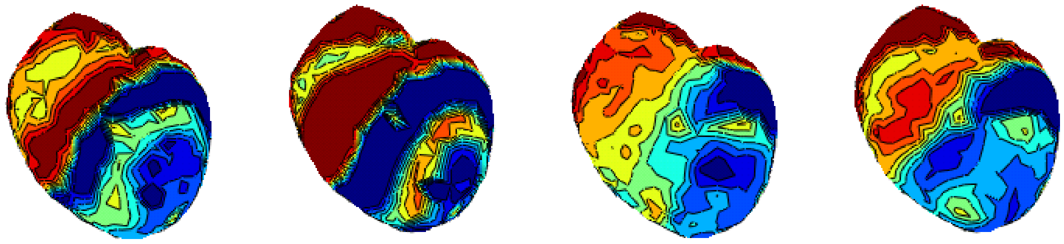

(c) Kalman-Real (d) Bayes-Real (e) Kalman-Bayes (f) Bayes-Train

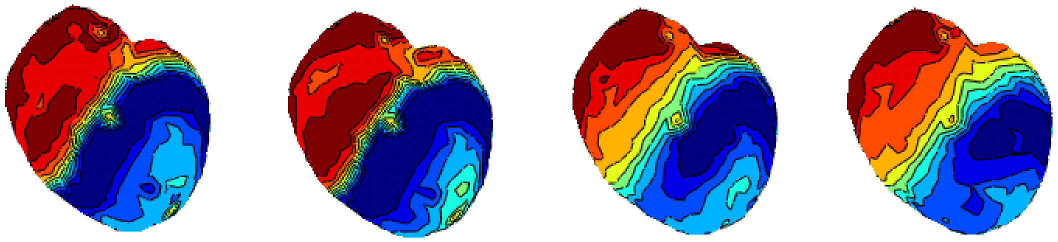

(g) ENMKalman-Real (h) ENMBayes-Real (i) ENMKalman-Bayes (j) ENMBayes-Train

Figure 4.17: The comparison of epicardial potential maps for scale 0.95 that do and do not use enhanced noise model. The ENM at the beginning of the model name means the measurement noise covariance used is selected according to the enhanced noise model.

Bayes-MAP methods (Bayes-Real, Bayes-Train). The enhanced noise model could be said to have smoothing affect on the wavefront especially for the Bayes-MAP based methods which is obviously due to the increased measurement error assumption.

In this section it is shown that determining the measurement noise covariances according to the enhanced noise model (adding the geometric errors to measurement noise as independent and identically distributed Gaussian noise) greatly improves the results. But the problem here is the determination of the amount of error that should be inserted to the model to compensate geometric errors. As it is seen from Figure 4.15 there is a point where the errors are minimized and after that point the errors

(a) Real Distribution (b) Colormap

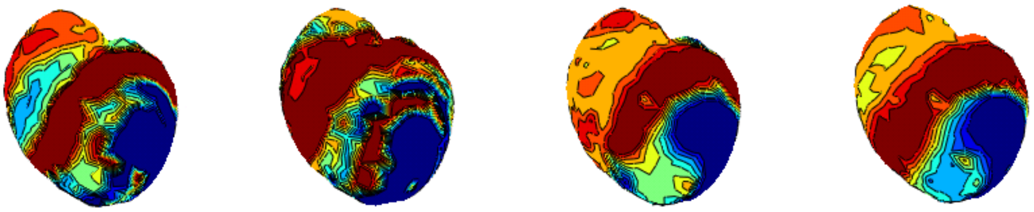

(c) Kalman-Real (d) Bayes-Real (e) Kalman-Bayes (f) Bayes-Train

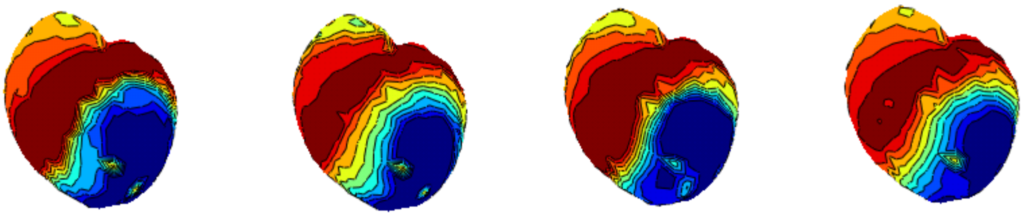

(g) ENMKalman-Real (h) ENMBayes-Real (i) ENMKalman-Bayes (j) ENMBayes-Train

Figure 4.18: The comparison of epicardial potential maps for 15 mm shift that do and do not use enhanced noise model. The ENM at the beginning of the model name means the measurement noise covariance used is selected according to the enhanced noise model.

starts to increase again. Another important observation is the error decline at the Kalman filter algorithms are a lot more comparison to Bayes-MAP algorithms when enhanced noise model is used.

4.6 Determination of the Measurement and Process Noise Covariance Matrices Using Residuals

In this section the measurement and process noise covariance matrices are estimated using a method based on residuals. In order to test the performance of the methods different scenarios are employed. In the first scenario both measurement and process noise covariance matrices are calculated for the case that no geometric error exists and only independent and identically distributed (iid) 15 or 30 dB noise is present. By doing so the algorithm's ability to compensate additive errors is tested. In the second scenario again both process and measurement noise covariance matrices are calculated but this time along with 30dB iid noise also geometric errors are present at the system. This scenario is implemented to find out if residual based algorithm is able to compensate the geometric errors. In the third and fourth scenarios only measurement noise covariance matrix is calculated and the value that gives highest CC value for 30 dB noise case is used as process noise covariance. The difference between third and fourth scenarios is that the third scenario is simulated for 15 and 30 dB iid noise cases and the fourth scenario is tested for the case when both geometric errors and 30 dB noise are present. As stated in 4.5.2 the determination of correct values for the process noise covariance without using CC and RDMS is the most important problem that needs to be solved before the usage of ENM in practical cases. The fourth scenario at this section refers to that problem and tries to determine the measurement noise covariance matrix that should be used in the system to compensate geometric errors by using body surface potentials

At the first scenario the process and measurement noise covariances are estimated for the cases where 30 dB or 15 dB independent and identically distributed Gaussian noise is added to the system. The results for this scenario are given in Table 4.7. From that table:

Table 4.7: CC and RDMS values for Kalman-Real and Kalman-Bayes when noise covariances are calculated from residuals. The Res prefix before method name indicates the noise covariances that are calculated from residuals are used in solutions. No prefix means that those solutions are obtained with noise covariances used for 30 dB.

Noise	Kalman-Real		Kalman-Bayes		Res-Kalman-Real		Res-Kalman-Bayes	
	CC	**RDMS**	**CC**	**RDMS**	**CC**	**RDMS**	**CC**	**RDMS**
30 dB	0.97	0.20	0.88	0.42	0.95	0.26	0.88	0.43
15 dB	0.84	0.49	0.79	0.56	0.36	1.11	0.42	1.04

Table 4.8: CC and RDMS values for Kalman-Real and Kalman-Bayes when noise covariances are calculated from residuals with geometric errors are present(15mm shift in heart's position and 0.95 change in heart's size). The Res prefix before method name indicates the noise covariances that are calculated from residuals are used in solutions. No prefix means that those solutions are obtained with noise covariances used for 30 dB.

Geometric Error	Kalman-Real		Kalman-Bayes		Res-Kalman-Real		Res-Kalman-Bayes	
	CC	**RDMS**	**CC**	**RDMS**	**CC**	**RDMS**	**CC**	**RDMS**
15 mm Shift	0.62	0.83	0.60	0.86	0.56	0.90	0.57	0.89
0.95 scale	0.71	0.73	0.67	0.77	0.61	084	0.62	0.83

- When 30 dB noise is added to the system the algorithm successfully determine noise covariances very close to optimal values.
- When the noise is increased to 15 dB the algorithm fails and the results obtained are even worse than the solutions that uses the noise covariances for 30 dB case.

At the second scenario the performance of the algorithm when geometric errors are present is tested. For that purpose 15 mm shift in heart's location and 0.95 scale error in heart's size are simulated as geometric errors. Then process and measurement noise covariance matrices are calculated. Finally, epicardial potential map solution is obtained using those noise covariances in Kalman-Real and Kalman-Bayes algorithms. Table 4.8 shows that using the residual based method not only provides us no improvements but also worsen the results in the case of geometric errors. This result was not expected. The possible reason for this result is the search for many unknowns (both process and measurement noise covariance matrices) with limited and indirect information (body surface potentials).

In the next scenario the process noise covariance is fixed to the value that gives highest

Table 4.9: CC and RDMS values for Kalman-Real and Kalman-Bayes when only measurement noise covariances is calculated from residuals. The Res prefix before method name indicates the noise covariance that is calculated from residuals are used in solutions. No prefix means that those solutions are obtained with noise covariances used for 30 dB. The **R** shows the scalar σ calculated for measurement covariance matrix which is in the form $\sigma\mathbf{I}$.

Noise	Kalman-Real		Kalman-Bayes		Res-Kalman-Real			Res-Kalman-Bayes		
	CC	**RDMS**	**CC**	**RDMS**	**CC**	**RDMS**	**R**	**CC**	**RDMS**	**R**
30 dB	0.97	0.20	0.88	0.42	0.97	0.23	0.0103	0.85	0.49	0.0159
15 dB	0.84	0.49	0.79	0.56	0.97	0.24	0.0177	0.85	0.49	0.0189

CC for 30 dB noise and the measurement noise covariance is calculated with the algorithm in order to make analogy with the enhanced noise model.

In Table 4.9 the scenario that calculates only measurement error covariance is tested when there is no geometric error and only 30 or 15 dB Gaussian noise is present.

From Table 4.9 it is seen that the solutions obtained with residual algorithm are slightly worse than the optimal CC and RDMS values especially for the Kalman-Bayes algorithm when results for 30 dB are examined. But when the SNR is decreased to 15 dB the measurement covariance matrix calculated from the residuals improves the results significantly. Also it is seen that the measurement error covariance calculated for Kalman-Real is smaller than Kalman-Bayes which is because the STM used in Kalman-Real is more accurate than the Kalman-Bayes. This result is important in the sense that the quality of the STM can be evaluated from those values and the appropriate one from available STM's can be chosen. But this is a preliminary result and more study on this is required.

In Table 4.10 the scenario that calculates only measurement error covariance is tested when geometric errors along with 30 dB Gaussian noise is present.

From Table 4.10 it is clear that instead of calculating both process and measurement noise covariances, fixing the process noise covariance and calculating only measurement noise covariances results in higher CC and lower RDMS. The solutions are improved significantly with residual based algorithm when geometric errors are present. It is also seen that the scalar (σ) that determines the measurement error covariance matrix ($\sigma\mathbf{I}$) is calculated as same for both 0.95 scale and 15 mm shift errors. It is seen

Table 4.10: CC and RDMS values for Kalman-Real and Kalman-Bayes when only measurement noise covariance is calculated from residuals with geometric errors are present(15mm shift in heart's position and 0.95 change in heart's size). The Res prefix before method name indicates the noise covariance that is calculated from residuals are used in solutions. No prefix means that those solutions are obtained with noise covariances used for 30 dB.The **R** shows the scalar (σ) calculated for measurement covariance matrix which is in the form ($\sigma\mathbf{I}$).

Geometric Error	Kalman-Real		Kalman-Bayes		Res-Kalman-Real			Res-Kalman-Bayes		
	CC	**RDMS**	**CC**	**RDMS**	**CC**	**RDMS**	**R**	**CC**	**RDMS**	**R**
15 mm Shift	0.62	0.83	0.60	0.86	0.87	0.47	0.0103	0.77	0.64	0.0162
0.95 scale	0.71	0.73	0.67	0.77	0.92	0.38	0.0103	0.81	0.57	0.0162

that the calculated measurement covariance matrix does not change much for different amounts of geometric errors. For example for Kalman-Bayes it is 0.0159 for no geometric error case, 0.0160 for 6 mm shift, 0.0162 for 15 mm shift and 0.0164 for 25 mm shift. From these it is clear that the calculated measurement noise covariance increases as the amount of geometric error increases which supports the ENM.

At Figure 4.19 the epicardial maps with and without residual based method are shown for 15 mm location error. From those maps it is clear that the epicardial potential distributions are constructed with higher correlation to the real distribution when the measurement noise covariance matrix is calculated with the residual based algorithm.

Overall when both process and measurement error covariance matrices are calculated, the residual based algorithm can only determine near to optimal noise covariances for small errors like 30 dB. When the error increases to 15 dB Gaussian noise or geometric errors are included to the system the solutions obtained are even worse than the case when error covariances of 30 dB noise is used. If the long processing time (approximately 80 minutes to calculate the noise covariances) is also considered we don't think this method is appropriate when both process and measurement noise covariance matrices are desired to be calculated.

But if the process error covariance matrix is fixed and only measurement error covariance is calculated, significant improvements are observed when geometric errors are present or the SNR ratio is small (15dB). For the cases without geometric errors and high SNR (30 dB) the solutions are again close to optimal but slightly worse

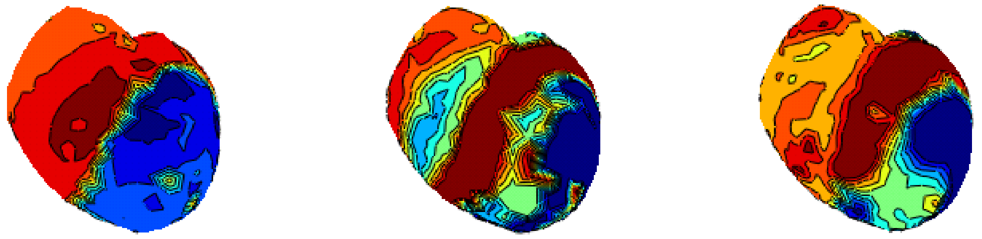

(a) Real Distribution (b) Kalman-Real (c) Kalman-Bayes

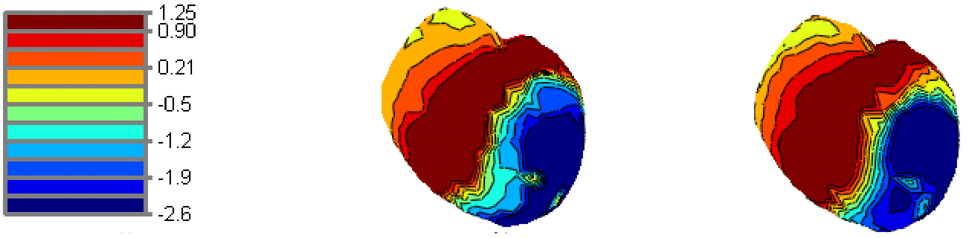

(d) Colormap (e) Res-Kalman-Real (f) Res-Kalman-Bayes

Figure 4.19: Epicardial potential maps for 54 ms after the first stimulus. The map solutions of both Kalman-Real and Kalman-Bayes are given when 15 mm shift geometric error is present. The Res prefix before the name of the method stands for the measurement noise covariance is calculated with the residual based algorithm. When there is no prefix it means that the same noise covariance matrices as the case in 30 dB Gaussian noise are used.

especially for Kalman-Bayes algorithm. We think the significant improvements in geometric error cases are more important than the slight decreases in error performance for the cases without geometric errors and this algorithm can be used for inverse ECG problem. But here again a major disadvantage should be noted which is the long processing time which is approximately 60 minutes. Another promising result is that the measurement noise covariance calculated for Kalman-Bayes is higher than the Kalman-Real. The reason for this increase is due to the quality of the STM used in algorithms. This result should be further studied and it could be used as an indicator of the quality of the STM used in Kalman filter.

4.7 Expectation Maximization Algorithm to Determine Measurement and Process Noise Covariance Matrices

As described before the values of measurement and process noise covariances are also critical in order to obtain good solutions. At this section expectation maximization algorithm is used to determine those covariances.

The first scenario used is for the case of additive white Gaussian noise. For that purpose body surface potentials are simulated from the epicardial potentials, at 15 or 30 dB SNR. Then from those BSP's the epicardial potentials are estimated using Kalman-Real and Kalman-Bayes approaches. The initial error covariances needed for EM algorithm are chosen randomly as $0.01x\mathbf{I}_N$ for process and $0.16x\mathbf{I}_M$ for measurement noise where $\mathbf{I}_N$ is the NxN and $\mathbf{I}_M$ is the MxM identity matrices. Here N is the number of epicardial nodes and M is the number of BSP measurement electrodes. In Figure 4.20 the RDMS versus iteration number plots are shown. From those plots it is seen that the EM algorithm is able to determine the correct values for noise covariances for both 15dB and 30 dB Gaussian noise cases. Also the algorithm achieves to find the covariances not only for Kalman-Real case both also for Kalman-Bayes which is important because the usage of Kalman-Real is not possible for practical cases. Another important fact is no significant improvement is observed in terms of RDMS values after the first five iterations which means that epicardial potential estimations could be obtained just after five iterations. Because each iteration takes about 65 seconds it is wise to avoid unnecessary iterations.

In the second scenario only the measurement error covariance matrix is calculated to compensate the effects of geometric errors. For that purpose the process noise covariance is fixed and only the measurement noise covariance is updated with EM. The initial process and measurement noise covariance matrices are the ones that give the best CC values when no geometric error is present. Only the measurement noise covariance is updated at this scenario to make an analogy with the enhanced noise model described before where the geometric errors are compensated with the increase in the measurement error covariance. In Figure 4.21 RDMS versus iteration plots for the geometric errors 15 mm shift and 0.95 scale are given for the Kalman-Real and Kalman Bayes algorithms. The inferences from those plots are:

- Very significant improvements are obtained in terms of error metrics.
- The convergence is completed usually at five iterations.
- The global minimum point sought for ENM is found with EM algorithm from

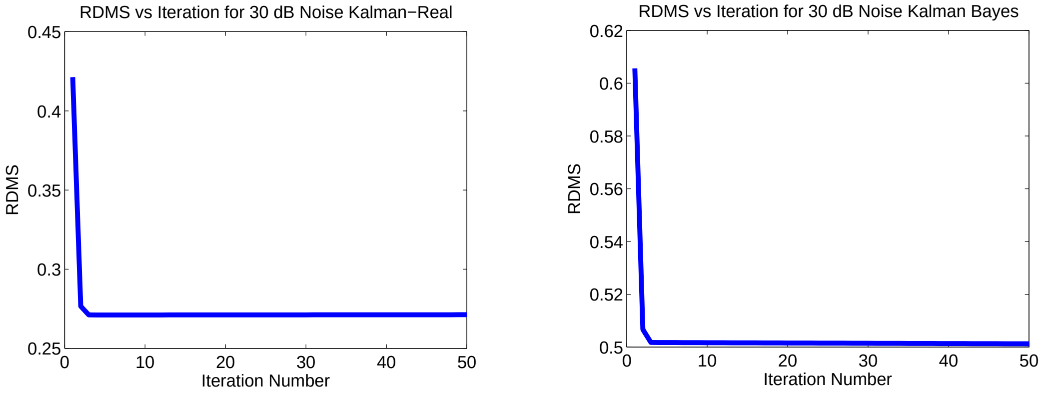

(a) 30 dB Gaussian Noise for Kalman-Real (b) 30 dB Gaussian Noise for Kalman-Bayes

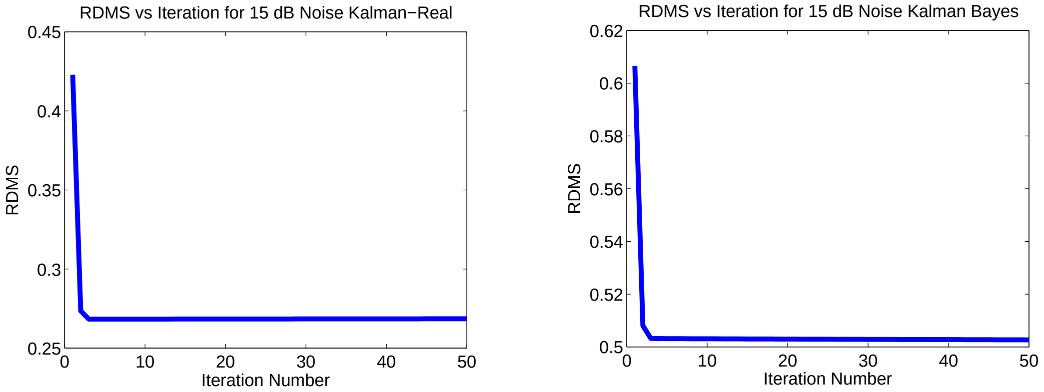

(c) 15 dB Gaussian Noise for Kalman-Real (d) 15 dB Gaussian Noise for Kalman-Bayes

Figure 4.20: The evolution of RDMS values with respect to iterations of the EM algorithm for Kalman-Real and Kalman-Bayes techniques for 15 and 30 dB Gaussian noise.

the body surface potentials and this is a very important result to compensate geometric errors.

In the last scenario both the measurement and process noise covariances are updated with EM algorithm for the case where the geometric errors are present. As in the second scenario the initial process and measurement noise covariance matrices are selected as the ones that give the best CC values when no geometric error is present and the geometric errors simulated are the 15 mm shift and 0.95 scale. This time as seen from Figure 4.22 again improvements are obtained but unlike the first and second scenarios the RDMS values decrease slowly which requires more iterations. Another observation from those plots is that the improvements in the Kalman-Real algorithm is higher than those in Kalman-Bayes algorithm, which is due to the quality of the *a priori* information. This result was also observed with the ENM.

The epicardial potential maps for the cases explained in scenario one are given in Figures 4.23. For the second and third scenarios the results are shown in Figure 4.24 and 4.25. The epicardial potentials maps also support our earlier inferences and improvements using EM algorithm are obvious.

In this section the EM algorithm is used to calculate the process and measurement noise covariances. The overall results obtained with EM studies are:

- For 15 and 30 dB Gaussian noise cases only five iterations with the EM algorithm is enough to calculate the optimal noise covariances.
- For the case of geometric errors when only measurement noise covariance is updated with EM, the results are improved significantly with EM algorithm. This result also supports the assumption made at the enhanced noise model.
- For the case of geometric errors when both measurement and process noise covariances are updated by EM, the improvements are smaller than those obtained when only the measurement noise covariance matrix is updated by EM. Also the convergence rate is much slower than first and second scenarios (it still converges after 500 iterations). The possible reason for smaller convergence

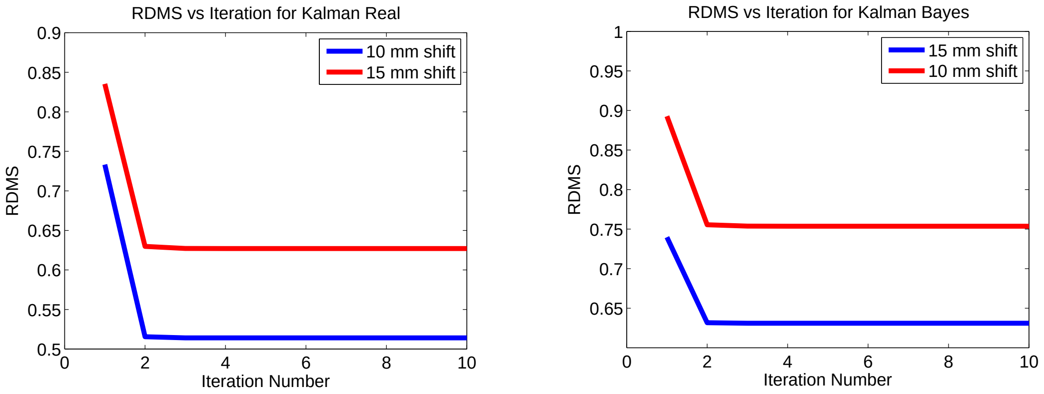

(a) 10 and 15 mm Shift for Kalman-Real (b) 10 and 15 mm Shift for Kalman-Bayes

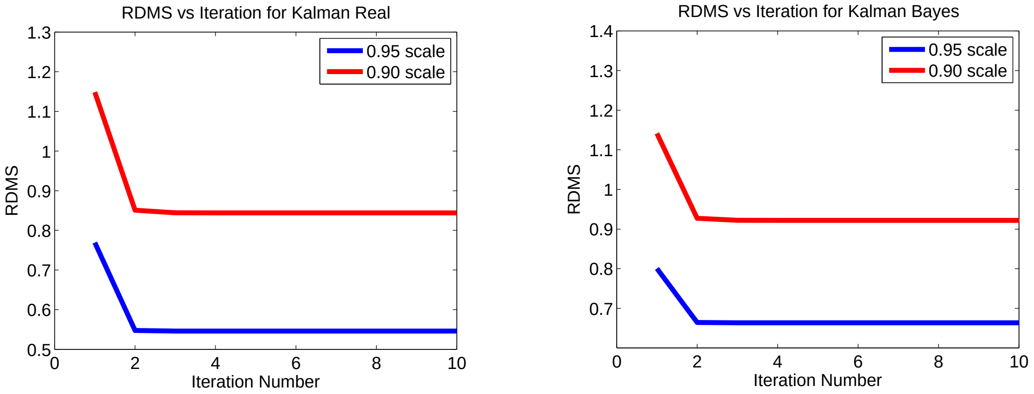

(c) Scale 0.90 and 0.95 for Kalman-Real (d) Scale 0.90 and 0.95 for Kalman-Bayes

Figure 4.21: The evolution of RDMS values with respect to iterations of the EM algorithm which updates only measurement noise covariance for Kalman-Real and Kalman-Bayes techniques for 10 and 15 mm shift and 0.90 and 0.95 scale geometric errors.

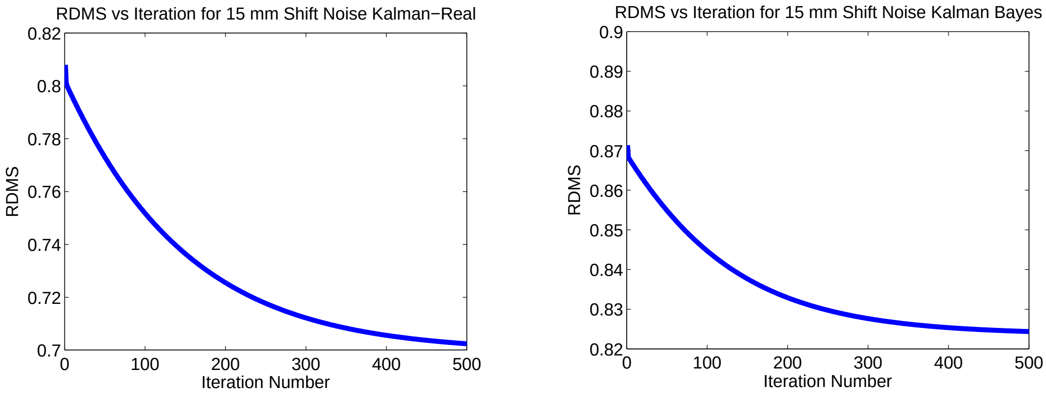

(a) 15 mm Shift for Kalman-Real (b) 15 mm Shift for Kalman-Bayes

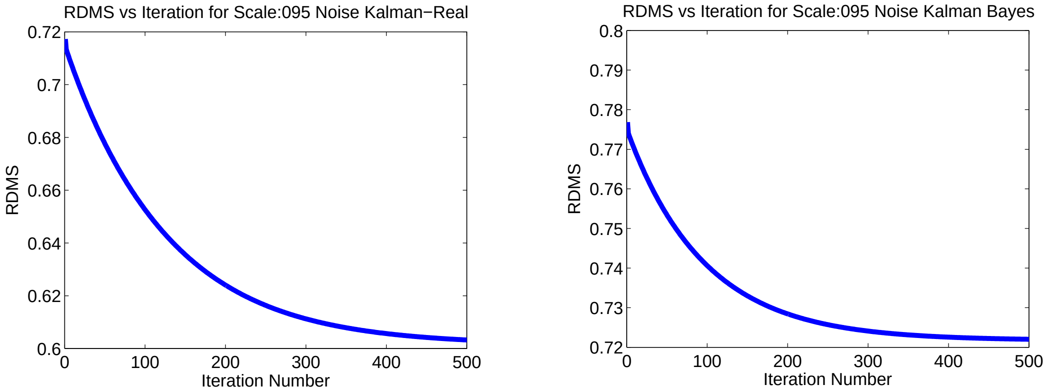

(c) Scale 0.95 for Kalman-Real (d) Scale 0.95 for Kalman-Bayes

Figure 4.22: The evolution of RDMS values with respect to iterations of the EM algorithm for Kalman-Real and Kalman-Bayes techniques for 15 mm shift and 0.95 scale geometric errors.

is because determining the optimal values for both measurement and process noise covariances is a lot more complex than determining only the measurement noise covariance.

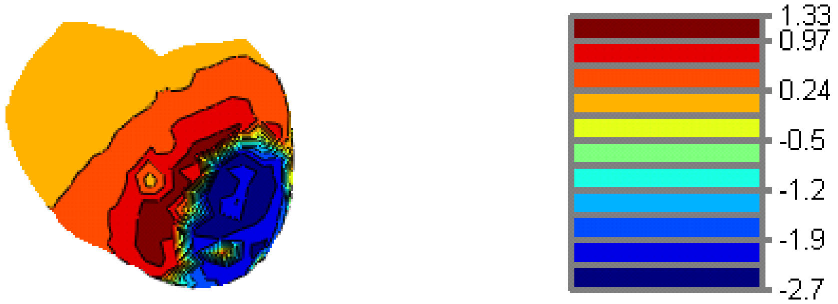

(a) Real Distribution (b) Colormap

(c) Kalman-Bayes (d) EM-Kalman-Bayes

(e) Kalman-Real (f) EM-Kalman-Real

Figure 4.23: Epicardial potential maps for 39 ms after the first stimulus. The map solutions of both Kalman-Real and Kalman-Bayes are given when 15 dB Gaussian noise is added to the system. The EM prefix before the name of the method stand for the noise covariances are calculated with EM algorithm and other solutions use the same noise covariance matrices as the case in 30 dB Gaussian noise.

(a) Real Distribution (b) Colormap

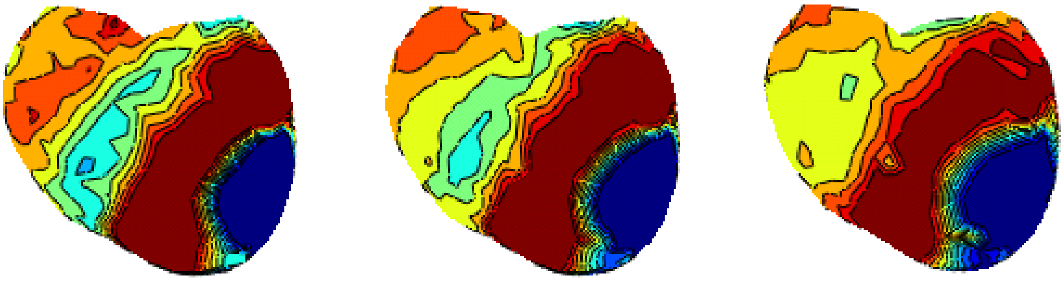

(c) Kalman-Bayes (d) EM-Kalman-Bayes (e) EM-Kalman-Bayes only R

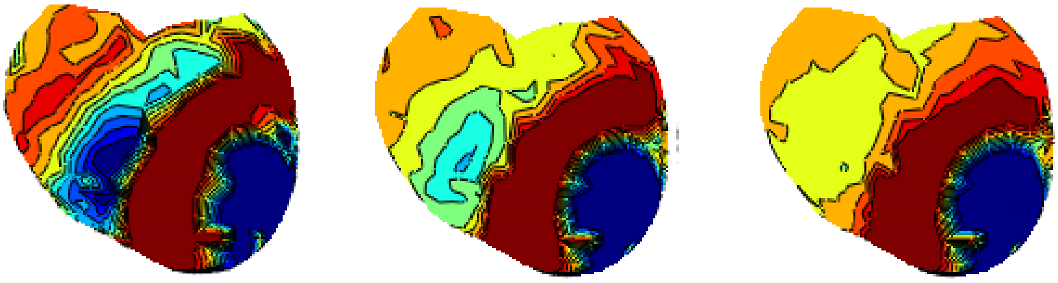

(f) Kalman-Real (g) EM-Kalman-Real (h) EM-Kalman-Real only R

Figure 4.24: Epicardial potential maps for 39 ms after the first stimulus. The map solutions of both Kalman-Real and Kalman-Bayes are given when 15 mm shift geometric error is present. The EM prefix before the name of the method stands for both measurement and process noise covariances are calculated with EM algorithm. ’only R’ means only the measurement error is updated and when there is no prefix it means that the same noise covariance matrices as the case in 30 dB Gaussian noise are used.

(a) Real Distribution (b) Colormap

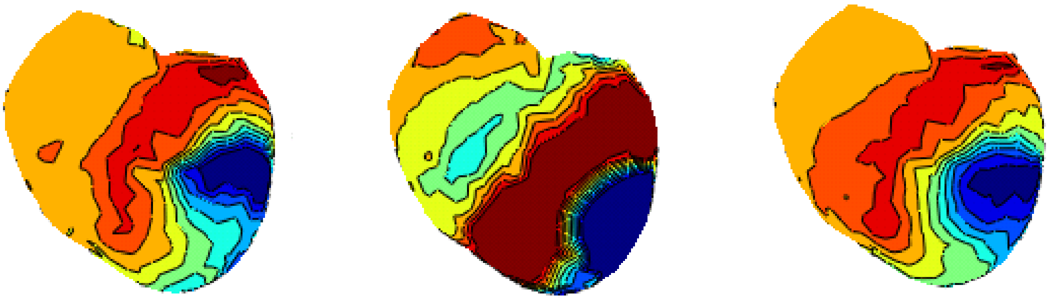

(c) Kalman-Bayes (d) EM-Kalman-Bayes (e) EM-Kalman-Bayes only R

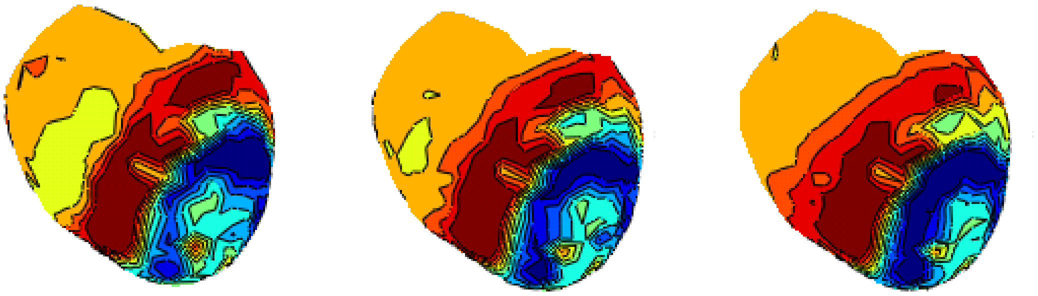

(f) Kalman-Real (g) EM-Kalman-Real (h) EM-Kalman-Real only R

Figure 4.25: Epicardial potential maps for 39 ms after the first stimulus. The map solutions of both Kalman-Real and Kalman-Bayes are given when 0.95 scale geometric error is present. The EM prefix before the name of the method stands for both measurement and process noise covariances are calculated with EM algorithm. ’only R’ means only the measurement error is updated and when there is no prefix it means that the same noise covariance matrices as the case in 30 dB Gaussian noise are used.

CHAPTER 5

CONCLUSIONS

This thesis focuses on three major problems. The first one is the solution of inverse problem of ECG using spatio-temporal methods especially with Kalman filter. The second study is on the effects of geometric errors and a noise model to include geometric noise to the general formulation. The last study focuses on the determination of process and measurement noise covariances using body surface potentials with and without geometric errors. The inverse solution scenarios used in those three studies are

1. **Tikhonov:** The zero'th order Tikhonov regularization solution in which a different regularization parameter was calculated using the L-Curve approach for each time instant.
2. **Kalman-Tikh:** The solution of the zero'th order Tikhonov regularization was used to calculate the STM.
3. **Bayes-Real:** The epicardial potential maps of the test data itself are used to calculate the mean and the covariance matrix in the spatial Bayesian MAP estimation.
4. **Kalman-Real:** The epicardial potential maps of the test data itself were used to calculate the STM.
5. **Bayes-Train:** The epicardial potential maps from a training set were used to calculate the mean and the covariance matrix in the spatial Bayesian MAP estimation.

6. **Temp-Bayes:** The spatio-temporal Bayesian MAP solution with *a priori* information from the training set.

7. **Kalman-Bayes:** A training set was used to obtain the solution using the spatial Bayesian MAP (Bayes-Train) and then this solution was used to calculate the STM.

8. **Kalman-Direct:** A training set was used to calculate the STM directly.

5.1 Spatio-temporal Methods for Inverse Problem of ECG

In this work, Tikhonov, Kalman-Tikh, Bayes-Train, Kalman-Bayes, Temp-Bayes and Kalman-Direct approaches were compared. But before the comparisons could be made, one of the major difficulties for the solution of inverse problem of ECG using the Kalman filter approach had to be solved. This difficulty was the determination of the state transition matrix (STM) which models the temporal evolution of the epicardial potentials for the state-space model. Kalman-Tikh, Kalman-Bayes and Kalman-Direct are possible solutions to this difficulty.

Also in order to decrease the computational cost while the STM is calculated from epicardial potentials, one node was assumed to be related only a few nodes at the previous time instant, rather than all nodes so STM matrix was constructed as a sparse matrix. It was shown that this simplification has no significant effects on the solution provided that the related nodes are selected carefully. We also showed that the best choice is to take advantage of both the locality property (1’st order neighbors) and the shape of the activation wavefront (the nodes that are activated at the same time).

From the solutions the following inferences were made:

- Kalman-Tikh and Kalman-Bayes algorithms could be used to solve the inverse ECG problem with Kalman filter without the need for the true epicardial potential distribution.

- Improvements are obtained by using spatio-temporal methods instead of only spatial methods.

- The quality of Kalman-Direct solution is highly dependent on the sequence of the elements in the training set and its computational cost is very high, especially when the number of epicardial potential recordings included in the training set increases.
- Kalman-Bayes performs slightly better than Temp-Bayes but its computational cost is higher. So if one can tolerate the extra computational time, Kalman-Bayes could be preferred instead of Temp-Bayes or spatial Bayes.
- The results of Kalman-Tikh are worse than Bayes-Train and its computational time is higher but the advantage of Kalman-Tikh is that the necessity of using a training set could be avoided with that approach.

5.2 The Effects of Geometrics Errors to the Solution of Inverse ECG Problem

Two different kinds of geometric errors were studied in this work; wrong determination of the heart's size and location. The effects of geometric errors were studied for five inverse problem algorithms which are Tikhonov, Kalman-Real, Bayes-Real, Bayes-Train and Kalman-Bayes.

The inferences were:

- The geometric errors significantly reduce the performances of the inverse problem algorithms.
- The Bayesian MAP estimation methods are more immune to geometric errors in comparison to Kalman filter methods.

To overcome the performance decrease that occurs due to the geometric errors, these errors were modeled as additive Gaussian noise in the inverse ECG problem definition. This approach was called the enhanced noise model (ENM). In the ENM, the overall noise covariance matrix was obtained by adding the measurement noise and geometric noise covariance matrices. The conclusions are:

- ENM achieved very significant improvements in the solutions of Kalman-Real, Kalman-Bayes, Bayes-Train and Bayes-Real methods when geometric errors are present.

- The amount of increment at the measurement covariance matrix is critical because there is a global minimum point where the ENM performs best and then the errors started to increase.
- Kalman-Real and Bayes-Real showed more improvements than Kalman-Train and Bayes-Train due to the high quality of the *a priori* information used in those algorithms .

5.3 Estimation of the Measurement and Process Noise Covariance Matrices from Body Surface Potentials

The estimation of the correct noise covariances is critical for both Bayesian MAP and Kalman filter methods. As a part of this thesis, two different approaches to determine noise covariances were modified to be used for inverse ECG problem. The performances of those methods were tested for the Kalman-Bayes and Kalman-Real algorithms. Also both of these approaches were tested for two different cases.

Case 1 Both process and measurement covariance matrices were calculated.

Case 2 The process noise covariance matrix was fixed to a value that is calculated previously for the simulation study at 30 dB SNR when there are no geometric errors, and only measurement noise covariance was calculated.

The first method is based on residuals. The conclusions for **Case 1** are:

- Algorithm determined the near optimal noise covariances for high SNR ratios (30 dB).
- It failed when the SNR is low (15dB) or geometric errors are present.
- The computation time was high (80 minutes).

For the **Case 2**:

- The algorithm calculated near optimal values not only for high SNR (30dB) but also for lower SNRs (15dB). Significant improvements were obtained for the low SNR case when the covariance calculated with the residual algorithm was used instead of fixed measurement noise covariance.
- When geometric errors were present, the calculated measurement covariance matrix resulted in major improvements in the solutions.
- Computation time was lower than the previous case (60 minutes).

The second method is based on expectation maximization (EM) and it is tested to determine the noise covariance matrices with and without geometric errors. The results showed that:

- The EM algorithm could calculate the optimal process and measurement noise covariances for both 15dB and 30 dB SNR cases when there are no geometric errors. Also the convergence rate was very high and near optimal results were obtained just after five iterations (both for Case 1 and Case 2).
- When only the measurement noise covariance was updated with EM (Case 2) to make an analogy with the assumption made in the ENM, the convergence rate of the algorithm was again very fast, usually five iterations were enough to converge. The improvements were very significant and coincide with the results of the ENM.
- The EM algorithm (Case 1) also achieved to enhance the solutions when both process and measurement noise covariances were updated, when the geometric errors along with 30 dB Gaussian noise were present. But this time the iteration number should be higher (although the improvements obtained per iteration decreases as the iteration number increases the algorithm still showed improvements after 500 iterations). The improvements obtained there were smaller than when only measurement noise covariance was updated. A possible reason for this is, so many parameters were tried to be determined with little information.
- The improvements obtained with EM algorithm were higher for the Kalman-Real comparison to the Kalman-Bayes. That result coincides with the results

obtained with ENM and it was probably due to the high quality of the *a priori* information used in Kalman-Real.

- Overall it was determined that using EM one could calculate not only the noise covariance matrices for Gaussian noise cases but also reduce the affects of geometric errors with the information obtained only from body surface potentials.

5.4 Future Works

- Studies on the estimation of the STM directly from the body surface potentials could be studied.
- Here we have assumed geometric errors as white Gaussian noise and even this wrong assumption improves the solutions significantly. Actually geometric errors are not Gaussian so adding the effects of the geometric errors to the formulation with a more convenient distribution could further improve results.

REFERENCES

[1] Eriksson H. Heart failure: a growing public health problem. *J Intern Med*, 237:135–141, 1995.

[2] Pullan A. J., Paterson D., and Greensite F. Noninvasive imaging of cardiac electrophysiology. *Phil. Trans. R. Soc. Lond. A*, 359:1277–1286, 2001.

[3] Menown I. B., Mackenzie G., and Adgey A. A. Optimizing the initial 12-lead electrocardiographic diagnosis of acute myocardial infarction. *Eur. Heart J.*, 21:275–283, 2000.

[4] Malmivuo J. and Plonsey R. *Bioelectromagnetism - Principles and Applications of Bioelectric and Biomagnetic Fields*. Oxford University Press, 1995.

[5] Zrenner B., Ndrepepa G., and Schmitt C. Use of multielectrode basket catheters for mapping of cardiac arrhythmias. *Herzschrittmachertherapie und Elektrophysiologie*, 11-1:4–10, 2000.

[6] Ramanathan C., Ghanem R. N., Jia P., Ryu K., and Rudy Y. Noninvasive electrocardiographic imaging for cardiac electrophysiology and arrhythmia. *Nature Medicine*, 2004.

[7] Vander A. J., Sherman J. H., and Luciano D. S. *Human Physiology*. McGraw-Hill Education, 2000.

[8] Jones S. A. *ECG Success: Exercises in ECG Interpretation*. F. A. Davis, 2008.

[9] Klabunde R. E. *Cardiovascular Physiology Concepts*. Lippincott Williams and Wilkins, 2004.

[10] Guyton A. C. and Hall J. E. *Textbook of Medical Physiology*. Elsevier Saunders, 2006.

[11] Despopoulos A. and Silbernagl S. *Color Atlas of Physiology*. Georg Thieme Verlag, 2003.

[12] Fallert M. A., Mirotznik M. S., Downing S. W., Savage E. B., Foster K. R., Josephson M. E., and Bogen D. K. Myocardial electrical impedance mapping of ischemic sheep hearts and healing aneurysms. *Circulation*, 87:199–207, 1993.

[13] Gulrajani R. M. The forward and inverse problems of electrocardiography. *IEEE Eng Med Biol Mag.*, 17:84–101,122, 1998.

[14] Babaeizadeh S. and Brooks D. H. Boundary element methods for electrocardiography. *CDSP, NEU, Boston, MA, USA*, 2003.

[15] Babaeizadeh S. and Brooks D. H. Using electrical impedance tomography for inverse electrocardiography. *CDSP, NEU, Boston, MA, USA*, 2004.

[16] Babaeizadeh S., Brooks D. H., Isaacson D., Newell J. C., and Macleod R. S. The 3d boundary element method for forward and inverse electrical impedance tomography,. *NCRR Site Visit, Salt Lake City, Utah, USA*, 2005.

[17] Sands G. B., French R. A., Withy S. J., Pullan A. J., and Legget M. E. Validation of human electrocardiographic inverse studies using ventricular pacing. *Cardiac Society of Australia New Zealand: 49th Annual Scientific Meeting, Auckland, NZ,*, page 120, 2001.

[18] Cheng L. K., Buist M. L., Sands G. B., and Pullan A. J. Interpretation of ecg signals through forward and inverse modeling. *Proc. EMBS/BMES Conference, Houston, TX, USA*, page 120, 2002.

[19] Seger M., Fischer G., Modre R., Messnarz B., Hanser F., and Tilg B. Lead field computation for the electrocardiographic inverse problem-finite element versus boundary elements. *Computer Methods and Programs in Biomedicine*, 77:241–252, 2005.

[20] Johnson C. R. and MacLeod R. S. Nonuniform spatial mesh adaptation using a posteriori error estimates: applications to forward and inverse problems. *Applied Numerical Mathematics*, 14:311–326, 1994.

[21] Shou C., Xia L., Jiang M., Liu F., and Crozier S. Forward and inverse solutions of electrocardiography problem using an adaptive bem method. *Springer-Verlag Berlin Heidelberg FIMH*, pages 290–299, 2007.

[22] Wang Y. and Rudy Y. Application of the method of fundamental solutions to potential-based inverse electrocardiography. *Annals of Biomedical Engineering*, 34-8:1272–1288, 2006.

[23] Arthur R. M., Geselowitz D. B., Briller S. A., and Trost R. F. The path of the electrical center of the human heart determined from surface electrocardiograms. *J. Electrocardiol.*, 4(1):29–33, 1971.

[24] Gulrajani R. M. and Mailloux G. M. A simulation study of the effects of torso inhomogeneities on electrocardiographic potentials, using realistic heart and torso models. *Circ. Res.*, 52:45–56, 1983.

[25] Pullan A. J., Cheng L. K., Nash M. P., Bradley C. P., and Paterson D. J. Noninvasive electrical imaging of the heart: Theory and model development. *Annals of Biomedical Engineering*, 29:817836, 2001.

[26] Nash M. P. and Pullan A. J. Challenges facing validation of noninvasive electrical imaging of the heart. *A. N. E*, 10-1:73–82, 2005.

[27] Bradley C.P., Pullan A.J., and Hunter P.J. Effects of material properties and geometry on electrocardiographic forward simulations. *Annals of Biomedical Engineering*, 28:721–741, 2000.

[28] Cheng L. K., Bradley C.P., and Pullan A.J. Effects of experimental and modeling errors on electrocardiographic inverse formulations. *IEEE Trans. Biomed. Eng.*, 50:23–32, 2003.

[29] Mesnarz B., Tilg B., Modre R., Fischer G., and Hanser F. A new spatio-temporal regularization approach for reconstruction of cardiac transmembrane potential patterns. *IEEE Trans. Biomed. Eng.*, 51-2:273–281, 2004.

[30] Farina D., Jiang Y., Skipa O., Dössel O., Kaltwasser C., and Bauer W. R. The use of the simulation results as a priori information to solve inverse problem of ecg for a patient. *Computers in Cardiology*, 32:571–574, 2005.

[31] Calderero F., Ghodrati A., Brooks D. H., Tadmor G., and MacLeod R. S. A method to reconstruct activation wavefronts without isotropy assumptions using a level sets approach. *FIMH 2005, LNCS 3504*, pages 195–204, 2005.

[32] Brooks D. H., Ahmad G. F., Macleod R. S., and Maratos G. M. Inverse electrocardiography by simultaneous imposition of multiple constraints. *IEEE Trans. Biomed. Eng.*, 46-1:3–18, 1999.

[33] Rudy Y. and Messinger-Rapport B. J. The inverse problem in electrocardiography: Solutions in terms of epicardial potentials. *CRC Crit. Rev. in Biomed. Eng.*, 16:215–268, 1988.

[34] Oster H. S. and Rudy Y. The use of temporal information in the regularization of the inverse problem in electrocardiography. *IEEE Trans. Biomed. Eng.*, 39:66–75, 1992.

[35] Hansen P. C. Rank-deficient and discrete ill-posed problems: Numerical aspects of linear inversion. 1998.

[36] Serinagaoglu Y., Brooks D.H., and MacLeod R.S. Bayesian solutions and performance analysis in bioelectric inverse problems. *IEEE Trans. Biomed. Eng.*, 52-6:1009–1020, 2005.

[37] Onal M. and Serinagaoglu Y. Spatio-temporal solutions in inverse electrocardiography. *IFMBE Proceedings*, 22:180–183, 2008.

[38] Berrier K.L., Sorensen D.C., and Khoury D.S. Solving the inverse problem of electrocardiography using a duncan and horn formulation of the kalman filter. *IEEE Trans. Biomed. Eng.*, 51:507–515, 2004.

[39] Goussard Y., Joly D., and Savard P. Time-recursive solution to the inverse problem of electrocardiography. *http://citeseer.ist.psu.edu/357941.html*.

[40] El-Jakl J., Champagnat F., and Goussard Y. Time-space regularization of the inverse problem of electrocardiography. *IEEE EMBC and CMBEC*, pages 213–214, 1995.

[41] Joly D., Goussard Y., and Savard P. Time-recursive solution to the inverse problem of electrocardiography a model-based approach. *Proc. IEEE-EMBS*, pages 767–768, 1993.

[42] Aydin U. and Serinagaoglu Y. Use of activation time based kalman filtering in

inverse problem of electrocardiography. *IFMBE Proceedings*, 22:1200–1203, 2008.

[43] Aydin U. and Serinagaoglu Y. Comparison of bayesian map estimation and kalman filter methods in the solution of spatio-temporal inverse ecg problem. *Proc. WC 2009*, 2009.

[44] Jiang M., Xia L., Shou G., and Tang M. Combination of the lsqr method and a genetic algorithm for solving the electrocardiography inverse problem. *Phys. Med. Biol.*, 52:1277–1294, 2007.

[45] Jiang M., Xia L., and Shou G. Noninvasive electrocardiographic imaging: Application of hybrid methods for solving the electrocardiography inverse problem. *FIMH 2007, LNCS 4466*, 4466:269–279, 2007.

[46] He B. and Wu D. Imaging and visualization of 3-d cardiac electrical activity. *IEEE Trans. Inf. Tech. in Biomedicine*, 5-3:181–186, 2001.

[47] Greensite F. The temporal prior in bioelectromagnetic source imaging problems. *IEEE Trans. Biomed. Eng.*, 50-10:1152–1159, 2003.

[48] Ghodrati A., Brooks D. H., Tadmor G., and MacLeod R. S. Wavefront-based models for inverse electrocardiography. *IEEE Trans. Biomed. Eng.*, 53-9:1821–1831, 2006.

[49] Zhang Y., Ghodrati A., and Brooks D. H. An analytical comparison of three spatio-temporal regularization methods for dynamic linear inverse problems in a common statistical framework. *Inverse Problems*, 21:357–382, 2005.

[50] Greensite F. A new treatment of the inverse problem of multivariate analysis. *Inverse Problems*, 18:363–379, 2002.

[51] Doessel O., Bauer W. R., Farina D., Kaltwasser C., and Skipa O. Imaging of bioelectric sources in the heart using a cellular automaton model. *Proc. IEEE EMBS*, pages 1067–1070, 2005.

[52] He B., Li G., and Zhang X. Noninvasive imaging of cardiac transmembrane potentials within three-dimensional myocardium by means of a realistic geometry anisotropic heart model. *Phys. Med. Biol.*, 47:4063–4078, 2002.

[53] He B., Li G., and Zhang X. Noninvasive three-dimensional activation time imaging of ventricular excitation by means of a heart-excitation model. *IEEE Trans. Biomed. Eng.*, 50-10:1190–1202, 2003.

[54] Nash M.P., Bradley C.P., Kardos A., Pullan A.J., and Paterson D.J. n experimental model to correlate simultaneous body surface and epicardial electropotential recordings in vivo. *Chaos, Solitons and Fractals*, 13:1735–1742, 2002.

[55] Oster H. and Tacardi B. Electrocardiographic imaging: Noninvasive characterization of intramural myocardial activation from inverse reconstructed epicardial potentials and electrograms. *Circulation*, 97:1496–1507, 1998.

[56] Macleod R. S., Lux R. L., and Tacardi B. A possible mechanism for electrocardiographically silent changes in cardiac repolarization. *J. Electrocardiol.*, 30:114–121, 1997.

[57] Barr R. C. and Spach M. S. Inverse calculation of qrs-t epicardial potentials from body surface potential distributions for normal and ectopic beats in the intact dog. *Circ. Res.*, 42:661–675, 1978.

[58] Spach M. S., Barr R. C., Lanning C. F., and Tucek P. C. Origin of body surface qrs and t wave potentials from epicardial potential distributions in the intact chimpanzee. *Circulation*, 55:268–278, 1977.

[59] Aydin U. and Serinagaoglu Y. Statistical modeling of the geometric error in cardiac electrical imaging. *Proc. ISBI 2009*, pages 442–445, 2009.

[60] Ramanathan C. and Rudy Y. Electrocardiographic imaging: I. effect of torso inhomogeneities on body surface electrocardiographic potentials. *Journal of Cardiovascular Electrophysiology*, 12:229–240, 2001.

[61] Ramanathan C. and Rudy Y. Electrocardiographic imaging: Ii. effect of torso inhomogeneities on noninvasive reconstruction of epicardial potentials, electrograms, and isochrones. *Journal of Cardiovascular Electrophysiology*, 12:241–252, 2001.

[62] Messinger-Rapport B. J. and Y. Rudy. The inverse problem in electrocardiography: A model study of the effects of geometry and conductivity parameters

on the reconstruction of epicardial potentials. *IEEE Trans. Biomed. Eng.*, 33-7:667–676, 1986.

[63] Huiskamp G. and Oosterom A. V. Tailored versus realistic geometry in the inverse problem of electrocardiography. *IEEE Trans. Biomed. Eng.*, 36-8:827–835, 1989.

[64] Jiang Y., Farina D., and Doessel O. Effect of heart motion on the solutions of forward and inverse electrocardiographic problem - a simulation study. *Computers in Cardiology*, 35:365–368, 2008.

[65] Barr R. C., Ramsey M., and Spach M. S. Relating epicardial to body surface potential distributions by means of transfer coefficients based on geometry measurements. *IEEE Trans. Biomed. Eng.*, 24-1:1–11, 1977.

[66] Tikhonov A. N. and Arsenin V.Y. *Solution of Ill-Posed Problems*. Winston and Sons Washington., 1977.

[67] Hansen P. C. and OLeary D. P. The use of the l-curve in the regularization of discrete ill-posed problems. *SIAM J. Sci. Comput.*, 14:1487–1503, 1993.

[68] Kay S. M. *Fundamentals of Statistical Signal Processing: Estimation Theory*. Englewood Cliffs, NJ: Prentice-Hall, 1993.

[69] Aster R., Borchers B., and Thurber T. *Parameter Estimation and Inverse Problems*. Academic Press, 2004.

[70] McGee L. A. and Schmidt S. F. Discovery of the kalman filter as a practical tool for aerospace and industry, 1985.

[71] Xiaoyun L., Xiaoling Z., and Xian X. Application of kalman filter in agricultural economic forecasting. *IEEE Int. Conf. on Sys., Man, and Cybernetics*, 3:2185–2189, 1996.

[72] Ennola K., Sarvala J., and Devai G. Modelling zooplankton population dynamics with the extended kalman filtering technique. *Ecological Modelling 110, pp. 135-149, 1998*, 110:135–149, 1998.

[73] Grewal M. S. and Andrews A. P. *Kalman filtering : theory and practice using MATLAB*. New York: John Wiley, 2 edition, 2001.

[74] Jazwinski A. H. *Stochastic processes and filtering theory*. Mineola, N.Y. : Dover Publications, 2007.

[75] Shumway R. H. and Stoffer D. S. *Time Series Analysis and Its Applications : With R Examples*. New York: Springer, 2 edition, 2006.

[76] Kaipio J. P. and Somersalo E. *Computational and Statistical Methods for Inverse Problems Applied Mathematical Sciences*. New York: Springer-Verlag, 2004.

[77] Heino J., Somersalo E., and Kaipio J. P. Compensation for geometric mismodelling by anisotropies in optical tomography. *Optics Express*, 13-1:296–308, 2005.

[78] Bailie A. E. and Jazwinski A. H. Adaptive filtering interim report, 1967.

[79] Shumway R. H. and Stoffer D. S. An approach to time series smoothing and forecasting using the em algorithm. *Journal of Time Series Analysis*, 3-4:253–264, 1982.

[80] MacLeod R.S. and Johnson C.R. Map3d: Interactive scientific visualization for bioengineering data. *IEEE EMBS 1993*, pages 30–31, 1993.